Interaction of ^{6}He with hydrogen isotopes at 26 MeV/n energy

Bogumił Zalewski

February 2024

Dedication

To my Wife

my Kids

and my Mentors

Contents

Abstract

In the present work elastic scattering measurements for the p+^{6}He and d+^{6}He systems, as well as the ^{6}He(d,t)^{5}He transfer reaction were performed at 26 MeV/n in inverse kinematics at the ACCULINNA-2 fragment separator. The obtained angular distributions of the elastic scattering were analyzed within the Optical Model (OM), and the transfer reaction angular distribution was analyzed using the Distorted-Wave Born Approximation (DWBA) method.

The obtained angular distribution of the differential cross section for the p+^{6}He elastic scattering is in good agreement with the data obtained by Wolski [1] at a slightly lower energy (25 MeV/u) measured at the ACCULINNA fragment separator. The data set is in agreement with the differential cross section calculated with the global OM potential of Varner [2] as well as the cross sections calculated using optical potentials by Wolski [1] and the optical potential obtained from microscopic Continuum-Discretised Coupled Channels (CDCC) calculations by Rusek [3].

The differential cross section of the d+^{6}He elastic scattering was measured for the first time with a good angular resolution thanks to the use of a CD_2 target. The experimental data set is reproduced well by OM calculations with the optical potentials derived from the p+^{6}He OM potentials using the folding method. This suggests that the influence of deuteron breakup on the elastic scattering is small. It also appears that the quadrupole deformation of the ^{2}H ground state has little influence on the d+^{6}He elastic scattering. From the set of global optical potentials for deuteron scattering considered, the potential of Zhang [4] fits the experimental data best.

The angular distribution of the differential cross section for the ^{6}He(d,t)^{5}He neutron transfer reaction was measured for the first time. The obtained cross section was analyzed using the DWBA method. The optical potentials used to generate the entrance channel distorted waves were the empirical potentials obtained from the analysis of the d+^{6}He elastic scattering. It was found that the choice of entrance channel potential has a minor influence on the final cross section. The exit channel wave functions were generated with the global Optical Model Potential (OMP) of Pang [5] and with the OMP obtained from folding the ^{4}He+t and n+t OM potentials with the wave function of the $^{5}\mathrm{He}_{\mathrm{g.s.}}$.

Wave functions of the cluster-to-core relative motion for $^{5}\mathrm{He}_{\mathrm{g.s.}}$+n and ^{2}H+n systems were obtained from the single particle binding potentials. It was observed that the remnant part strongly influences the differential cross section of the transfer reaction in the DWBA calculations. Post and prior approaches give different results with no remnant and almost the same result with the full remnant term.

The spectroscopic amplitude $\mathrm{S}_{5\mathrm{He+n}}$ for the $^{6}\mathrm{He}_{\mathrm{g.s.}}$=$^{5}\mathrm{He}_{\mathrm{g.s.}}$+n configuration was adjusted so that the calculated differential cross section for the transfer reaction reproduced the data points. It was averaged over the determination of different entrance and exit channel potentials and equals $\mathrm{S}_{5\mathrm{He+n}} = 1.167\ ^{+0.148}_{-0.140}$ after taking into account experimental and theoretical uncertainties. The spectroscopic factor ($\mathrm{SF}_{5\mathrm{He+n}}$) calculated from the spectroscopic amplitude equals $\mathrm{SF}_{5\mathrm{He+n}} = 1.36\ ^{+0.35}_{-0.33}$ and is smaller than theoretical predictions, but agrees with them within the uncertainties.

Streszczenie

W poniższej pracy przedstawiono opis badań elastycznego rozpraszania systemów p+^{6}He i d+^{6}He, a także reakcji transferu neutronu ^{6}He(d,t)^{5}He przy energii 26 MeV/n w odwrotnej kinematyce przeprowadzonych na separatorze ACCULINNA-2. Otrzymane rozkłady kątowe elastycznego rozpraszania przeanalizowano w ramach Modelu Optycznego (OM), a rozkład kątowy reakcji transferu przeanalizowano za pomocą metody Distorted Wave Born Approximation (DWBA).

Otrzymany rozkład kątowy różniczkowego przekroju czynnego elastycznego rozpraszania p+^{6}He jest zgodny z danymi uzyskanymi przez Wolskiego na separatorze fragmentów ACCULINNA dla nieco niższej energii (25 MeV/n). Dane eksperymentalne są dobrze opisane przekrojami czynnymi obliczonymi w ramach modelu optycznego na podstawie globalnego potencjału optycznego (OMP) autorstwa Varnera [2], a także przekrojami czynnymi obliczonymi przy użyciu potencjałów optycznych autorstwa Wolskiego [1] oraz potencjału optycznego uzyskanego przy pomocy metody Continuum-Discretized Coupled Channels (CDCC) przez Ruska [3].

Rozkład kątowy elastycznego rozpraszania d+^{6}He został zmierzony po raz pierwszy z dobrą rozdzielczością kątową dzięki użyciu tarczy z deuteryzowanego polietylenu CD_2. Dane eksperymentalne są dobrze opisane przekrojami czynnymi obliczonymi w ramach modelu optycznego na podstawie potencjałów optycznych uzyskanych metodą foldingu ze złożenia potencjału p+^{6}He z funkcją falową ^{2}H. Sugeruje to mały wpływ dysocjacji deuteronu na proces elastycznego rozpraszania. Porównanie przekrojów czynnych d+^{6}He obliczonych ze zmierzonymi sugeruje także niewielki wpływ deformacji kawdrupolowej deuteronu na elastyczne rozpraszanie d+^{6}He. Spośród rozważanych globalnych potencjałów optycznych dla rozpraszania

deuteronu, globalny potencjał Zhanga [4] najlepiej opisuje uzyskane dane eksperymentalne.

Rozkład kątowy różniczkowego przekroju czynnego dla reakcji transferu neutronu z jądra ^{6}He do deuteru, ^{6}He(d,t)^{5}He, został zmierzony po raz pierwszy. Otrzymane przekroje czynne zostały przeanalizowane za pomocą metody DWBA. Potencjały optyczne użyte do wygenerowania funkcji falowych w kanale wejściowym były empirycznymi potencjałami uzyskanymi z analizy elastycznego rozpraszania d+^{6}He. Stwierdzono, że wybór potencjału w kanale wejściowym ma niewielki wpływ na uzyskany przekrój czynny. Funkcje falowe w kanale wyjściowym wygenerowano za pomocą globalnego potencjału optycznego parametryzowanego przez Panga [5] oraz za pomocą potencjału optycznego uzyskanego poprzez złożenie potencjałów optycznych ^{4}He+t i n+t z funkcją falową ^{5}He$_{\mathrm{g.s}}$.

Funkcje falowe neutronu w systemach ^{5}He$_{\mathrm{g.s.}}$+n i ^{2}H+n uzyskano z potencjałów wiązania pojedynczej cząstki. Zauważono, że część *remnant* potencjału przejścia ma duży wpływ na przekrój czynny uzyskany metodą DWBA. Podejścia *post* i *prior* dają różne wyniki bez części *remnant* oraz prawie takie same wyniki z częścią *remnant*, niezależnie od użytego potencjału interakcji rdzeń-rdzeń.

Amplituda spektroskopowa $S_{5\mathrm{He+n}}$ konfiguracji ^{6}He$_{\mathrm{g.s.}}$=^{5}He$_{\mathrm{g.s.}}$+n została dobrana tak, aby różniczkowy przekrój czynny dla reakcji transferu pasował do uzyskanych punktów pomiarowych i została uśredniona dla różnych potencjałów kanału wejściowego i wyjściowego otrzymując $S_{5\mathrm{He+n}} = 1.167\ ^{+0.148}_{-0.140}$ po uwzględnieniu błędów eksperymentalnych i analizy. Czynnik spektroskopowy $SF_{5\mathrm{He+n}}$ obliczony z amplitudy spektroskopowej wynosi $SF_{5\mathrm{He+n}} = 1.36\ ^{+0.35}_{-0.33}$ i jest mniejszy od przewidywań teoretycznych, ale zgadza się z nimi po uwzględnieniu niepewności pomiarowej.

Acknowledgements

At this point, I want to thank the following individuals and institutions for their invaluable support and contributions throughout the long journey of completing this PhD thesis.

First, I would like to express my deep gratitude to my supervisor, Professor Krzysztof Rusek, for his guidance, patience, and unwavering support. He assisted with the experiment proposal, being the foundation of my PhD thesis, and helped me during data analysis while being hundreds of kilometers away. After returning to Poland, the professor introduced me to theoretical models, explained the intricacies of data interpretation, and always pointed me in the right direction.

Also, I sincerely thank Professor Mikhail Sergeevich Golovkov for his mentorship during my stay in Dubna. Professor Golovkov spent his valuable time explaining the principles of the experiment, the data analysis process, and underlying physics. I will never forget his "Introduction to Nuclear Electronics".

I appreciate all ACCULINNA-2 group members, without whom this work would not have been possible - special thanks to Andrey Bezbakh and Grzegorz Kamiński for invaluable talks and countless nights spent on experiment preparations.

I am profoundly grateful to Professor Nicolas Keeley for the language corrections in this work.

I acknowledge the support of my family and friends, whose encouragement, patience, and understanding have sustained me through the challenges of doctoral research.

I would also like to express my gratitude to Narodowe Centrum Nauki for their financial support in Preludium 41 2021/41/N/ST2/03446 and to the Commission of Plenipotentiary Representative for their financial support in grants "Cryogenic target system for ACCULINNA-2 fragment separator" and "ACCULINNA-2 experimental setup upgrade and its elements unification".

Introduction

Increases in the intensity and availability of radioactive beams and technological advances in their separation allow intensive studies of radioactive nuclei situated further and further from the stability line. Such experiments further our understanding of the structure of atomic nuclei and their interactions.

A particular case of radioactive nuclei are the neutron halo nuclei, the most prominent examples of such nuclei. They consist of a compact core with one or two neutrons orbiting it. The lightest halo nucleus is helium-6, which, due to the small number of nucleons, is among the most straightforward systems to treat from a theoretical point of view. ^{6}He is usually depicted as an alpha core with two loosely bound neutrons orbiting it. More careful examinations revealed that it is a mixture of configurations such as ^{5}He+n, ^{4}He+2n and triton + triton. The probability of finding the system in a particular configuration is expressed in terms of a spectroscopic factor.

A recently published review [6] of the current status of spectroscopic factors describes, among other things, the so-called quenching of spectroscopic factors. This issue has been known for decades and involves significant discrepancies between experimentally obtained single-particle spectroscopic factors and their theoretical predictions within the framework of the independent particle model. Additionally, an influence of asymmetry in the binding energy of individual nucleons on the spectroscopic factor is observed in knockout reactions. In contrast, no such influence is noted in transfer reactions. Due to the substantial difference in the binding energy of neutrons and protons ($\Delta S = -20.88$ MeV), ^{6}He proves a promising candidate for such investigations.

An experimental investigation of p+^{6}He reactions by Wolski et al. [1] at ACCULINNA provided considerable insight into the structure of helium-6 and contributed a significant amount of material for later analysis with more advanced methods [7, 8] like microscopic CDCC calculations. A measurement of the d+^{6}He elastic scattering differential cross section would provide the entrance channel interaction potential required for an analysis of the ^{6}He(d,t)^{5}He neutron transfer with the DWBA method. Moreover, this reaction has not been measured before. It might deliver exciting results, especially since both helium-6 and the deuteron are loosely bound systems with ^{2}H having the lowest binding energy per nucleon of all stable nuclei.

The CDCC method has been recently extended to systems involving two weakly bound nuclei by Descouvemont [9, 10]. He successfully analyzed the d+^{11}Be, d+^{7}Li, and d+^{11}Li systems. The data obtained from the measurement of elastic scattering of d+^{6}He and the ^{6}He(d,t)^{5}He transfer reaction will constitute a solid foundation for further development of the four-body CDCC model.

In summary, measurements of elastic scattering of ^{1,2}H+^{6}He and the ^{6}He(d,t)^{5}He transfer reaction were proposed at an energy of 26 MeV/n. The measurements were conducted at the Flerov Laboratory of Nuclear Reactions at the Joint Institute for Nuclear Research in Dubna, Russia, at the ACCULINNA-2 separator. This experiment was performed in 2018 and marked the first physics experiment on this separator.

Chapter 1

Theoretical introduction

In this chapter, a concise overview of the theory of nuclear reactions will be introduced. The mathematical language used to analyze the obtained experimental results will be described, with Section 1.1 introducing the theory of scattering, as well as the Optical Model and selected issues related to it. Section 1.2 will describe the theoretical model used to analyze nucleon transfer reactions.

1.1 Scattering theory

The beginning of nuclear physics is considered to be the discovery of radioactivity by Henri Becquerel in 1896. While studying phosphorescence in uranium salts, Becquerel discovered the phenomenon of radioactivity, which was later identified as an alpha decay. Just over 20 years later, Ernest Rutherford first observed a nuclear reaction induced by alpha particles emitted from radioactive radium. Over time, alpha particles began to be used to induce nuclear reactions. In 1932, Cockroft and Walton built the first accelerator to initiate nuclear reactions using accelerated protons. Studying artificially induced nuclear reactions with increasingly higher energies, various targets, and different projectiles has led to a better understanding and description of many phenomena occurring in nuclei.

A typical nuclear reaction may be written as

$$a + A \rightarrow B + b + Q \tag{1.1}$$

where A is the target nucleus, a the incident nucleus, B and b the reaction products, and Q the energy released or absorbed during the reaction. This reaction may equally be written as

$$A(a,b)B \tag{1.2}$$

1.1.1 Elastic scattering

Elastic scattering is the simplest nuclear reaction from the point of view of theoretical considerations. The internal structure of the participating nuclei does not change; they remain in their ground states. In the case of elastic scattering, Equation 1.2 will take the form

$$A(a,a)A \tag{1.3}$$

One of the main quantities characterizing a nuclear reaction is the reaction cross section. The cross section is denoted by the Greek letter σ and determines the probability of a given reaction occurring. Taking the example of a typical scattering experiment, where a beam of nuclei a hits a target formed of nuclei A, it can be expressed by the following relation

$$\sigma = \frac{N_{scattered}}{N_{tar}\ N_{beam}} \tag{1.4}$$

where $N_{scattered}$ is the number of a nuclei scattered, N_{tar} is the number of A nuclei in the target per unit area, and N_{beam} is the number of beam particles a incident on the target. The unit of σ is m^2, but due to the low values of cross sections, barns (1 barn $= 10^{-28}\ \mathrm{m}^2 = 100\ \mathrm{fm}^2$) or millibarns are used instead. By measuring the number of particles emitted per time unit within an element of solid angle $d\Omega$ in the direction with polar angles (θ, ϕ), we obtain a differential cross section. The differential cross section is usually given in the center-of-mass (CM) system of coordinates and is defined as

$$\frac{d\sigma(\theta,\phi)}{d\Omega} = |f(\theta,\phi)|^2 \tag{1.5}$$

where $d\Omega$ is the solid angle element and $f(\theta,\phi)$ is a scattering amplitude depending on the angles θ and ϕ in a spherical coordinate system. When there is no spin polarisation of the beam or the target, the scattering amplitude does not depend on

the angle ϕ, and the cross section is a function of θ alone.

In the above example, we may consider the beam of particles a from an accelerator moving along the Z axis as a plane wave described by a wave function χ_A

$$\chi_a = A_0 \; exp \; i(\mathbf{k}_a z) \tag{1.6}$$

where A_0 is the beam flux before any collision, $\mathbf{k}_a$ is the wave number $\mathbf{k}_a = \mathbf{p}_a/\hbar$ with $\mathbf{p}_a$ the particle momentum. Similarly, the target particles A can be described by the following wave function

$$\chi_A = N_0 \; exp \; i(\mathbf{k}_A z) \tag{1.7}$$

with N_0 the number of particles per unit volume and $\mathbf{k}_A$ being the wave number. In the case of stationary target $\mathbf{k}_A = 0$, since the momentum resulting from thermal movements can be neglected. In order to describe the system of particles a impinging on target A in the center-of-mass system, we can use the relation

$$\chi_\alpha = \chi_A \chi_a = A_0 \exp[i(\mathbf{k}_\alpha \mathbf{r}_\alpha)] \tag{1.8}$$

where $\mathbf{r}_\alpha = \mathbf{r}_a - \mathbf{r}_A$ is the distance between the particles and r_a and r_A are the position vectors of the incident particle and the target; N_0 is assumed to be equal to 1 particle per unit volume for simplicity and

$$\mathbf{k}_\alpha = \frac{m_A}{m_a + m_A}\mathbf{k}_a \tag{1.9}$$

is the relative momentum between the particles, where m_A and m_a are the masses of the target and incident particles, respectively. Equation 1.8 describes the incoming beam plus the stationary target system without considering any internal structure of these particles. We will refer to this as the entrance channel. In order to include information about the structure of these nuclei, we introduce the wave functions φ_A and φ_a which describe the internal structure of the target and the beam nuclei. We thus obtain

$$\chi_\alpha = A_0 \; exp(i\mathbf{k}_\alpha \mathbf{r}_\alpha)\varphi_A \varphi_a \tag{1.10}$$

The above equation describes the so-called incident wave without any particle interaction. For a complete description of the actual process, we would have to include scattered waves for each possible exit channel β in a form

$$\Psi = A_0 \exp(i\mathbf{k}_\alpha \mathbf{r}_\alpha)\varphi_a\varphi_A + \sum_\beta \chi_\beta \tag{1.11}$$

We will now focus on the wave function of a example exit channel. We assume that the distance from the target is sufficient by large so that there is no interaction potential between the nuclei and that the wave has a radial form

$$\Psi_\beta = A_0 f_\beta(\theta,\phi)\frac{exp(i\mathbf{k}_\beta \mathbf{r}_\beta)}{r_\beta}\varphi_B\varphi_b \tag{1.12}$$

with A_0 the particle flux in the entrance channel, φ_B and φ_b the wave functions of the internal states in the exit channel, and $\mathbf{k}_\beta$ and $\mathbf{r}_\beta$ the wave number and the distance between the nuclei in the exit channel. For the elastic scattering reaction, we have $\varphi_a = \varphi_b$ and $\varphi_A = \varphi_B$. For a given radius $r_\beta = r$ and with no spin polarization, we obtain the density of the scattered particles, defined as the square modulus of the wave function, in the form

$$\frac{1}{r^2}\left|A_0 f_\beta(\theta)\right|^2. \tag{1.13}$$

This gives $\left|A_0 f_{elastic}(\theta)\right|^2 d\Omega$ for an element of solid angle, and finally, through dividing by the original particle flux, we obtain equation 1.5

$$\frac{d\sigma_{elastic}}{d\Omega} = |f_\beta(\theta)|^2 \tag{1.14}$$

With the wave function in the form presented in equation 1.11 and a known interaction potential $V(\mathbf{r})$, we could try to find the reaction cross section by solving the Schrödinger equation

$$\left[-\frac{\hbar^2}{2m}\nabla^2 + V(\mathbf{r})\right]\Psi(\mathbf{r}) = E\Psi(\mathbf{r}) \tag{1.15}$$

where m is the particle mass and E its energy. The term in square brackets is the sum of the kinetic and potential energies, called the Hamiltonian. It is often denoted

by $\hat{H}$. Unfortunately, including all of the open reaction channels is impossible, and there is insufficient computing power to solve the Schrödinger equation for nuclear reaction. Instead, we will use physical models, which allow us to obtain reaction cross sections and information about nuclear structure.

1.1.2 Optical model

One of the models used to describe nuclear reactions is the optical model proposed by Fernbach, Serber, and Taylor [11]. The optical model simplifies the complex many-body problem of the interactions between the nucleons in the target nucleus and the incident particle by approximating it as a two-body problem. Instead of considering the various interactions individually, they are replaced by a spherical potential $U(r)$ independent of the orientation of the vector $\mathbf{r}$, which represents the interaction between the incident particle and the nucleus. This effective potential as used in the model is complex

$$U(r) = V_{re}(r) + iW_{im}(r) \tag{1.16}$$

where the real part $V_{re}(r)$ represents the scattering potential between the nuclei and the imaginary part $iW_{im}(r)$ is associated with absorption of the particle flux from the elastic channel. If the incoming particle becomes excited through interaction with the target nucleus, we call it a non-elastic event. As a result, this particle is removed from the elastic channel. It is important to note that the absorption does not describe non-elastic reactions but merely accounts for their effect on the elastic scattering. This approximation is called the "optical model" because it shares similarities with the description of the scattering of light by an almost transparent but refractive sphere. There, a complex refractive index is used in order to include attenuation of the light as it travels through the medium.

The most commonly used form of the optical potential is the Woods-Saxon, given by the following formula

$$f_{WS}(r) = \frac{-1}{1 + e^{(r-R)/a}} \tag{1.17}$$

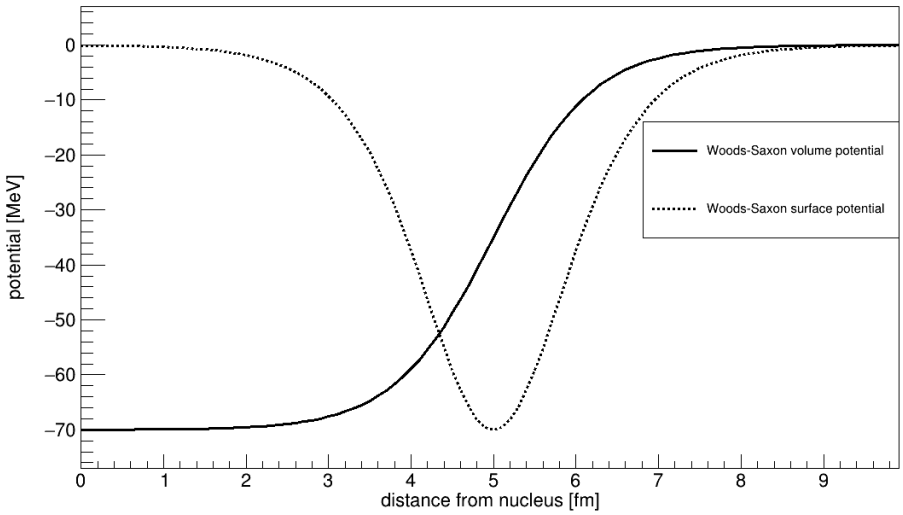

Figure 1.1: A comparison between the shapes of the volume and surface Woods-Saxon potentials with $V_0 = V_s = 70\ MeV$, $R_v = R_s = 5\ fm$ and $a_v = a_s = 0.6\ fm$

where r [fm] is the distance between the nuclei, $R = r_0 A^{1/3}$ [fm] is the nuclear radius, and a [fm] is the potential diffuseness. Combining equations 1.16 and 1.17 we obtain

$$U(r) = \frac{-V_0}{1 + e^{(r-R_v)/a_v}} + \frac{-iW_0}{1 + e^{(r-R_w)/a_w}} \tag{1.18}$$

where V_0 [MeV] and W_0 [MeV] are the real and imaginary potential amplitudes, respectively. Eq. 1.18 is the simplest form of the optical model potential based on Woods-Saxon terms for both the real and the imaginary parts. It is commonly referred to as a volume potential.

A complete optical potential $U(r)$ may contain several terms. One of the other widely used terms has the form of the radial derivative of the volume potential and is described by the following formula

$$W_s(r) = -4a_s \frac{d}{dr} \frac{-V_s}{1 + e^{(r-R_s)/a_s}} \tag{1.19}$$

This form of the potential is also referred to as a surface potential. Figure 1.1 presents an example of volume and surface potentials of Woods-Saxon forms.

Another type of a potential used in the optical model is the spin-orbit potential. This potential is a nuclear analog of the spin-orbit coupling of the electron spin $\mathbf{s}$ and its orbital angular momentum $\mathbf{l}$ in the electrostatic potential of the nucleus.

It has the so-called Thomas radial form

$$V_{so}(r) = -2V_{so}\frac{-1}{r}\frac{d}{dr}\frac{1}{1+e^{(r-R_{so})/a_{so}}}(\mathbf{l}\cdot\mathbf{s}) \tag{1.20}$$

Finally, there is the Coulomb potential for the scattering of charged particles calculated with the following formula:

$$V_c(r) = \begin{cases} \frac{1}{4\pi\epsilon_0}\frac{Z_1 Z_2 e^2}{2R_c}\left(3-\frac{r^2}{R_c^2}\right) & \text{for } r \le R_c \\ \frac{1}{4\pi\epsilon_0}\frac{Z_1 Z_2 e^2}{r} & \text{for } r \ge R_c \end{cases} \tag{1.21}$$

where Z_1 and Z_2 are the charge numbers of the projectile and target nuclei, e is the elementary charge, and R_c is the Coulomb radius.

A typical [12] optical model potential used to describe a scattering reaction thus has the form:

$$U(r) = -V_0 f_{WS}(r, R_v, a_v) - iW_0 f_{WS}(r, R_w, a_w) - iW_s(4a_s)\frac{d}{dr}f_{WS}(r, R_s, a_s) + V_C(r) \tag{1.22}$$

where V_0, W_0, and W_s are the depths of the real volume potential and the imaginary volume and surface potentials, respectively.

The above form of the optical potential is often found in so-called Global Optical Potentials (GOM). The potential amplitudes, radii, and diffusivities in these models are described as functions of, for example, energy, atomic numbers A and Z, and certain constants. These constants are chosen so that the calculated differential cross sections based on the potential best describe a large set of experimental data.

1.1.3 Folding model

The folding model is a microscopic approach which aims to obtain the interaction potential between two nuclei based on the sum of the two-body interactions between one of the nuclei and the constituents of the other nucleus. Let us consider a particle P moving towards a target nucleus T. A diagram of the description of the adopted coordinates is shown in Figure 1.2. Their interaction potential can be described by the sum of effective interactions between each nucleon of the target

(T1 and T2) and the incoming particle using the formula

$$U(\mathbf{r}) = \int \rho(\mathbf{R})\nu(|\mathbf{r} + \frac{1}{2}\mathbf{R}|)d\mathbf{R} \tag{1.23}$$

with $\rho(\mathbf{R})$ being the target nucleus density distribution and $\nu(|\mathbf{r} + \frac{1}{2}\mathbf{R}|)$ being the effective interaction between the particle and each of the target nucleons. It is worth noting that the density distribution of the atomic nucleus is the square of its wave function, and the effective interaction between a nucleus and a nucleon can be described using the optical potential. The above method can also be successfully extended to an atomic nucleus with a known wave function and its interaction with another atomic nucleus, assuming the absence of any internal structure. This approach is called single-folding, while when we assume that the second particle also has internal structure, we need to integrate over it as well, giving the name double-folding.

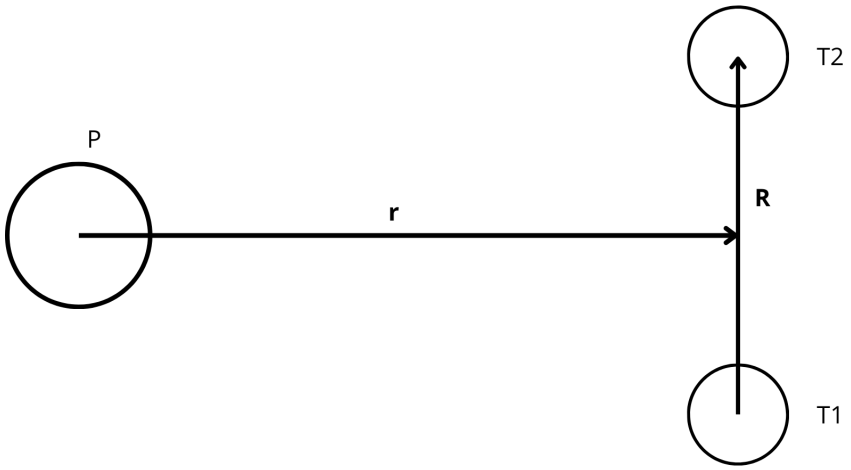

Figure 1.2: T system of coordinates used for the folding potential description.

1.2 Transfer reactions

A transfer reaction is a complex many-body reaction where a nucleon or a part of a nucleus, called a cluster, is transferred to another nucleus. Using the

notation introduced earlier, an example transfer reaction can be written as

$$a + A \rightarrow B + b + Q \tag{1.24}$$

We will denote the transferred particle as x and define the entrance channel nucleus

$$A = B + x \tag{1.25}$$

and the exit channel particle

$$b = a + x \tag{1.26}$$

Figures 1.3 and 1.4 accordingly present a schematic of the entrance and exit channel configurations. A complete mathematical description of the process is impossible

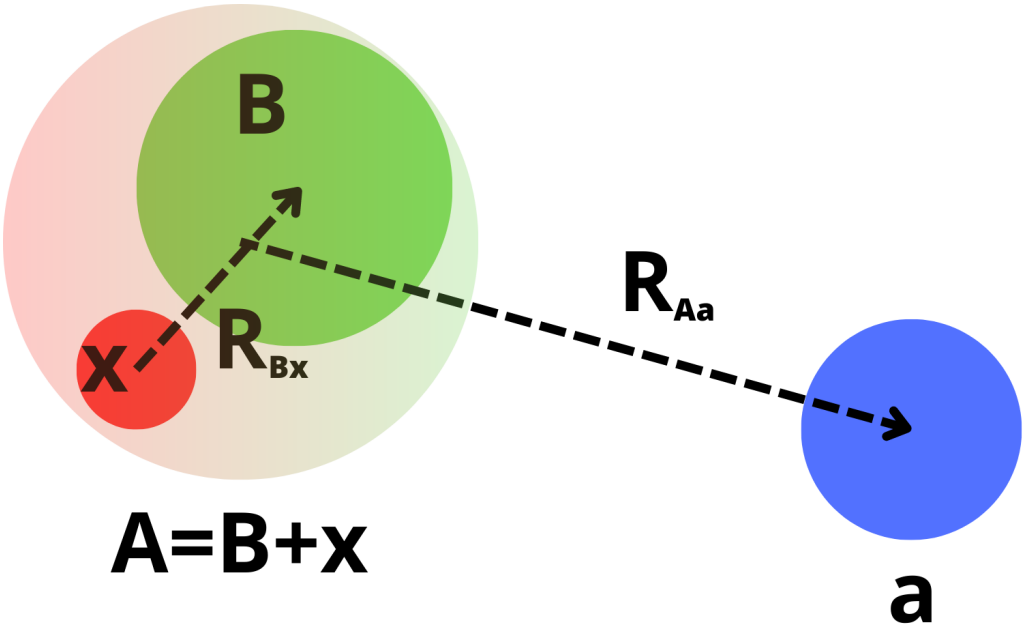

Figure 1.3: Schematic view of the entrance channel with coordinates marked.

since all possible channels would have to be considered, just as for the elastic scattering. Instead, we will use the distorted wave Born approximation formalism which allows for a description of inelastic scattering, transfer, and knockout reactions. A detailed derivation of the DWBA formalism and its approximations are given in detail in many works [12, 13] and will not be given here.

We will start with a formula describing the differential cross section for an example reaction A(a,b)B within the DWBA method:

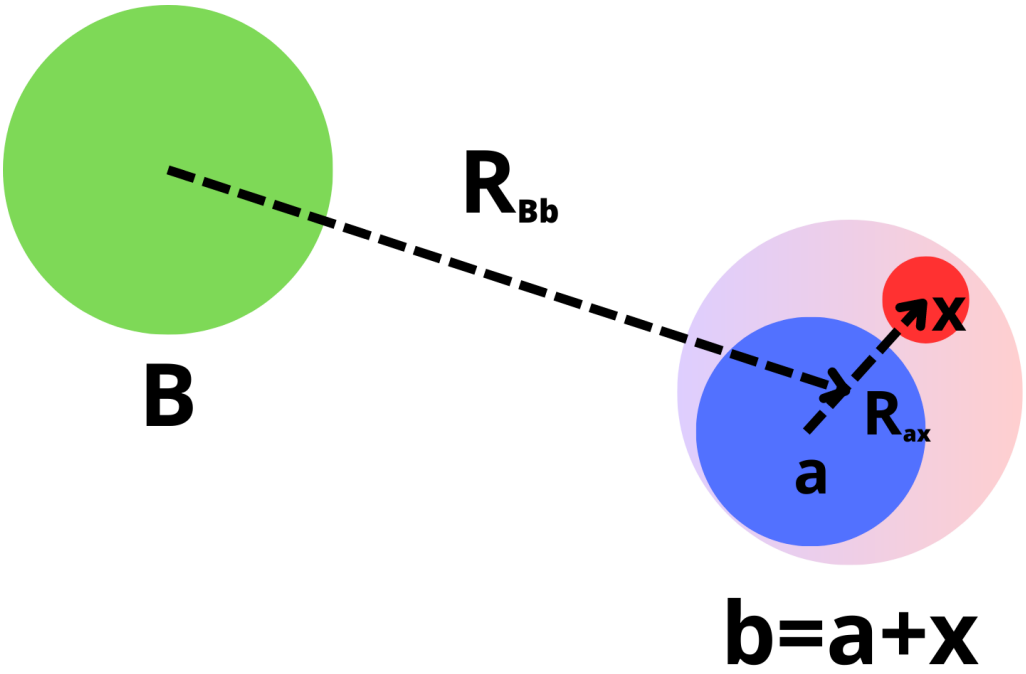

Figure 1.4: Schematic view of the exit channel with coordinates marked.

$$\frac{d\sigma(\theta)}{d\Omega} = \frac{\mu_\alpha \mu_\beta}{\left(2\pi\hbar^2\right)^2} \frac{k_\beta}{k_\alpha} |T|^2 \tag{1.27}$$

where μ_α and μ_β are the reduced masses of the entrance and exit channels respectively, and can be calculated using the following relations

$$\mu_\alpha = \frac{m_a m_A}{m_a + m_A}, \qquad \mu_\beta = \frac{m_b m_B}{m_b + m_B}$$

k_α and k_β are the relative momenta of the nuclei in the entrance and exit channels, respectively, and can be calculated using the following relations

$$k_\alpha = \frac{m_A k_a - m_a k_A}{m_a + m_A}, \qquad k_\beta = \frac{m_B k_b - m_b k_B}{m_b + m_B}$$

The T in equation 1.27 is a transition amplitude defined as

$$T = \iint \chi_\beta^{(-)}(\mathbf{k}_\beta, \mathbf{r}_\beta)^* \langle \varphi_b \varphi_B | \mathbf{U} | \varphi_a \varphi_A \rangle \chi_\alpha^{(+)}(\mathbf{k}_\alpha, \mathbf{r}_\alpha) d\mathbf{r}_\alpha d\mathbf{r}_\beta \tag{1.28}$$

where $\chi_\beta^{(-)}(\mathbf{k}_\beta, \mathbf{r}_\beta)^*$ and $\chi_\alpha^{(+)}(\mathbf{k}_\alpha, \mathbf{r}_\alpha)$ are wave functions describing the elastic scattering in the entrance and exit channels respectively. These wave functions are the

time inverse of each other and are related by

$$\chi_{\beta}^{(-)}(\mathbf{k}_{\beta}, \mathbf{r}_{\beta})^{*} = \chi_{\alpha}^{(+)}(\text{-}\mathbf{k}_{\alpha}, \mathbf{r}_{\alpha}) \tag{1.29}$$

The above wave functions can be found by solving the Schrödinger equation with known optical potentials. In the $\langle\varphi_b\varphi_B|\mathbf{U}|\varphi_a\varphi_A\rangle$ term, $\boldsymbol{U}$ is a transition potential and φ are the internal wave functions of the corresponding nuclei. Knowing that $A = b + x$, we can factorize the wave function φ_A as

$$\varphi_A(\zeta) = SF_{(B+x)}^{1/2}\varphi_B(\zeta)\varphi_x(\zeta)\Psi_{Bx}(\mathbf{r}_{Bx}) \tag{1.30}$$

where ζ are the internal coordinates of the nucleus, Ψ_{Bx} is the wave function describing the relative motion of B and x, and $SF_{(B+x)}$ is the spectroscopic factor giving the probability of finding nucleus A in the configuration B+x. With the same approach, we can factor the wave function φ_b as

$$\varphi_b(\zeta) = SF_{(a+x)}^{1/2}\varphi_a(\zeta)\varphi_x(\zeta)\Psi_{ax}(\mathbf{r}_{ax}) \tag{1.31}$$

where ζ are the internal coordinates of the nucleus, Ψ_{ax} is a wave function describing the relative motion of a and x, and $SF_{(a+x)}$ is a spectroscopic factor giving the probability of finding a nucleus b in the configuration a+x.

The reaction can be considered from the point of view of the entrance channel, which is called the *prior* representation, or from the point of view of the exit channel, which is called the *post* representation. Formally, both approaches yield identical results [13], but the availability of the optical potential in one of the channels can make one approach more viable. Depending on the representation, the transition potential $\mathbf{U}$ will be defined differently. In the prior representation, we have

$$U_{prior}(\mathbf{R}_{Aa}, \mathbf{R}_{Bx}) = V_{Bx}(\mathbf{R}_{Bx}) + U_{Ba}(\mathbf{R}_{Ba}) - U_{Aa}(\mathbf{R}_{Aa}) \tag{1.32}$$

where $U_{Bx}(\mathbf{R}_{Bx})$ is the binding potential of cluster x to nucleus B, $U_{Ba}(\mathbf{R}_{Ba})$ the optical potential between nuclei B and a, and $U_{Aa}(\mathbf{R}_{Aa})$ is the optical potential between nuclei A and a. The term consisting of the optical potentials $U_{Ba}(\mathbf{R}_{Ba})$

and $U_{Aa}(\mathbf{R}_{Aa})$ is called the remnant.

By analogy, for the post representation, we obtain

$$U_{post}(\mathbf{R}_{Bb}, \mathbf{R}_{ax}) = V_{ax}(\mathbf{R}_{ax}) + U_{Ba}(\mathbf{R}_{Ba}) - U_{Bb}(\mathbf{R}_{Bb}) \tag{1.33}$$

where $V_{ax}(\mathbf{R}_{ax})$ is the binding potential of cluster x to nucleus a, $U_{Ba}(\mathbf{R}_{Ba})$ the optical potential between nuclei B and a, and $U_{Bb}(\mathbf{R}_{Bb})$ is the optical potential between nuclei B and b. The term consisting of the optical potentials $U_{Ba}(\mathbf{R}_{Ba})$ and $U_{Aa}(\mathbf{R}_{Aa})$ is called the remnant. The choice of optical potentials in the entrance and exit channels strongly influences the result of the DWBA. In some cases, for example, when the interaction potential in the exit channel is unknown, one can approximate the remnant term as zero. In these cases, the transition amplitude will be determined mainly by the binding potential.

Chapter 2

Experimental details

The experimental part of this work was performed at the ACCULINNA-2 fragment separator in the Joint Institute for Nuclear Research in Dubna, Russia. The separator and the U400M cyclotron, which produced the primary beam, will be briefly described in section 2.1. The experiment will be detailed in section 2.2. Section 2.3 will outline the principle of operation of the beam monitoring detectors, and information regarding telescopes will be presented in section 2.4. Finally, a description of the Data Acquisition System (DAQ) will be provided in Section 2.5.

2.1 ACCULINNA-2 fragment separator

A fragment separator is a system of magnets placed around a beam line designed to filter out unwanted ions produced in the fragmentation reaction of the primary beam on the primary target. The primary beam usually consists of stable nuclei that are accelerated, for example, in a cyclotron and are then focused onto the primary target. As a result of the fragmentation reaction, a cocktail of ions is produced, among which the short-lived isotope of interest is present. The thickness of the target is chosen so that the newly created isotopes have the desired energy and to ensure sufficient intensity of the secondary beam. The resulting secondary beam is focused using magnetic lenses and guided through dipole magnets, which deflect the ion trajectory. By adjusting the magnetic field induction, we can allow ions with the desired A/Z ratio at a given velocity v to pass through. After cleaning,

the secondary beam is focused onto several focal planes where the beam can be monitored. Finally, the ions arrive at the reaction chamber, where they are focused onto the secondary target.

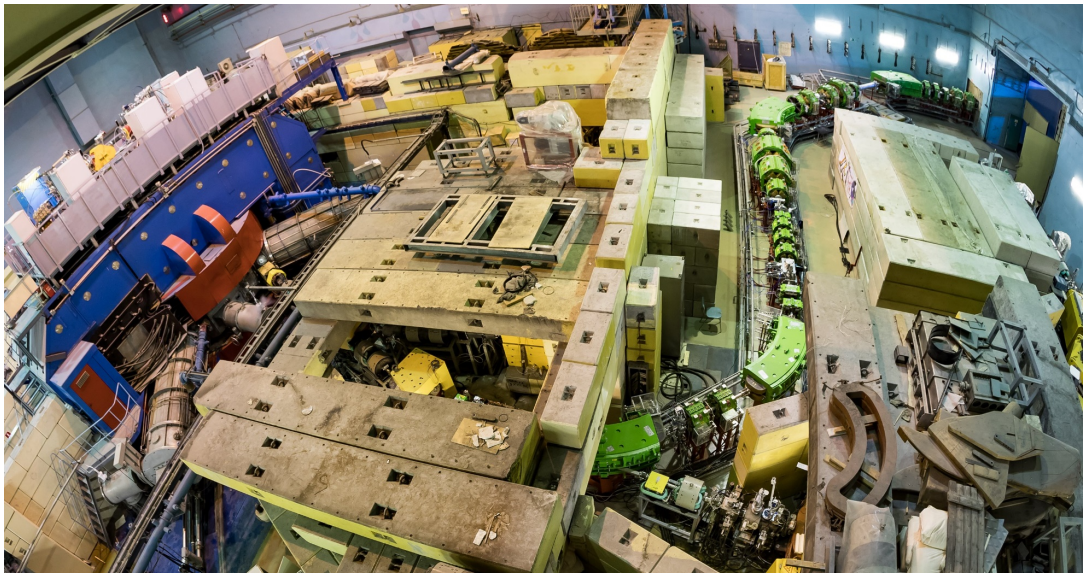

Figure 2.1: A view over the U400M cyclotron hall. The cyclotron is painted in red and blue on the left side of the photograph. The magnets of the ACCULINNA-2 fragment separator are painted green. The beamline passes through the cyclotron hall wall, visible in the upper right corner.

ACCULINNA-2 is a separator built in 2018 that operates with the U400M cyclotron at the Flerov Laboratory of Nuclear Reactions [14, 15]. A photograph of the cyclotron and ACCULINNA-2 is presented in Fig. 2.1, and the main characteristics of the separator are listed in Table 2.1. The measurements described in this work were carried out in March and April 2018 as the first physics experiment. During the experiment, the nitrogen isotope ^{15}N was ionized and pre-accelerated in the Electron Cyclotron Resonance (ECR) ion source. Subsequently, the ions were injected into the cyclotron. There they were further accelerated to an energy of 49.7 MeV/n with an average intensity of 1.4 µA. The ions were later directed into the ACCULINNA-2 and focused at a water-cooled rotating primary target made of natural beryllium with a thickness of 2 mm. Afterwards, the secondary beam, which included ^{6}He ions, was guided through two dipole magnets, between which a beryllium degrader was placed. The purified beam was then guided outside the cyclotron hall (presented in Figure 2.2), where it passed through the focal planes F3, F4, and F5 inside the reaction chamber, where it was focused onto the physical

target. After cleaning, the average beam intensity in the focal planes F3 and F5 was $2 * 10^4$ and 10^4 particles per second, respectively.

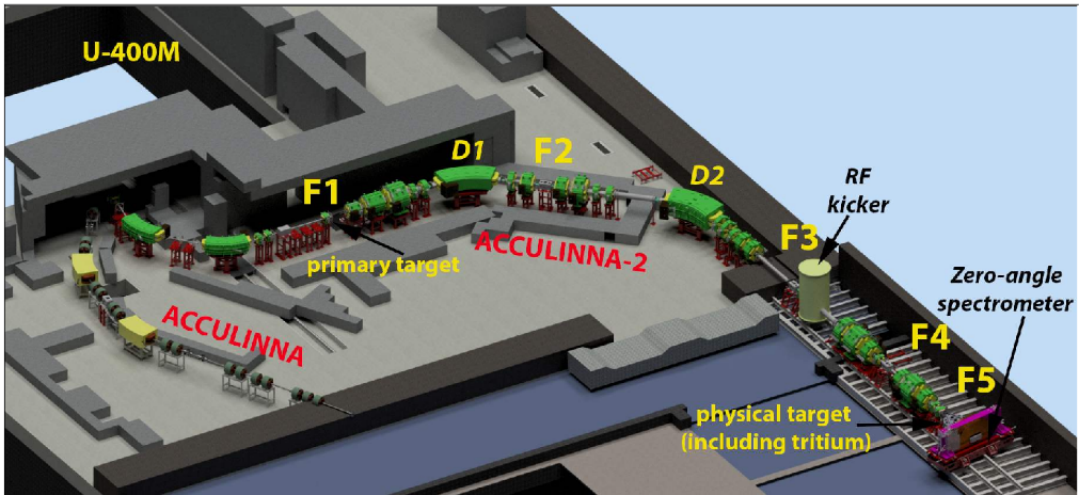

Figure 2.2: A drawing of the ACCULINNA-2 fragment separator. The focal planes are marked with the letters "F" and the dipole magnets with "D". The focal plane F3 is located outside the cyclotron hall, where the radiation levels are lower. The RF kicker and the zero-angle spectrometer were not used during the measurements.

Parameter	value
$\Delta\Omega$ [msr]	4.2
δ_P [%]	6.0
$P/\Delta P$	2000
$\beta\rho_{max}$ [Tm]	3.9
L [m]	37
E_{min} [AMeV]	5
E_{max} [AMeV]	50

Table 2.1: Basic characteristics of the ACCULINNA-2 separator, where $\Delta\Omega$ is the solid angle, δ_P - momentum acceptance, and $P/\Delta P$ – momentum resolution, respectively.

2.2 Experimental setup and procedure

The energy of the secondary beam was measured with a Time-of-Flight (ToF) detector, which consisted of two subdetectors: the first subdetector was located in the focal plane F3 and the second 12.32 meters downstream of the beamline before the focal plane F5. Multiwire Proportional Chambers (MWPCs) 1 and 2 were located upstream of the focal plane F5 at 81.6 cm and 27.0 cm, respectively. Mea-

suring the beam position in the MWPCs allowed for reconstruction of the beam trajectory and calculation of its position on the target plane. Figure 2.3 presents a schematic of the experimental setup. The deuterium target consisted of a deuterated

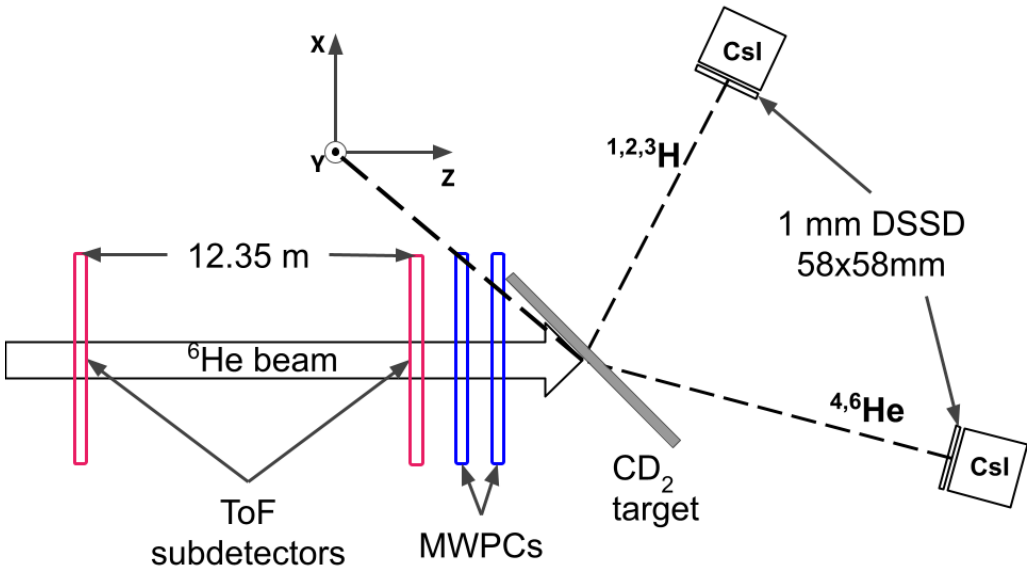

Figure 2.3: Schematic of the experiment. The X, Y, and Z axes in the laboratory coordinate system are defined as indicated in the Figure, with the center of the coordinate system at the center of the target. The ^{4,6}He (right) telescope was stationary throughout the experiment, while the ^{1,2,3}H (left) telescope position was changed.

polyethylene foil in an aluminum frame, as seen in the photograph of the experimental setup in Fig. 2.4. After the beam impinged on the target, multiple reactions occurred, predominantly elastic scattering on protons, deuterons, and carbon. The reaction product energies and positions were measured with two identical telescopes, each consisting of a 1 mm thick Double-Sided Silicon Detector (DSSD) and a CsI(Tl) scintillator detector. The DSSD allowed for the precise measurement of the particle energy loss in the detector and the position where it hit the detector. The scintillator detectors were thick enough to stop the reaction products and measure their remaining energy. Knowledge of the beam position and its vector at the target plane and the reaction product position in the telescopes allowed for the complete reconstruction of the reaction geometry. The time-of-flight and the energy loss of the beam in the ToF F5 subdetector allowed for the identification of beam ions, while $\Delta E - E$ spectra from the telescopes enabled a further data cleaning process. The experiment was designed assuming that the reaction products of elastic scattering and transfer reactions would be detected in coincidence. The telescopes were placed

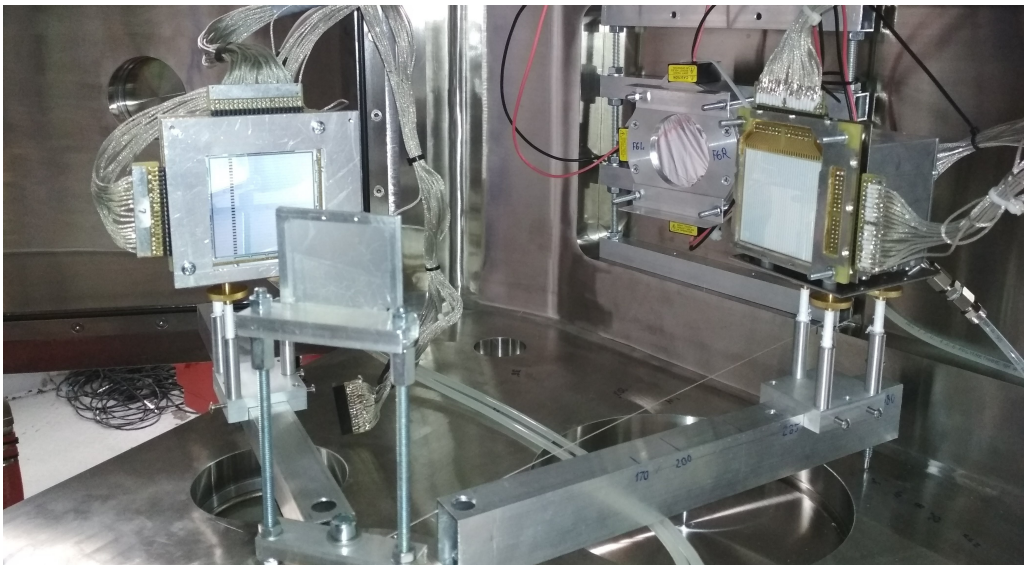

Figure 2.4: A photograph of the experimental setup inside the reaction chamber. The CD_2 target is at the front, and the left and right telescopes are in the background.

on the left and right sides of the optical axis to achieve this. The laboratory system of coordinates used during the experiment is defined in Figure 2.3 with the optical axis parallel to the Z axis.

The right telescope was positioned 25.0 cm from the target at an angle of 15° to the optical axis and was stationary throughout the measurement. It covered the angular range from 5° to 25° in the laboratory system of coordinates, which allowed for the detection of the elastically scattered ^{6}He and 4He originating from the transfer reaction.

The left telescope was positioned at 17.0 cm at three different angles, which were changed throughout the measurement to cover a wider angular range. Both telescopes were rotated so that they faced the target.

Along with the left telescope position, the target thickness and the angle at which it was placed were changed. In the first geometry, the target was 100 µm thick and was rotated around the Y axis at 45° so that it faced the left telescope. This increased its effective thickness and decreased the energy loss of the scattered protons and deuterons. A summary of the angles at which the left telescope was positioned, the angle of the target rotation, and the target thickness is presented in Table 2.2. In the second and third geometries, reaction products had sufficiently

high energy, so the target faced the optical axis and another 100 µm thick foil was added.

Geometry	Left telescope angle [deg]	Left telescope angular range	Target thickness [µm]	Target angle [deg]
1	65.3	75 - 55	100	45
2	50	40 - 60	200	6
3	35	25 - 45	200	0

Table 2.2: Experimental setup parameters for different geometries. The right telescope was stationary throughout the experiment.

2.3 Beam detectors

2.3.1 Multi-wire proportional chamber

The MWPC is a gaseous detector working in the proportional region, which means that the electrical signal produced in the detector has an amplitude proportional to the energy deposited in its volume. When an ionizing particle penetrates the gas, it collides with an inert gas atom, leading to ionization and the formation of an electron and a positively charged ion, referred to as an "ion pair".

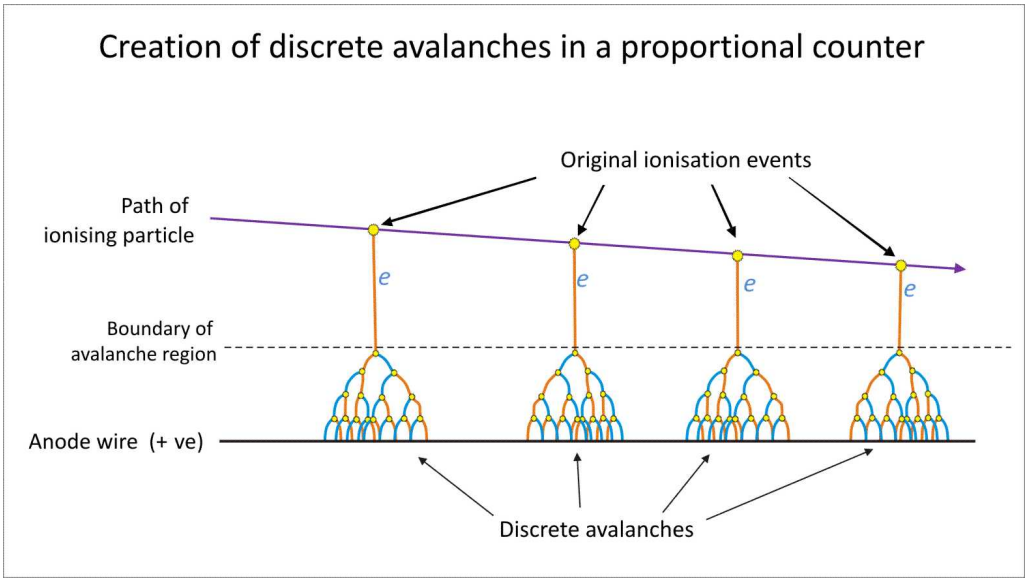

Figure 2.5: A visualization of how electron avalanches are formed in MWPC detector.
By Dougsim, CC BY-SA 3.0,
https://en.wikipedia.org/wiki/File:Proportional_counter_avalanches.jpg

The ionizing particle creates a path of these ion pairs as it moves through the chamber. The number of ion pairs generated is directly related to the energy deposited by the particle in the gas volume. The detector's specific geometry and applied voltage maintain a low electric field in most areas, functioning like an ion chamber. However, the field strength is sufficient to prevent ion pair recombination, causing positive ions to drift toward the cathode and electrons toward the anode in the "ion drift" region. Close to the anode wire, a high electric field accelerates the electron, which knocks out other electrons, triggering Townsend avalanches [16] within a fraction of a millimeter. Figure 2.5 presents a diagram illustrating the operation of a gas proportional detector. This localized avalanche region, near the tiny anode wire, utilizes the multiplication effect of each ion pair avalanche. A crucial design objective is to ensure that each initial ionizing event results in just one avalanche. This guarantees proportionality between the original events and the total ion current. Controlling parameters like the applied voltage, chamber geometry, and anode the wire diameter is vital to maintain this proportional operation. The counter enters a "limited proportionality" state if avalanches start self-multiplying due to ultraviolet photons.

Further increase in the applied voltage leads to Geiger discharge, causing complete ionization of the gas around the anode wire and loss of particle energy information. The electronic signals are collected independently from each wire, which allows identification of the place in the detector where the charged particles passed through. When two detectors are placed on a beamline, it is possible to reconstruct the particle vector and its position at the target plane.

There are two identical MWPCs at ACCULINNA-2, numbered 1 and 2, with MWPC 1 the first on the beam path. A detector features two sets of stainless steel anodes 6 µm thick, each coupled with a grid of parallel wires placed every 1.25 mm. The wires are made of tungsten and are 20 µm in diameter. There are 32 wires in one grid, and one grid is rotated 90° around the beam axis to provide information about beam position in two dimensions. The entrance and exit windows in the detector body are covered with a 25.4 µm thick Kapton foil, which keeps the chamber hermetic. The chamber is filled with the carbon tetrafluoride (CF_4) gas

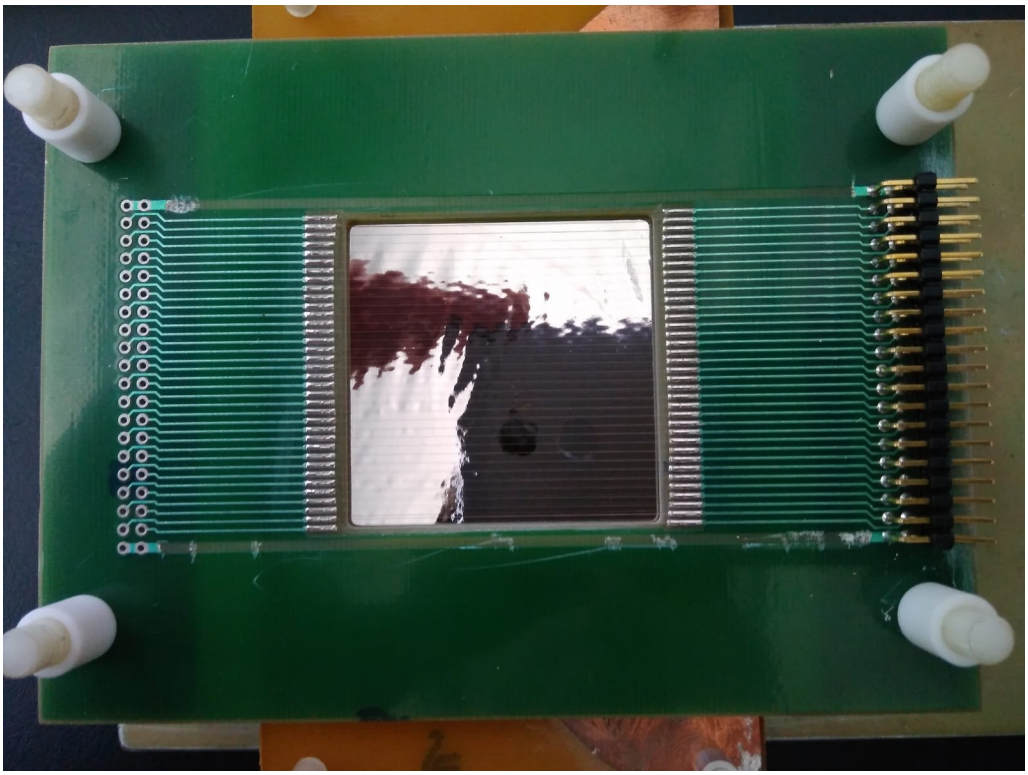

Figure 2.6: A photograph of the MWPC wires mounted on a PCB with the stainless steel cathode located below the wires. During the experiment, the wires were placed in a stainless steel cover.

at atmospheric pressure. A photograph of the MWPC wires and the stainless steel cathode without the detector cover is presented in Figure 2.6

2.3.2 Time-of-flight detector

The time-of-flight detector allows the measurement of the velocity of a particle by measuring its flight time over a known distance. Simultaneous measurement of the energy loss of a particle in one of the subdetectors allows for the creation of a two-dimensional plot (ΔE-ToF plot) which enables ion identification. An example of a plot created with the data from this measurement is shown in Figure 2.7. Given the velocity of the particle and its mass, its kinetic energy can be calculated, which is essential when measuring the energy of excited states, while in the case of this measurement, the main task is to identify ^{6}He in the incoming secondary beam. The time-of-flight detector installed at the ACCULINNA-2 consists of two fast scintillator subdetectors[1]. The distance between the subdetectors is 12.32 m, which allows

[1]The principle of the operation of a scintillator detector will be described in section 2.4.2

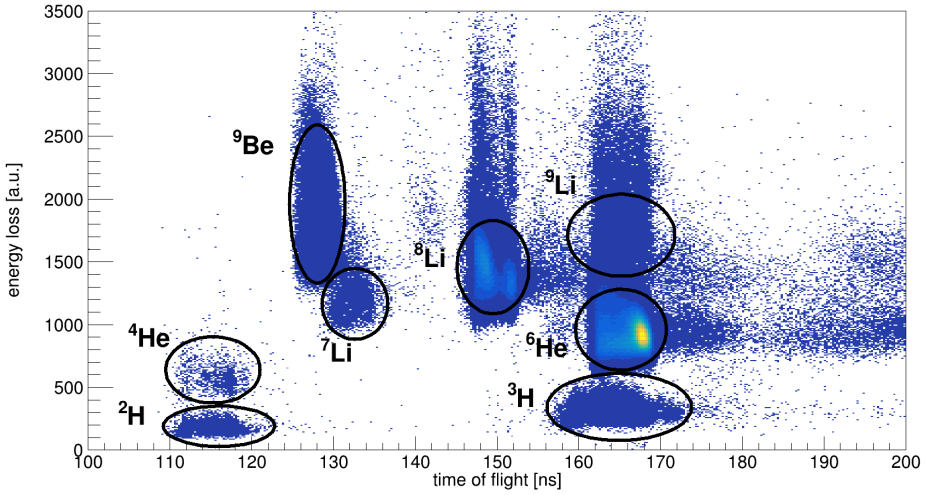

Figure 2.7: ID plot with individual ions collected in this experiment marked.

a high time resolution. Photographs of the interior of one of the subdetectors and a subdetector mounted on the beamline are shown in Figure 2.8.

A single detector consists of four photomultipliers (PMTs) arranged on a cross plan, as shown in Figure 2.8a. Hamamatsu R7600U-200 PMTs coupled with Hamamatsu E5996 voltage dividers were used in the experiment. Each photomultiplier was powered by a separately controlled voltage adjusted so that the signal amplitude from a given ion was at the same level for a given detector. The distance between the fronts of the PMTs was 50 mm, which was also the diameter of the entrance window. Aluminum blocks were placed between the photomultipliers to keep the structure rigid and ensure light tightness. A plastic scintillator was placed on the mounting ring and bolted to the subdetector body. A fast, plastic scintillator

Properties	EJ-212
Light Output (% Anthracene)	65
Wavelength of Maximum Emission [nm]	423
Rise Time [ns]	0.9
Decay Time [ns]	2.4
Pulse Width, FWHM [ns]	2.7
Density [g/cm^3]	1.023
Polymer Base	Polyvinyltoluene
Refractive Index	1.58

Table 2.3: Basic characteristics of the EJ-212 plastic scintillator taken from the manufacturer's website.

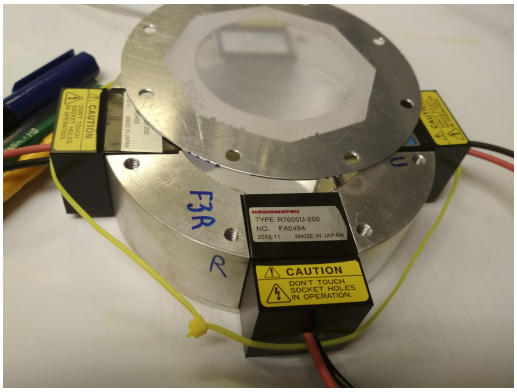

(a) ToF F3 subdetector used in the experiment during the assembly process. The PMTs will be wrapped in copper tape for better heat transfer to the detector body and are numbered for easier identification. At the bottom of the detector, a mylar foil prevents light from escaping the body. The matted EJ-212 plastic scintillator taped to the holder ring is placed on top of the detector.

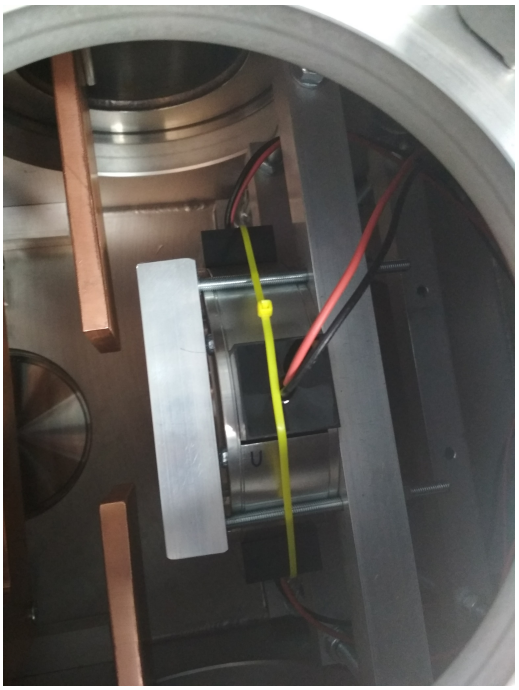

(b) A side view of the ToF subdetector mounted in the diagnostic box in the focal plane F3.

Figure 2.8: ToF subdetector F3 during assembly and mounted on the beamline.

by Eljen Technology, model EJ-212, was used in both subdetectors as scintillating material. The main parameters of EJ-212 are given in Table 2.3. Both plastic scintillators were matted on both sides for even light distribution in the detector volume. After matting, the thicknesses of the plastics were measured: 111 micrometers in the focal plane F3, and 235 micrometers in the focal plane F5.

Properties	Value
Effective area	18 mm x 18 mm
Spectral range [nm]	300 to 650
Peak wavelength [nm]	400
Maximum voltage [V]	900
Gain	2.0×10^6
Rise time [ns]	1.6
Transit time [ns]	9.6
Transit time spread [ns]	0.35

Table 2.4: Basic characteristics of the R7600-200 photomultiplier taken from the manufacturer's website.

The ion identification and calibration procedure of the ToF detector will be described in section 3.2.3 in chapter 3.

2.4 Telescopes

2.4.1 Silicon detectors

A silicon semiconductor detector is based on a reverse-biased p-n junction. The applied voltage is high enough to ensure that the depletion zone is stretched over the whole body of the silicon material. A charged particle passing through the depletion zone creates electron-hole pairs moving toward the electrodes. A fast

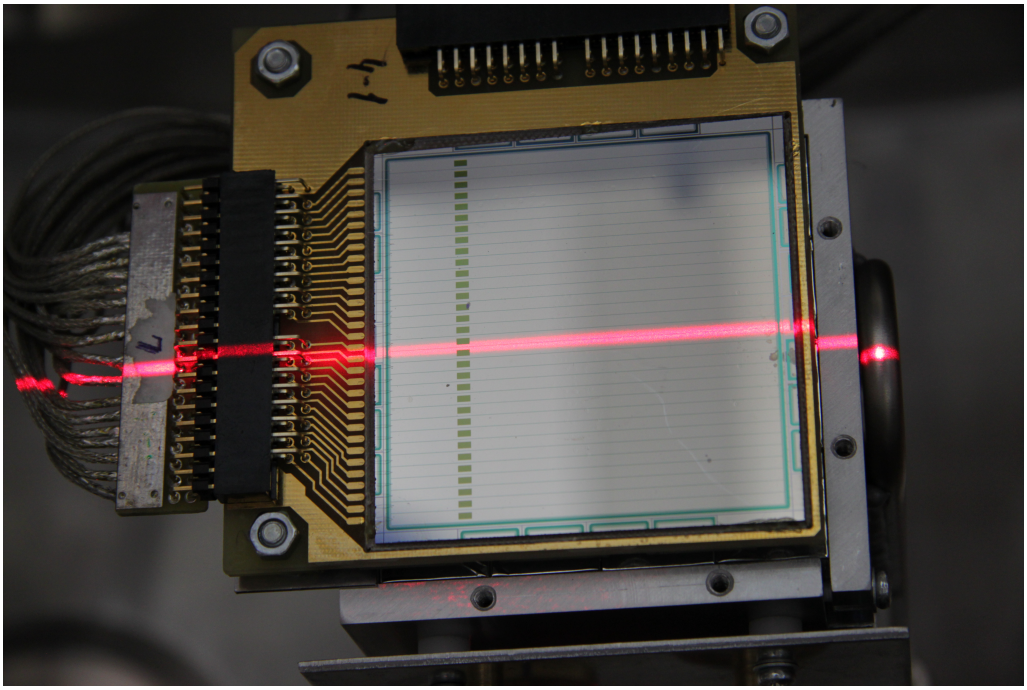

Figure 2.9: DSSD mounted on the left telescope during positioning with a laser level. The horizontal electrodes are facing the target.

electronic signal is amplified and read by an analog-digital converter. The signal is proportional to the energy loss of the particle in the detector and, due to the fast charge collection, has a higher time and energy resolution than scintillator detectors. With the progress in semiconductor production techniques, it is possible to produce detectors with thicknesses ranging from tens of microns to a couple of millimeters. It is also possible to utilize multiple electrodes on the detector surface, allowing the collection of information not only on the energy and time but also on the position

where the signal originated.

Two square, 1 mm thick Double-Sided Silicon Detectors were utilized in the experimental setup used for this measurement. The detectors were mounted on the left and right telescope and had an active area of 58x58 mm^2 and 32 electrodes on each side. The electrodes had the form of strips 1.8125 mm wide, with the strips on one side being oriented perpendicularly to the strips on the opposite side. A photograph of the DSSD used in the left telescope is presented in Figure 2.9.

The calibration procedure of the DSSD detectors will be described in section 3.2.1 in chapter 3.

2.4.2 CsI array

A scintillator detector consists of a scintillating material plus an attached photomultiplier tube. The scintillating process in inorganic crystal scintillators occurs when an ionizing particle excites electrons, which emit light quanta when they deexcite. In order to minimize reabsorption of the emitted light, impurities called activators are introduced into the crystal lattice. As a result, new energy levels within the forbidden gap are created locally. Excited electrons drift to the sites with the

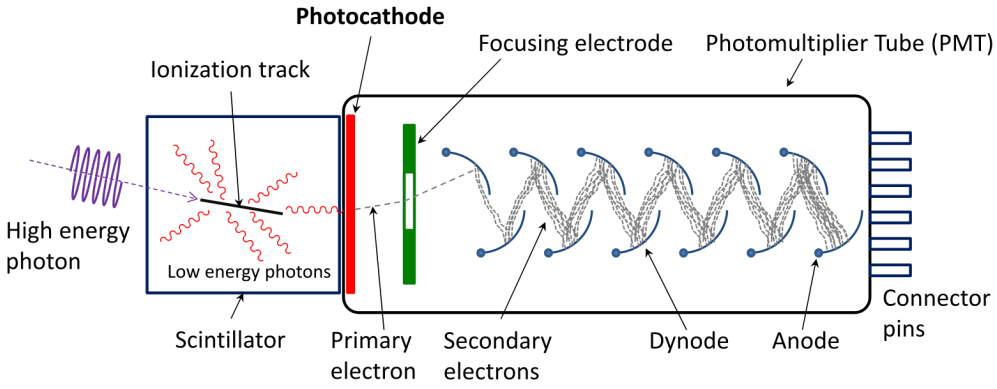

Figure 2.10: Principle of operation of a scintillator detector coupled to a photomultiplier tube. The ionizing radiation in the schematic has the form of a high energy photon, whereas it was a charged particle in the experiment.
By Qwerty123uiop, CC BY-SA 3.0,
https://commons.wikimedia.org/w/index.php?curid=62426194

impurities and recombine there, emitting light shifted towards longer wavelengths, which are not absorbed by the bulk of the crystal. The photons transfer their energy

to electrons in the photocathode, causing the electrons to be emitted and accelerated in the electric field inside the PMT. The electrons hit the first dynode, causing more electrons to be emitted. The process is repeated several times, after which the electronic signal is amplified by several orders of magnitude. A schematic of how a scintillator with a photomultiplier tube works is presented in Figure 2.10.

In the experimental setup there were two identically designed thallium-activated cesium iodide crystal (CsI(Tl)) detectors, each mounted in one of the Telescopes. One detector consisted of a 4x4 array of CsI(Tl) crystals wrapped in 3.5 µm thick mylar foil to prevent light crosstalk between crystals. One crystal was 16.5 mm x 16.5 mm x 64 mm and was coupled with a R9880U-20 PMT by Hamamatsu, which allowed for individual readout channels for every crystal. The crystals and the PMTs were enclosed in a water-cooled metal case shown in Figure 2.11.

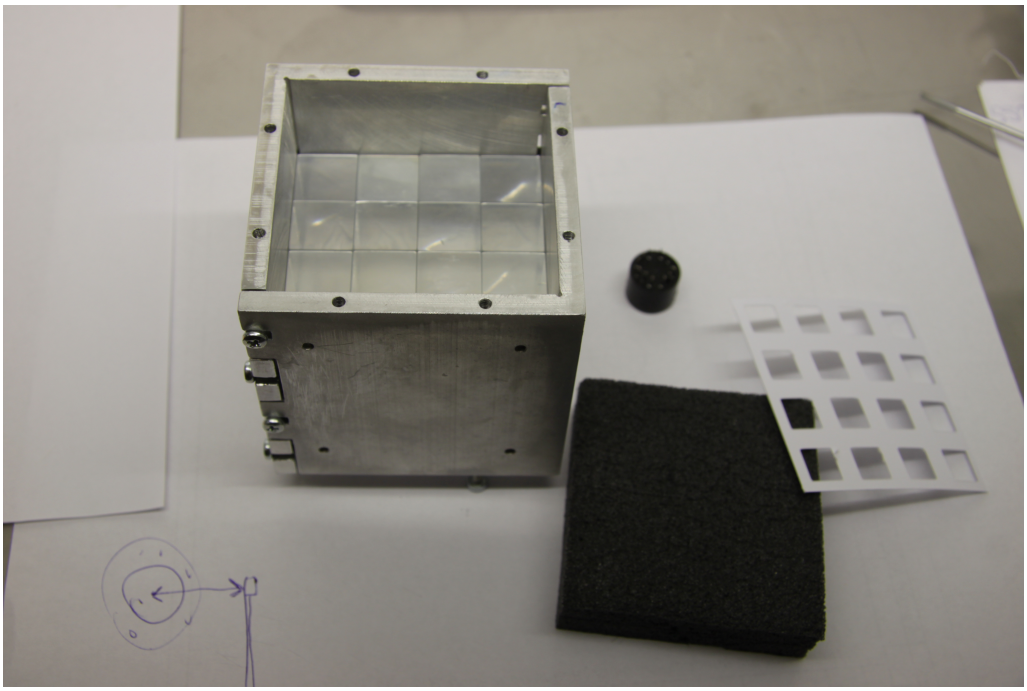

Figure 2.11: The CsI(Tl) crystals in the metal casing. Each crystal is wrapped in mylar foil to reduce light crosstalk between the crystals. The white mask on the right side of the photograph will be placed on the crystals and the PMTs will be mounted on top of it.

The thickness of the crystals was enough to stop the particles that passed through the DSSD, allowing us to make a 2D $\Delta E - E$ plot. The plot was used to identify ^{6}He ions. The calibration procedure of the CsI(Tl) detectors will be described in section 3.2.2. and the ^{6}He identification process will be described in

Properties	Value
Effective area [mm]	ϕ 8.0
Spectral range [nm]	230 to 920
Peak wavelength [nm]	630
Maximum supply voltage [V]	1100
Gain	2x10^6
Rise time [ns]	0.57
Transit time [ns]	2.7
Transit time spread [ns]	0.2

Table 2.5: Basic characteristics of the R7600-200 photomultiplier taken from the manufacturer's website.

section 3.3.1.

2.5 Data Acquisition System

The beam monitoring detectors and reaction products at ACCULINNA-2 are integrated within one distributed multi-processor data acquisition system based on the Multi Branch System (MBS) [17]. The electronics used the VME [18] standard with one CAMAC [19] crate. The scheme of the DAQ is presented in Figure 2.12.

Three different sources of trigger signals were defined in the data acquisition system applied to ACCULINNA-2 during the measurements described in this work. Upon reaching the controller when idle, the trigger signal caused a temporary cessation of acceptance of subsequent trigger signals. The trigger signal originating from the beam was designated "beam trigger," the signal from the telescopes "experimental trigger," and the signal exiting the controller "accepted trigger." The "accepted trigger" was then delivered to analog-to-digital converters, leading to the recording of amplitudes registered by amplitude sensing analog-to-digital converters (ADC) and charge integrating analog-to-digital converters (QDC), as well as the time signals recorded by the time-to-digital converter (TDC). Details of the readout of individual detectors will be described below.

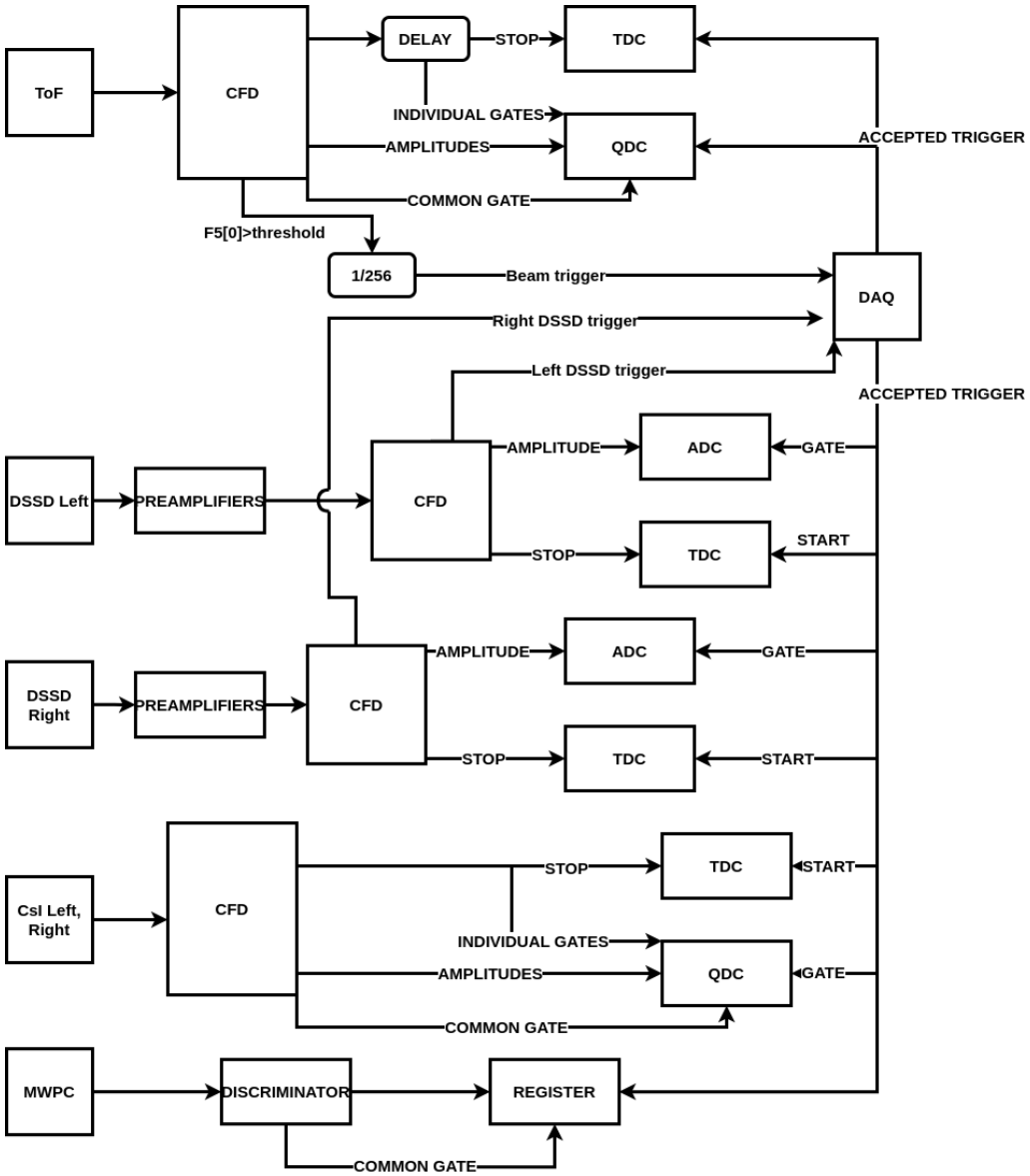

Figure 2.12: A schematic of the data acquisition system at ACCULINNA-2.

2.5.1 ToF

Analog signals from both ToF subdetectors PMTs directly reached a constant fraction discriminator (CFD) that had time and amplitude outputs. The output time signal was delayed and used as:

- The signal responsible for generating individual time gates for the signal from each photomultiplier in the ToF subdetectors, fed to the QDC
- the STOP signal for the TDC

The CFD shaped and amplified amplitude signals and then fed into the QDC. At the

same time the CFD generated a "common gate" for the QDC, and in the case when the signal from the first PMT subdetector ToF F5 exceeded a threshold (marked as F5[0]), it generated the "beam trigger" signal. This signal was then sent to a scaler, which allowed 1 in 256 signals to pass through to the acquisition system, generating the "beam trigger" signal.

The QDC integrated incoming amplitude signals from the ToF subdetectors in the time frame according to the individual gates, and upon receiving the "accepted trigger" signal, the common gate saved the integration results to the buffer.

The TDC measured the time between the "accepted trigger" and the delayed time signal from the CFD, which originated from the ToF subdetectors.

2.5.2 DSSD

Signals from the DSSDs were preamplified and then fed to a shaping amplifier and integrated with the CFD. The CFD generated an "experimental trigger" signal when the signal amplitude in any of the channels was over the threshold. Depending on whether the signal originated from the left telescope DSSD or the right telescope DSSD, it was saved in the data file with a different ID, but both signals functioned in the DAQ in the same way. The CFD output amplitude signals to the ADC with the gates generated based on the "accepted trigger signal" and saved the data to the buffer. The CFD output time signals were fed to the TDC and served as the STOP signal, with the "accepted trigger" as the START signal.

2.5.3 CsI

The signals from the PMTs of the CsI(Tl) detectors were fed into the CFD, which generated the "common gate" for the QDC, "individual gates" for the QDC, a STOP signal for the TDC, and the amplitude signal for the QDC. The principle of operation of the TDC and the QDC was the same as for the ToF subdetectors.

2.5.4 MWPC

The signals coming from the MWPC were fed into the discriminator, which, upon receiving a signal from any wire that was above the threshold, generated a "common gate" for the register. At the same time, the discriminator generated a logical signal for each wire with the signal above the threshold and passed it to the register. Upon receiving the "accepted" trigger within a specified time window, the registers were saved to the buffer and self-cleaned. After 1 µs, the register was self-cleaning if no trigger signal was received.

The detector responses from the ADC, QDC, and TDC were collected and formed an event. A group of events which filled the control unit buffer was sent to the computer and saved on the hard drive in .lmd file format. In addition to the detector responses, the trigger signal ID was also recorded. The data stream to the computer was monitored online using go4 [20] software to ensure beam focusing and monitoring of the quality of the collected data. After the measurement, the data files in the .lmd format were converted to the .root [21] format using go4 software.

Chapter 3

Data analysis

This chapter will describe the procedure for analyzing the experimental data collected during the experiment. Section 3.1 will describe the structure of the data and the tools used for the analysis. The procedure for calibrating the detectors (section 3.2) and the methods of data cleaning and reduction (section 3.3) will then be presented. The Monte Carlo simulation used to calculate the registration efficiency of the system will be described in section 3.4. The last step is described in section 3.5, where the method for calculating the elastic scattering and transfer cross sections is presented. The data were analyzed using the ROOT [21] framework, version 6.26/00, in the C++ standard C++14 programming language. The code written for data analysis is not attached to this work due to its length but is available on GitHub under the links:
https://github.com/guar1337/analysis
https://slcj.uw.edu.pl/codes/analysis

3.1 Data handling

The first step in the analysis process was initial data cleaning. Events that were not suitable for later interpretation were dismissed based on the criteria described below:

- **Invalid signals in MWPCs** An insignificant number of events contained

wrong values in the array containing the ID of the fired wire. The data analysis script could not process these events, so they had to be removed.

- **Time difference between signals from individual PMTs of the ToF subdetector** Depending on where the beam particle hit the scintillator, the timestamps in different PMTs in one of the ToF subdetectors differ. This difference is well-defined and is limited by an extreme condition in which an ion hits the very edge of the scintillator. Events where this time difference between signals was exceeded had to be removed since the actual energy of the particle could not be determined.

- **Multiple clusters in the MWPC** The MWPCs used in the experiment were designed to accept and adequately detect hits from multiple wires. If an event with multiple hits was recorded, it usually means that a beam particle ionized the gas somewhere between two wires. Both wires collected the charge, and two signals emerged. The estimated beam position was shifted toward the area between the wires and not around the wire, as in the case of a single hit event. Nevertheless, multiple MWPC hits were separated by an inactive wire in some events. This kind of event could not be processed and was removed since estimating an actual beam position passing through the MWPC was impossible.

- ^{6}He **in the beam** Despite the two-step beam separation process, there was still a cocktail of incoming ions in addition to ^{6}He. A ToF range corresponding to the region with ^{6}He was chosen in order to remove events that, in the later analysis, could be falsely identified with reactions of interest. The applied cut is presented in Figure 3.1

- **Signal in the left and right silicon detectors** One of the main criteria used for reaction identification was the coincidence of the reaction products. Therefore, removing events from the analysis with no signal above the threshold in both telescopes is safe.

After pre-cleaning, 0.2%, 0.05%, and 0.15% of the data were left in the first, second, and third geometry, respectively. The experimental data that passed the above

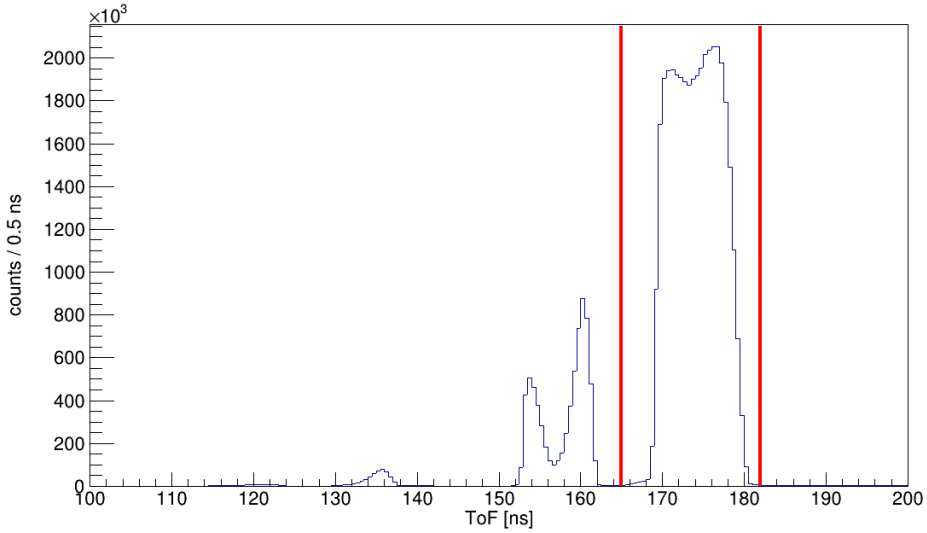

Figure 3.1: Time of Flight between focal planes F3 and F5. The peak corresponding to the ToF of ^{6}He is between the red lines and was selected for further analysis.

tests, apart from the **Signal in the left and right silicon detectors**, were saved to a separate .root file. This file was used to calculate the total beam flux in each geometry and as input for the Monte Carlo simulation.

3.2 Detector calibration

The amplitudes of the signals from the detectors have values expressed in channel units. In order to obtain spectra with physical meaning, these amplitudes need to be converted into energies. For the silicon detectors, a linear approximation was used with a correction for the dead layer of the detector. In the case of the CsI-based detectors, a linear approximation was also used, but no correction was made for the Mylar foil at the entrance of the detector. This correction is negligibly small compared to the resolution of the detectors. For the ToF detector, a TDC channel width correction was applied, and the ToF constant was obtained. The multi-wire proportional chamber positioning was performed for increased beam tracking accuracy.

3.2.1 Silicon detectors

The energy calibration of the silicon detectors is based on the assumption that the relationship between the signal amplitude and the energy loss in the detector is linear [16]:

$$energy\ [MeV] = A * channel + B$$

where A and B are parameters obtained from the fit. A ^{226}Ra alpha source was

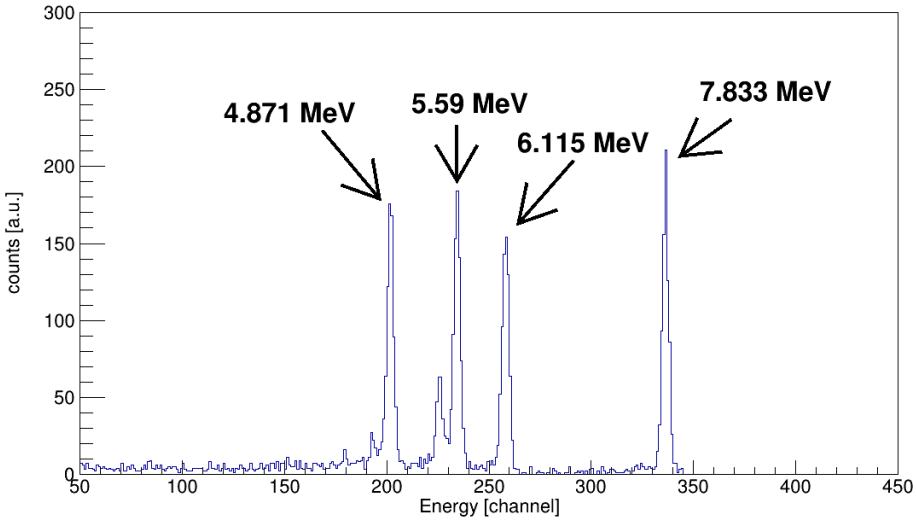

Figure 3.2: ^{226}Ra alpha particle energy spectrum.

used for the calibration. The source emits alpha particles with five different energies [22], presented in Fig. 3.2. Due to the low intensity and proximity to a more intense peak, the peak at 5.407 MeV was not used for calibration. The alpha particle energy emitted from the source had to be corrected for the source thickness and the detector dead layer. A summary of the energies is presented in Table 3.1.

Alpha decay energy	**Alpha energy after the source thickness correction**	**Alpha energy after Left DSSD dead layer correction**	**Alpha energy after Right DSSD dead layer correction**
4.871 MeV	4.751 MeV	4.210 MeV	4.218 MeV
5.407 MeV	not used	not used	not used
5.590 MeV	5.459 MeV	4.965 MeV	4.972 MeV
6.115 MeV	5.972 MeV	5.512 MeV	5.519 MeV
7.833 MeV	7.661 MeV	7.271 MeV	7.276 MeV

Table 3.1: Alpha particle energies from^{226}Ra used for silicon detector calibration.

The dead layer is the surface part of a silicon detector from which no elec-

tronic signal is collected when a charged particle passes through it. It is essential to assess the thickness of the dead layer properly to calibrate the detector and later evaluate the actual energy of a charged particle passing through it. The detector dead layer was adjusted so that the ADC noise level read corresponded to the zero energy deposited in the detector. This procedure was performed for both silicon detectors by averaging signals from all the strips for each of them. For the left DSSD, the dead layer value was 3.5 micrometers, and for the right DSSD, it was 3.45 micrometers.

It is worth mentioning that the dead layer of the detector is not uniform for the entire surface and may differ for individual strips. However, these differences do not that significantly affect the results. On the other hand, the electrical signal from each strip goes through its independent channel, and the differences in the obtained amplitude can be larger. The α-particle spectrum observed in the left DSSD after calibration is presented in Figure 3.3

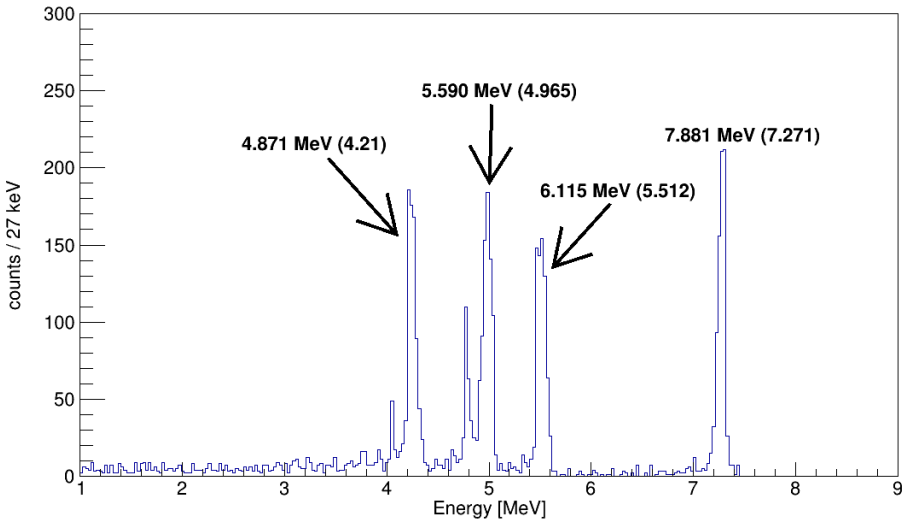

Figure 3.3: ^{226}Ra alpha particle energy spectrum observed in the left DSSD. The values are alpha decay energies, and the values in brackets are the observed energies obtained through peak fitting.

The position of the particle in the left DSSD was calculated by adding the position of the strip in the detector reference frame to the position of the zero strip

in the laboratory reference frame according to the formula

$$X_L\ [mm] = d_L * sin(\alpha_L) + w_X * 15.5 * cos(\alpha_L) - w_X * stripX_{ID} * cos(\alpha_L)$$
$$Y_L\ [mm] = -w_Y * 7.5 + w_Y * stripY_{ID}$$
$$Z_L\ [mm] = d_L * cos(\alpha_L) - w_X * 15.5 * sin(\alpha_L) + w_X * stripX_{ID} * sin(\alpha_L)$$

where d_L is the distance of the center of the left DSSD from the target, α_L is the angle at which the left telescope is positioned, w_X and w_Y are the widths of the vertical and horizontal strips in the left DSSD and $stripX_{ID}$ and $stripY_{ID}$ are the numbers of the vertical and horizontal strips where the particle was detected. The widths of the X and Y strips are different, because one electronic channel was connected to two Y strips.

By analogy, the position of the particle in the tight DSSD was calculated according to the formula

$$X_R\ [mm] = d_R * sin(\alpha_R) + w_X * 15.5 * cos(\alpha_R) - w_X * stripX_{ID} * cos(\alpha_R)$$
$$Y_R\ [mm] = -w_Y * 7.5 + w_Y * stripY_{ID}$$
$$Z_R\ [mm] = d_R * cos(\alpha_R) - w_X * 15.5 * sin(\alpha_R) + w_X * stripX_{ID} * sin(\alpha_R)$$

where d_R is the distance of the center of the right DSSD from the target, α_R is the angle at which the right telescope is positioned, w_X and w_Y are the widths of the vertical and horizontal strips in the right DSSD and $stripX_{ID}$ and $stripY_{ID}$ are numbers of the vertical and horizontal strips where the particle was detected.

3.2.2 Scintillator detectors

The light response of CsI(Tl) scintillating crystal to an ionizing charged particle with atomic number Z and mass number A is non-linear with respect to the incident energy E_0, depending on the atomic numbers Z and A [16]. This results in a formula [23] with multiple parameters that must be fit to a set of data points from a wide range of energies and, ideally, different ions. For the measurements described in this thesis, precise knowledge of the particle energy measured by the detector is unnecessary. However, identifying the detected ion with a $\Delta E - E$ plot

is essential. To achieve this, it is sufficient to group loci created for each crystal and a calibrated silicon detector. For this purpose, a linear function based on two data points was considered sufficient for the calibration procedure. One of the two points chosen was the ^{6}He beam energy after passage through the DSSD with the telescope positioned directly on the beamline with no target present. The second point used was the QDC readout of a signal with no energy deposited in the detector. The beam energy used to calibrate the detector was calculated from the time-of-flight of the ^{6}He nuclei. After obtaining the ion energy, it was corrected for the energy losses in the plastic scintillator at the exit from the ToF F5 subdetector and two MWPCs. As a result, the $\Delta E - E$ energy spectra from different crystals created an overlapping locus, which allowed for more precise isotope identification. The resulting $\Delta E - E$ spectrum from different crystals gathered together is presented in Figure 3.4

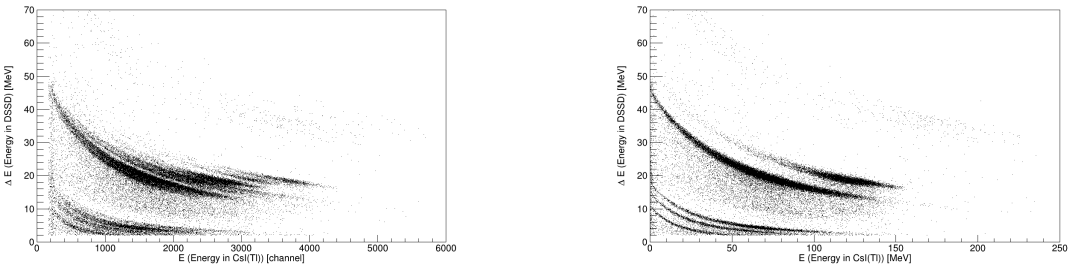

(a) Uncalibrated (b) Calibrated

Figure 3.4: $\Delta E - E$ spectra in the right telescope before calibration (a) and after calibration (b).

3.2.3 Time of flight detector

The ToF detector provides the time-of-flight of the particle between the subdetectors at focal planes F3 and F5 of the separator - timestamps tF3 and tF5, respectively. This time, unique for each beam ion is then used to calculate the particle energy at the target. The time-of-flight can be calculated with the formula

$$ToF\ [ns] = (\overline{tF5} - \overline{tF3}) * channel\ width\ [ns] + ToF\ constant\ [ns] \tag{3.1}$$

where:

- $\overline{tF3}$ **and** $\overline{tF5}$ are the average time stamp from each subdetector. Obtained by

averaging time stamps over photomultipliers.

- **channel width** is a scaling factor used by the TDC module. In this experiment, the channel width was equal to 0.125 nanoseconds per channel.

- **ToF constant** is the difference between the times measured in the ToF subdetectors that is not caused by the particle flight time. This constant does not change during the experiment and is caused by the difference in the length of signal cables and delays in the measurement electronics.

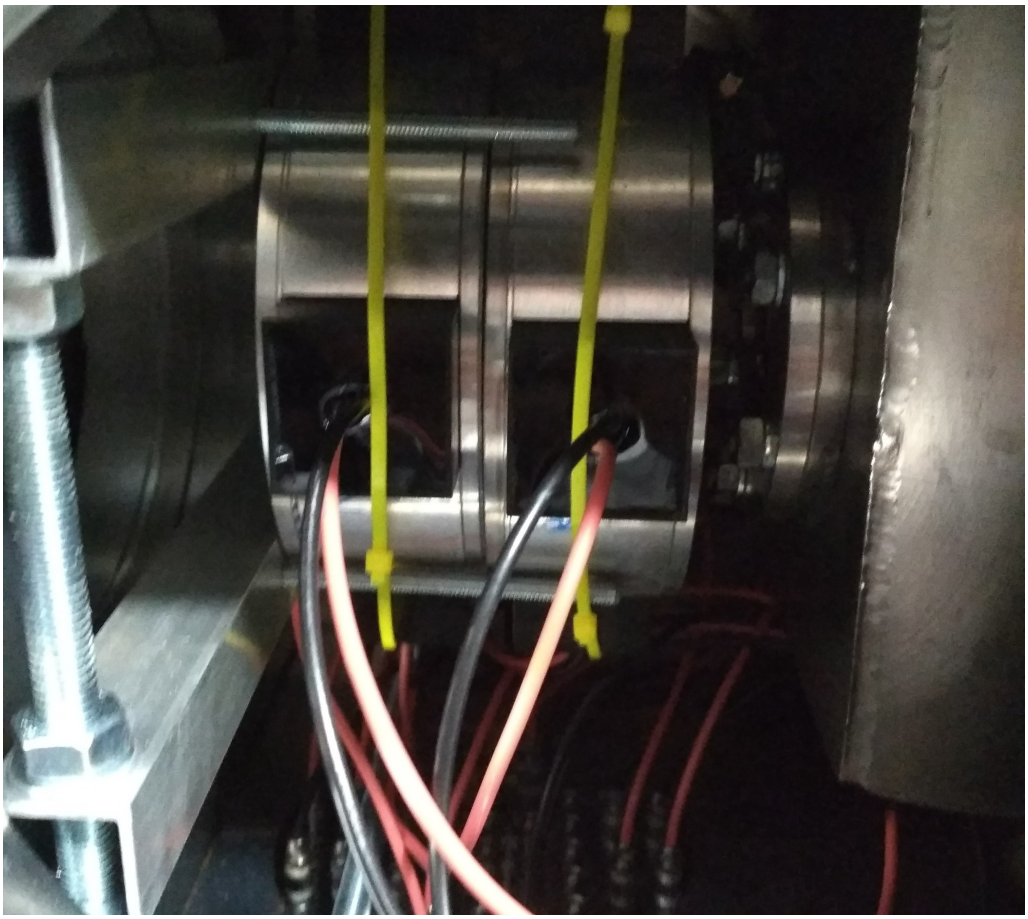

Figure 3.5: ToF subdetectors positioned at focal plane F5 for the ToF detector calibration measurement.

The channel width of the TDC electronics block was a programmable value and did not require determination. Therefore, the time-of-flight detector calibration was based on calculating the ToF constant. The experimental setup allowed for the physical movement of the subdetector located at the F3 focal plane to the diagnostic box at the F5 focal plane so that the two subdetectors were located side by side. A photograph showing the two ToF subdetectors positioned for the ToF detector

calibration measurement is presented in Figure 3.5.

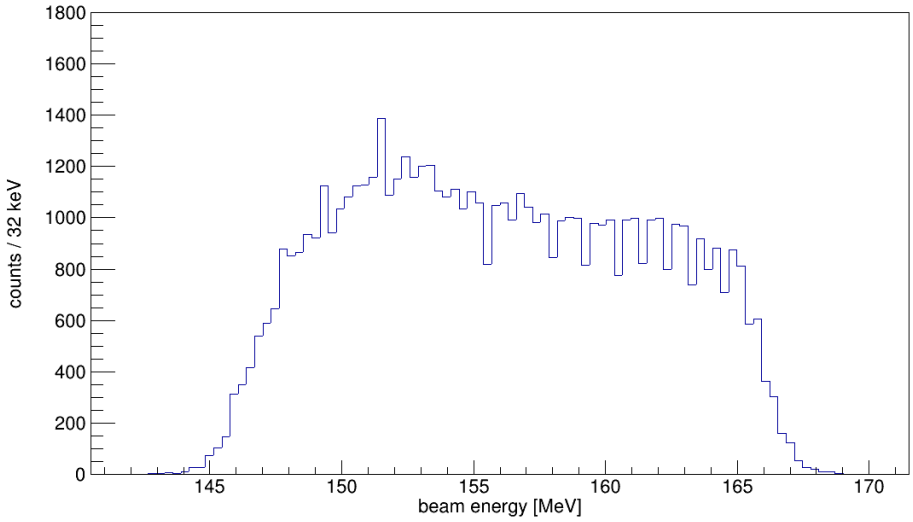

Figure 3.6: Kinetic energy spectrum of the ^{6}He beam

Two time-of-flight measurements were then taken, with the F3 subdetector positioned first in the beam path in one measurement and the F5 subdetector positioned first in the beam path in the other measurement. The obtained flight times corresponded to the sum of the ToF constant and the time-of-flight between the detectors. The ToF constan,t independent of the beam flight time between the detectors was obtained by calculating the average value of the two measurements. With the ToF of the particle and its energy loss in the plastic scintillator, it is possible to produce a Particle Identification Plot (PID) and identify the ion. The PID with data from the first geometry after precleaning is presented in Figure 3.10 in section 3.3.

The kinetic energy of the beam particles impinging on the target was calculated based on the time-of-flight using the formula

$$T = (\gamma - 1)m_0c^2 \tag{3.2}$$

where T is the kinetic energy in MeV, $\gamma = \frac{1}{\sqrt{1-\beta}}$ is the Lorentz factor with β the ratio of the particle velocity to the speed of light, m_0 is the particle rest mass in MeV/c^2 and c is the speed of light. After the calculation, the energy was corrected for loss in the plastic scintillator in the ToF subdetector in F5 and the two MWPCs.

The beam energy obtained for ^{6}He is presented in Figure 3.6.

3.2.4 MWPC alignment

The multi-wire proportional chambers can detect the location (vertex) of beam ion interactions within their volume. If the beam position is measured in two detectors, this information can be used to reconstruct the direction of the incoming beam vector, which is necessary for a complete reconstruction of the reaction geometry.

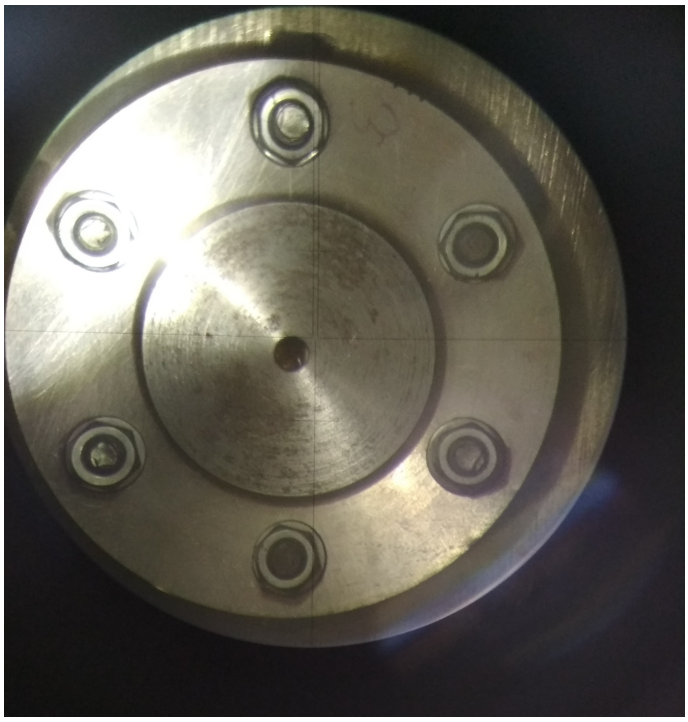

Figure 3.7: MWPC with a diaphragm mounted for the geometrical correction measurement.

The Cartesian coordinates of a particle vertex within each MWPC are easily obtainable from the formulae

$$X\ [mm] = ID_X * D_{wire} - X_0 + \Delta X_{1,2} \tag{3.3}$$

$$Y\ [mm] = -ID_Y * D_{wire} + Y_0 + \Delta Y_{1,2} \tag{3.4}$$

$$Z\ [mm] = \begin{cases} -816.0 & \text{for MWPC 1} \\ -270.0 & \text{for MWPC 2} \end{cases} \tag{3.5}$$

where $ID_{X,Y}$ is the number of the wire within the grid which registered the signal,

$D_{wire} = 1.25\ [mm]$ the distance between the wires, and X_0, Y_0 the position of the wire with $ID_{X,Y} = 0$. $\Delta X_{1,2}$ and $\Delta Y_{1,2}$ are corrections to the grid position in the laboratory system of coordinates.

Ideally, the MWPCs should be placed so that their geometrical center lies on the Z axis in the laboratory system, but two corrections need to be made:

- correction for the MWPC entrance/exit window position relative to the Z-axis

The distance between the center of the exit window of the MWPC and the Z-axis in the laboratory coordinate system was estimated with the use of a theodolite. First, a thick aluminum diaphragm with a hole in the center was placed in the MWPC exit window, and the distance from the center of the diaphragm to the beam axis was measured. This measurement was performed for both MWPCs, and a photograph of the view from the theodolite is presented in Figure 3.7.

- correction for the MWPC grid position relative to the MWPC entrance/exit window

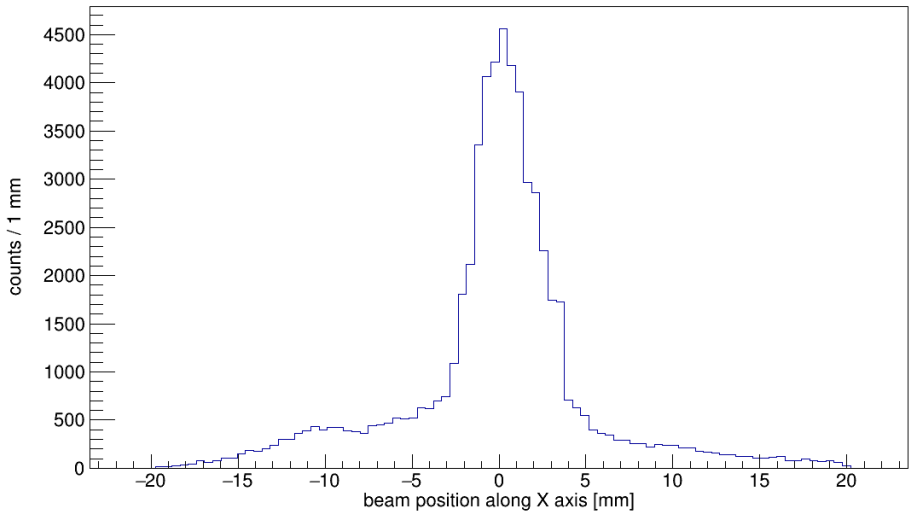

Figure 3.8: Beam distribution along the X axis in MWPC 1 after passing through the diaphragm.

In order to measure the second correction to the MWPC position, a diaphragm was placed in the entrance window of MWPC 1, and a short measurement of the beam which passed through the diaphragm was made. A Gaussian function was fitted to the measurement data to determine the center of the distribution. The

values obtained for the X and Y axes indicate the displacement of the grid relative to the diaphragm and, therefore, to the center of the entrance/exit window. The measurement was performed for both MWPCs. Figure 3.8 presents the distribution of the beam passing through the diaphragm.

A summary of the obtained corrections is presented in Table 3.2.

Once the vertices are calculated and the corrections applied, the beam vector can be calculated with the formula

$$\mathbf{V}_{beam}(X,Y,Z) = \mathbf{V}_{MWPC2}(X,Y,Z) - \mathbf{V}_{MWPC1}(X,Y,Z) \tag{3.6}$$

where $V_{MWPC1,2}(X,Y,Z)$ are the vertices of the particle interaction in each MWPC in the laboratory system of coordinates.

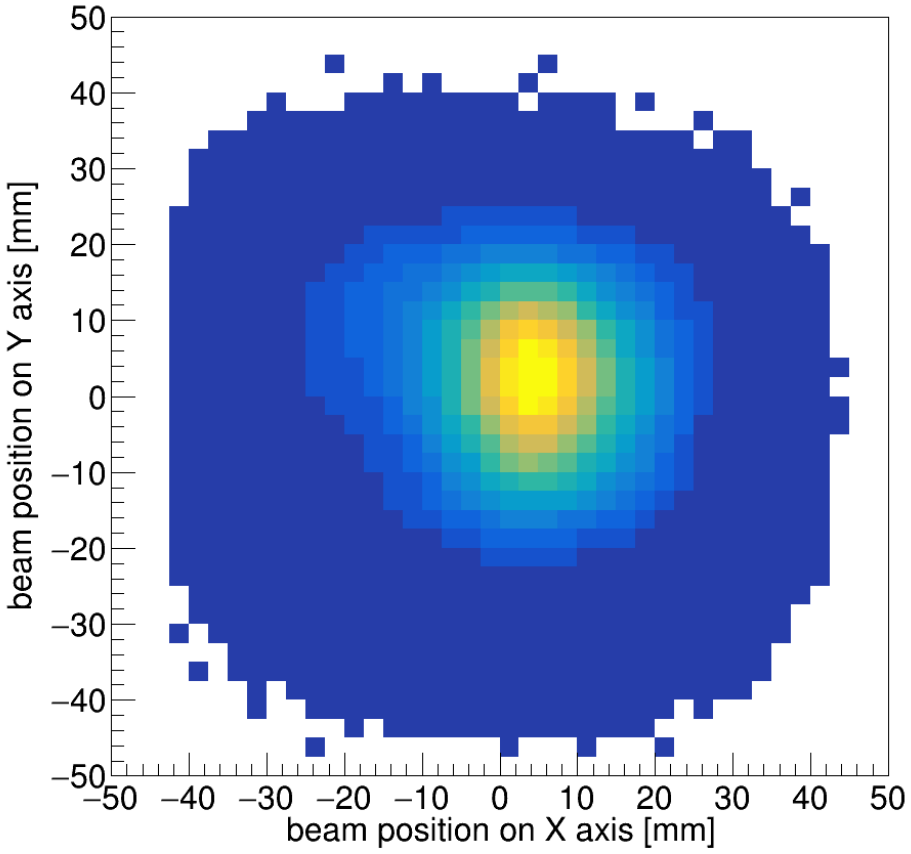

Figure 3.9: Beam profile on the target plane obtained in the first geometry.

The beam vertex at the target plane is the intersection point of a line (in this case the beam vector) and a plane (in this case the target plane). By drawing a 2D histogram with the calculated beam positions on the target plane, we can obtain the beam profile. The profile obtained for the first geometry is shown in Figure 3.9. For this geometry, FWHM of 22.8 mm was obtained on the X axis and FWHM of 19.7 mm on the Y axis.

ID	window-axis [mm]	window-grid [mm]	sum [mm]
MWPC 1 X	-1.0	0.0	-1.0
MWPC 2 X	-1.2	1.0	0.2
MWPC 1 Y	-3.5	1.362	-2.137
MWPC 2 Y	-1.7	0.575	-1.125

Table 3.2: Summary of MWPC positioning corrections. The column **window-axis** presents the corrections for the distance between the center of the detector exit window and the Z-axis, the column **window-grid** presents the corrections for the distance between entrance window and the wire grid, and the column **sum** presents the sum of these corrections.

3.3 Data reduction

In order to calculate differential cross section correctly, it is necessary to identify the reaction of interest and extract it from the many reactions recorded during the experiment. This section describes the process of identifying the ^{6}He(p,p)^{6}He and ^{6}He(d,d)^{6}He elastic scattering, as well as the ^{6}He(d,t)^{5}He transfer reaction. At this point in the data analysis, the detectors were calibrated and the reaction vertex at the target was reconstructed. Reaction products registered in the telescopes had their vertices, direction vectors, and laboratory angles reconstructed with respect to the beam vector. Since both elastic scattering and transfer reaction assume ^{6}He ion interaction within the target volume, some data cuts can be introduced for both reactions:

- ^{6}He in the beam

The ^{6}He nucleus is a relatively long-lived nucleus with a lifetime of about 0.8 seconds, while the time frame of the experiment is in the hundreds of nanoseconds. This allows the assumption that the particle identified using data from the ToF detector as ^{6}He is stable throughout the experiment concerning spontaneous decay. As the

particle travels from the F5 focal plane to the target, it maintains its original state without decay. The above assumption also applies to the ^{6}He elastically scattered off the target traveling toward the right telescope. Helium-6 in the beam can be identified based on the ID plot presented in Figure 3.10. This is a plot of the relationship between the particle time of flight in the ToF detector and the light response of the ToF subdetector in the F5 focal plane. For light exotic nuclei, the identification of ions is simplified due to the significant differences in mass between hydrogen isotopes and the absence of ^{5}He and ^{7}He.

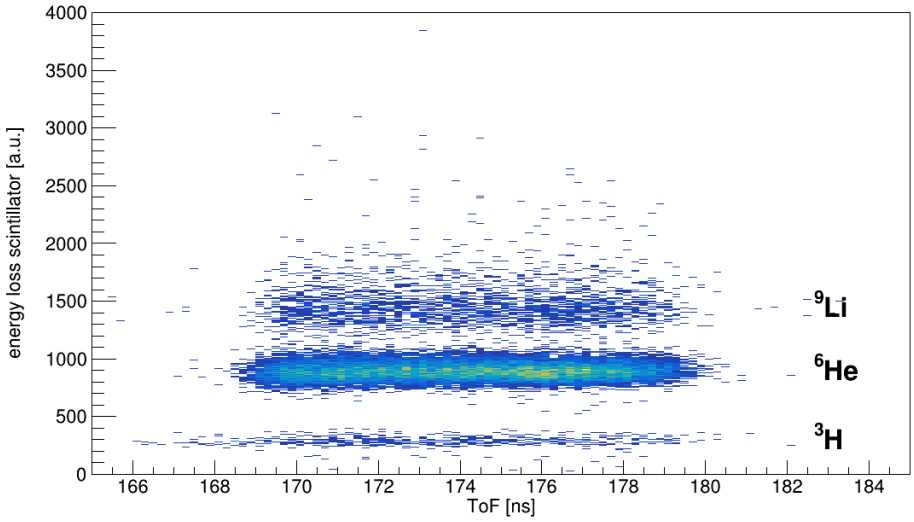

Figure 3.10: Time-of-flight of the particle plotted against its energy loss in the scintillator of the ToF subdetector. The loci corresponding to ^{9}Li, ^{6}He and ^{3}H are denoted.

- Beam impinging on the target

The target was mounted using 2 mm thick aluminum holding frames, which is a source of unwanted reactions. In order to get rid of the noise generated by the frames, a graphical cut was made on the beam vertex in the target plane. The background for both elastic and neutron transfer channels is negligible and is included in the statistical uncertainty estimation due to the multidimensional filtering process.

3.3.1 Elastic scattering

The elastic scattering is identified with simultaneous registration of a ^{6}He in the right telescope and a proton or deuteron in the left telescope with a ^{6}He

impinging on the target. The following filters are applied in order to fulfill these requirements:

- Registration of a ^{6}He in the right telescope

It is known that the first excited state of ^{6}He, $E_{2+} = 1.8\ MeV$ is located above the neutron separation energy $S_n = 1.71\ MeV$. The excited ^{6}He nucleus immediately decays into an alpha particle and two neutrons, so a ^{6}He nucleus registered in the right telescope must come from elastic scattering. Theoretically, it is possible to create ^{6}He in a beam reaction with the target, but the chance of this is negligibly small. A ^{6}He in the right telescope can be identified based on the $\Delta E - E$ plot presented in Figure 3.11. Such a plot is created by plotting the energy loss of the particle in the silicon detector against the energy registered in the CsI(Tl) detector.

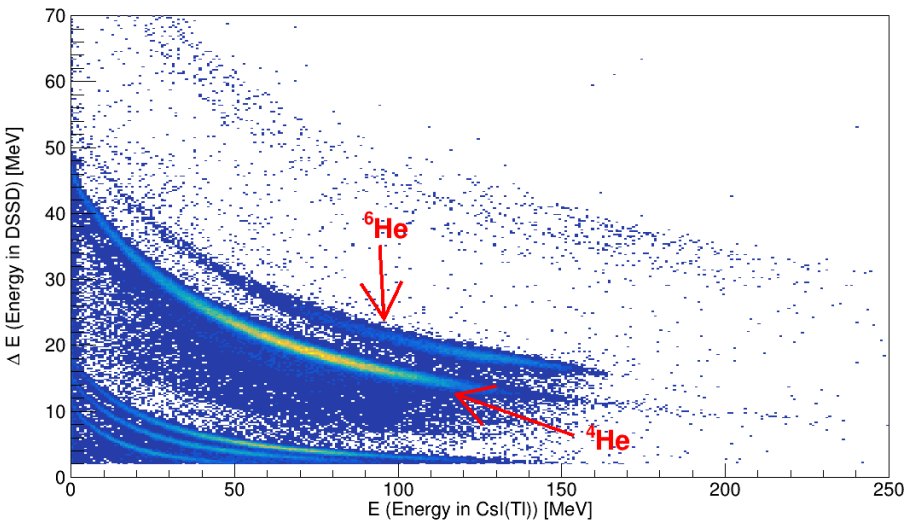

Figure 3.11: Energy loss of a particle in right CsI(Tl) plotted against energy loss in the right DSSD. Loci corresponding to ^{4}He and ^{6}He are labeled.

- Registration of a proton or deuteron in the left telescope

Low-energy protons and deuterons are impossible to identify with the use of a $\Delta E - E$ spectrum in the left telescope because the ions are stopped in the silicon detector. As an alternative, the angle-angle relation of observed nuclei was used to identify and extract reactions of interest. In this method, the laboratory angles of the particles are plotted against each other.

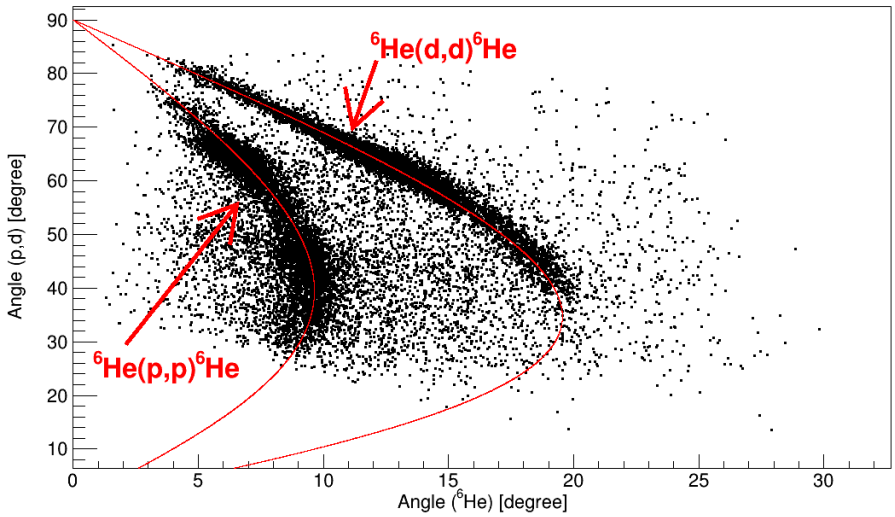

Figure 3.12: Laboratory angle of ^{6}He ions plotted against laboratory angle of ^{1,2}H ions. The kinematic predictions corresponding to the elastic scattering of ^{6}He on ^{1,2}H are plotted.

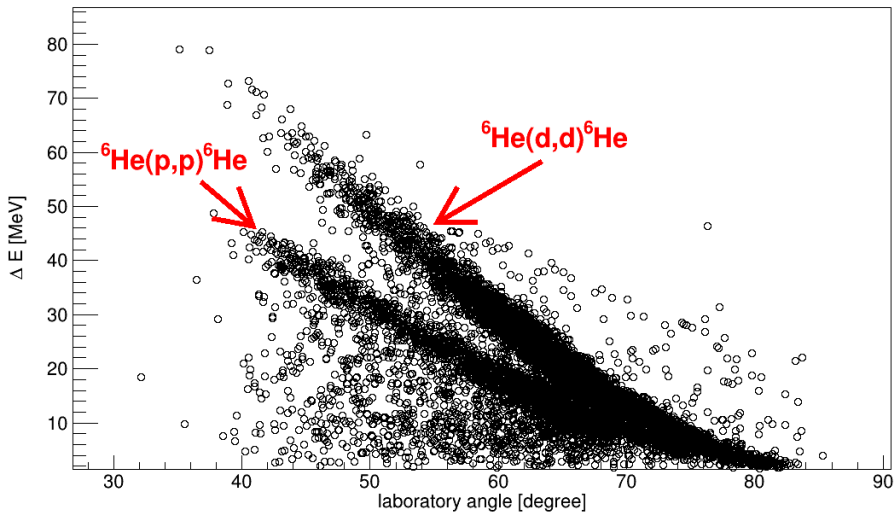

Figure 3.13: Laboratory angle of ^{1,2}H plotted against particle energy loss in the left telescope. The loci corresponding to the elastic scattering of ^{6}He on ^{1,2}H are marked.

The plot is made with pre-cleaned data gated on ^{6}He in the right telescope and in the beam. Figure 3.12 presents an example of such a plot. Loci corresponding to the scattering of protons and deuterons are pronounced and easily identified. Events coming from deuteron breakup might overlap with the angle-angle relation at higher deuteron energies, but these events are filtered out with the angle-energy cut described below.

Another method of extracting elastic scattering from the data is to plot the particle energy as a function of its angle in the left telescope. Figure 3.13 presents an example of such a spectrum. Two loci are visible in the figure, corresponding to the elastic scattering process. The upper locus corresponds to scattered deuterons and the lower one scattered protons.

- Simultaneous registration of a proton or deuteron in coincidence with a ^{6}He

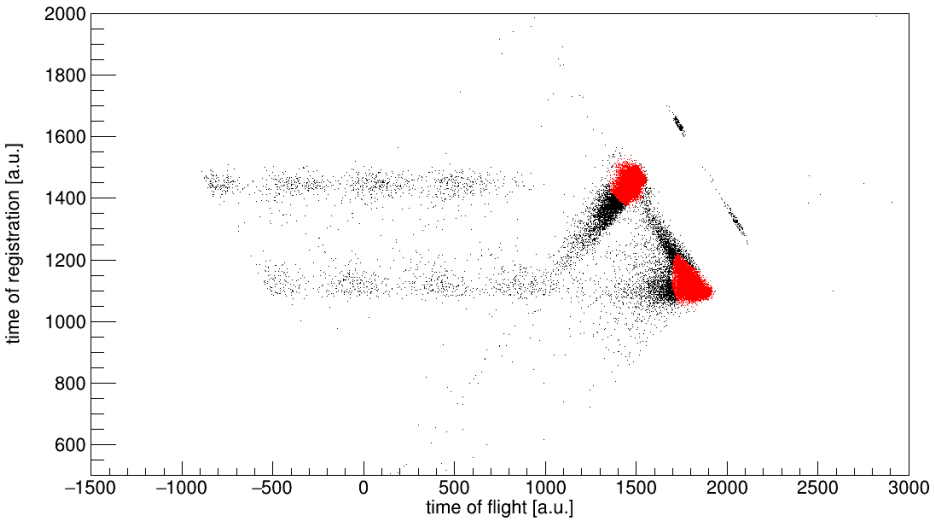

Figure 3.14: Time-of-flight between the ToF F5 subdetector and the left DSSD detector plotted against time stamp in the left DSSD detector. The area where the correct events are located is marked in red.

In order to ensure that the incoming ^{6}He beam ion and elastically scattered nuclei are registered in the same time frame with accuracy down to nanoseconds, a time gate was added. The time of particle registration in the left and separately the right telescopes is plotted against the time of flight between the ToF F5 subdetector and the DSSD detector. An example of a data cut in the left DSSD is presented in Figure 3.14.

3.3.2 Transfer reaction

Identifying and isolating the (d,t) reaction presents a more significant challenge than the elastic scattering. This is due to the lower cross section for this reaction and the immediate decay of the ^{5}He into a ^{4}He and a neutron. The alpha particles produced from ^{5}He also appear in large quantities in the decay of excited

^{6}He, as well as in reactions of the beam with carbon (^{12}C) in the target. This means that the simultaneous registration of ^{4}He+t is no longer an unambiguous way to identify the reaction. Additionally, the decay changes the vector of the alpha particle's flight direction relative to the initial ^{5}He vector. For this reason it was necessary to increase the number of filters applied to the experimental data. A summary of the gates applied to the experimental data:

- Registration of ^{4}He in the right telescope

Immediate decay of ^{5}He$\rightarrow^{4}$He+n requires gating on an alpha particle in the right telescope, which was identified using the $\Delta E - E$ spectrum in the right telescope method described above.

- Registration of ^{3}H in the left telescope

Direct identification of ^{3}H through the $\Delta E - E$ method is impossible for tritium energies below 23 MeV because the particle is entirely stopped in the DSSD. The energy-angle relation of the registered particle does not allow a confident choice of a two-dimensional filter for both the right and left telescopes. Nevertheless, the $\Delta E - E$ spectrum in the left telescope allows the rejection of unwanted data. Loci originating from protons and deuterons were removed, significantly reducing the background.

- Registration of ^{3}H and ^{4}He in coincidence

In order to prevent the registration of particles coming from different beam bunches or decaying nuclei, a time frame gate was applied to the registration time in the left telescope, right telescope, and the time difference between both telescopes.

- Missing mass spectrum of ^{3}H, ^{4}He and neutron

The energy-angle relations of the particles measured with the telescopes did not allow a reliable method of extracting the (d,t) reaction from the data. The beam energy spread, detector resolution, and background impede the removal of unwanted events while retaining events of interest. Missing mass spectra were therefore used to combine energy-angle relations from different detectors and cope with the beam energy spread. In the first step, momentum four-vectors were created for the nucleus

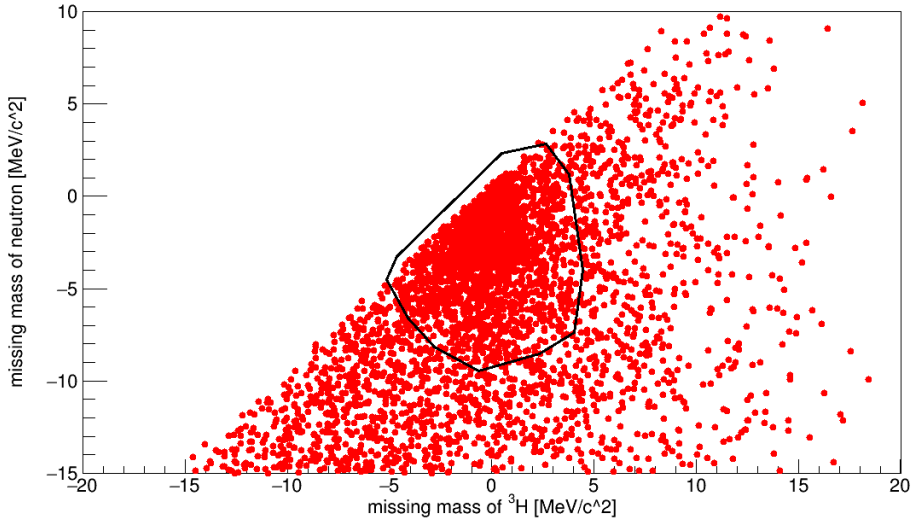

Figure 3.15: Missing mass of the triton plotted against the missing mass of the neutron. The region corresponding to the ^{6}He(d,t)^{5}He reaction is marked with a black line.

of the incoming beam, the nucleus of the target, and the ions registered in both telescopes. These vectors were created using the TLorentzVector class of the ROOT framework, which utilized the total energy and momentum vector of the registered particle. Two separate sets of vectors were created, assuming that a triton was registered in the left telescope and an alpha particle was registered in the right telescope. Next, momentum four-vectors of neutrons, ^{3}H and ^{4}He were reconstructed according to the formulae:

$$\mathbf{p}'_{neut} = (\mathbf{p}_{beam} + \mathbf{p}_{tar}) - (\mathbf{p}_{4He} + \mathbf{p}_{3H})$$

$$\mathbf{p}'_{3H} = (\mathbf{p}_{beam} + \mathbf{p}_{tar}) - \mathbf{p}_{4He}$$

$$\mathbf{p}'_{4He} = (\mathbf{p}_{beam} + \mathbf{p}_{tar}) - \mathbf{p}_{3H}$$

where $\mathbf{p}_{beam}$, $\mathbf{p}_{tar}$, $\mathbf{p}_{4He}$ and $\mathbf{p}_{3H}$ are the experimental momentum four-vectors of the beam, target, triton, and ^{4}He accordingly. For each reconstructed vector the missing mass was calculated by subtracting the particle rest mass from its total energy. The missing mass spectrum of the neutron was plotted against the missing mass spectrum of the ^{3}H and ^{4}He. The resulting graphs are presented in Figure 3.15 and 3.16

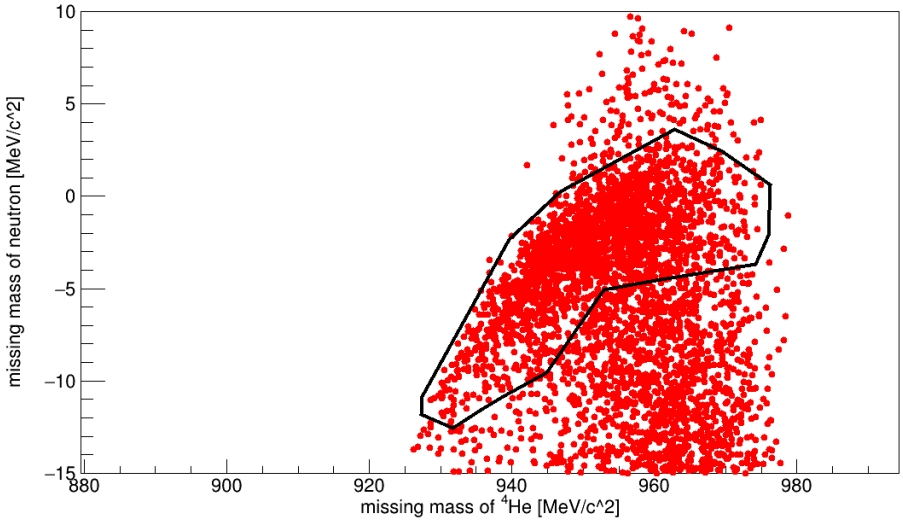

Figure 3.16: Missing mass of the alpha particle plotted against the missing mass of the neutron. The region corresponding to the ^{6}He(d,t)^{5}He reaction is marked with a black line.

The centers of the loci for the neutron, ^{3}H and ^{4}He are expected to be at 0, 0, and 939.565 MeV, respectively. The shifts between the observed and expected centers of the loci are caused by the linear calibration of the CsI detectors. However, the difference does not prevent the identification of the reaction. The cuts used were made with a surplus to avoid losing events, with the additional false-positive events chosen in one filter being removed by the other filter.

3.4 Detection efficiency

The detection efficiency of the experimental setup is defined as the probability of detecting and identifying a given reaction angle θ in the center-of-mass system. It is a function of many independently contributing factors, such as the beam distribution on the target, the scattering angle in the center-of-mass system, and the geometry of the experimental setup. The registration efficiency varies by several orders of magnitude in the region of angles corresponding to the edges of the telescopes. It significantly impacts the shape of the differential cross section in these regions.

The registration efficiency was calculated using of a Monte Carlo simulation for each geometry and reaction. The simulation was written in the Geant4 frame-

work [24, 25, 26] version 10.7.4, in the C++ programming language. The Geant4 framework allows for a simulation of particle interactions with matter and its tracking. The simulation can provide data such as the reaction vertex and the energy deposited by the particle in a given geometry element. The source code of the simulation has been posted on the GitHub website at https://github.com/guar1337/geant4 and on the Heavy Ion Laboratory website at the University of Warsaw. In the following section, the most critical parts of the simulation will be described without going into detail about how they were programmed. In the simulation, the experi-

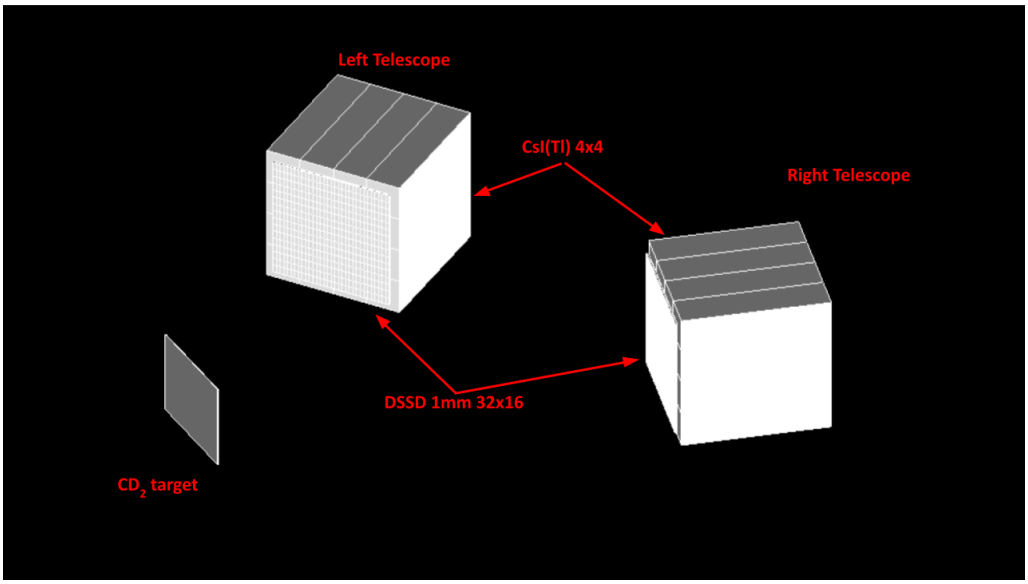

Figure 3.17: Screenshot from the Monte Carlo Simulation with the target and the detectors labeled.

mental setup consisting of two telescopes was reconstructed, maintaining the angles at which the detectors were positioned and their sizes. The experimental setup was constructed in three versions, one for each geometry. The versions differed in the angles at which the left telescope and the target were positioned, as well as the spatial distribution of the beam. A screenshot showing the graphical representation of the detectors in the simulation is presented in Figure 3.17.

The MWPC detector was indirectly simulated using experimental data from the MWPC subdetectors. The events recorded with the "beam trigger" allowed the reconstruction of the beam profile on the target and its directional vector in a given geometry. Then, the data were uploaded into the simulation and for each event a unique beam vector passing through the target was constructed. In the next step,

reaction vertices were randomly generated along the beam vector inside the target volume. At the obtained vertices, momenta four-vectors of particles (p and ^{6}He), (d and ^{6}He), or (t and ^{5}He) in the center-of-mass frame of reference were generated with opposite direction vectors and then converted to the laboratory frame of reference. Theta and phi angles were randomly chosen independently for each event. At this

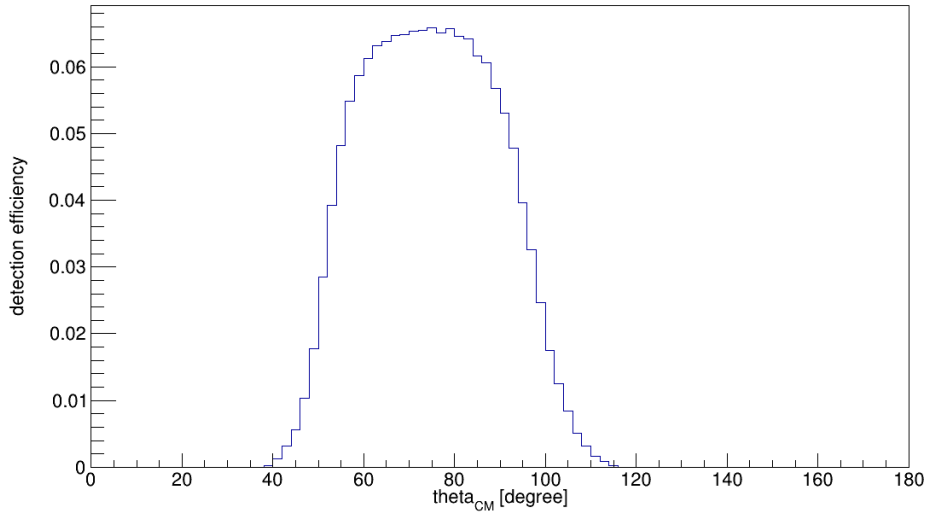

Figure 3.18: Detection efficiency for the ^{6}He(d,d)^{6}He elastic scattering in the second geometry calculated using Monte Carlo simulation in the Geant4 [24, 25, 26] framework. The detection efficiency was calculated by considering the beam spread on the target plane and its direction vector.

stage of the simulation, Geant4 began tracking the particles. The program saved the information on the particle vertices, IDs of the strips hit and the energy deposited in the detectors. Collected information was structured similarly to the experimental data and saved to the .root file. The obtained files were analysed taking into account the cuts applied to the beam position on the target plane. The registration efficiency in the center-of-mass system was calculated for each angle θ bin using the formula

$$\eta(\Delta\theta) = \frac{N_{obs}(\Delta\theta)}{N_{sim}(\Delta\theta)} \tag{3.7}$$

where $N_{obs}(\Delta\theta)$ and $N_{sim}(\Delta\theta)$ are the number of events registered and the number of events simulated over a given CM angle range. The detection efficiency obtained for the (d,d) reaction in the second geometry is presented in Figure 3.18.

3.5 Cross section calculation

The differential cross section for both elastic and neutron transfer reactions was calculated using the formula

$$\frac{d\sigma}{d\Omega}(\Delta\theta) = \frac{N_{exp}(\Delta\theta)}{\Delta\Omega(\Delta\theta) * N_{tar} * N_{beam} * \eta(\Delta\theta)} \tag{3.8}$$

where $\Delta\Omega(\Delta\theta)$ is the solid angle for a given bin of CM angle, $N_{exp}(\Delta\theta)$ is the number of identified reaction events for a given bin of CM angle, N_{tar} is the target thickness in $\frac{atoms}{cm^2}$, N_{beam} is the beam flux and $\eta(\Delta\theta)$ is the detection efficiency for a given bin of CM angle. Calculation of the target thickness is described thoroughly in Appendix A. We used experimental data acquired with the beam trigger after implementing a pre-cleaning procedure to estimate the beam flux to ensure beam quality. To estimate the detection efficiency, Monte Carlo simulations were performed for each process in every geometry.

3.5.1 Determination of the elastic scattering cross section

After the elastic channel was identified, the laboratory angle of ^{1,2}H registration was transformed to the CM according to equation (49) taken from [27]

$$\theta_{CM} = acos\left(\frac{1 - \gamma^2 \tan^2\theta_{lab}}{1 + \gamma^2 \tan^2\theta_{lab}}\right) \tag{3.9}$$

where γ is the Lorentz factor of the center-of-mass system velocity in the laboratory frame and θ_{lab} is the angle of ^{1,2}H registration. Once the angles were converted, the data were divided into bins with an angular step of 2°, and counts were integrated over each bin. The differential cross section was calculated separately for each geometry and overlapping data points were removed.

The angular distributions of the data are presented in Figures 3.19 and 3.20. The error bars represent statistical uncertainties only. For the majority of the data points, the error bars are included within the data point. Tabulated data points are given in Appendix B. The elastic scattering of ^{6}He on protons was compared with the data obtained for the same reaction by Wolski et al. [1] measured at a similar energy for the validation of the target thickness calculations. Considering

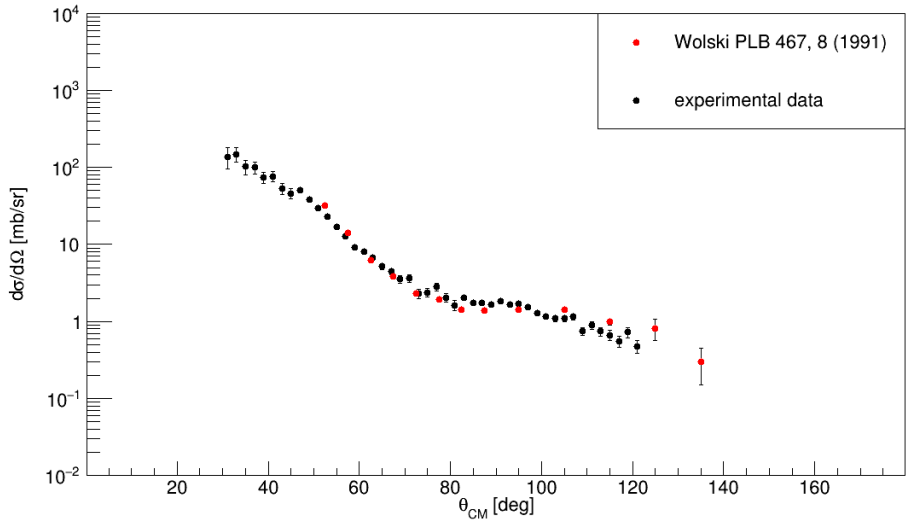

Figure 3.19: Differential cross section data for the ^{6}He(p,p)^{6}He elastic scattering obtained in this experiment and by Wolski [1]. The error bars denote statistical errors only.

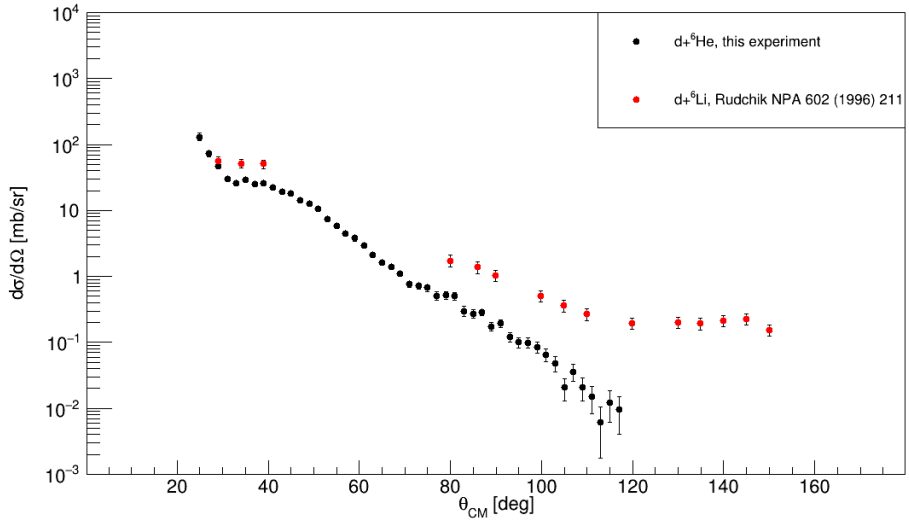

Figure 3.20: Differential cross section for the ^{6}He(d,d)^{6}He elastic scattering (this work) and for ^{6}Li(d,d)^{6}Li scattering (Ref. [28]). The error bars denote the statistical errors only.

the systematic uncertainty of 30% reported in [1], the obtained data validate the target thickness estimation method.

The elastic scattering of ^{6}He on deuterons is plotted together with the angular distribution for the d+^{6}Li scattering at 25 MeV/n from Rudchik et al. [28]. The significant difference between the angular distributions can be attributed to the

difference in the structure of ^{6}He and^{6}Li.

3.5.2 Determination of the neutron transfer cross section

The transfer reaction was not observed in the first geometry due to the positioning of the left telescope, and only small statistics were collected in the third geometry due to the detector positioning and the angle-angle relation of scattered particles. Therefore, the neutron transfer reaction differential cross section was

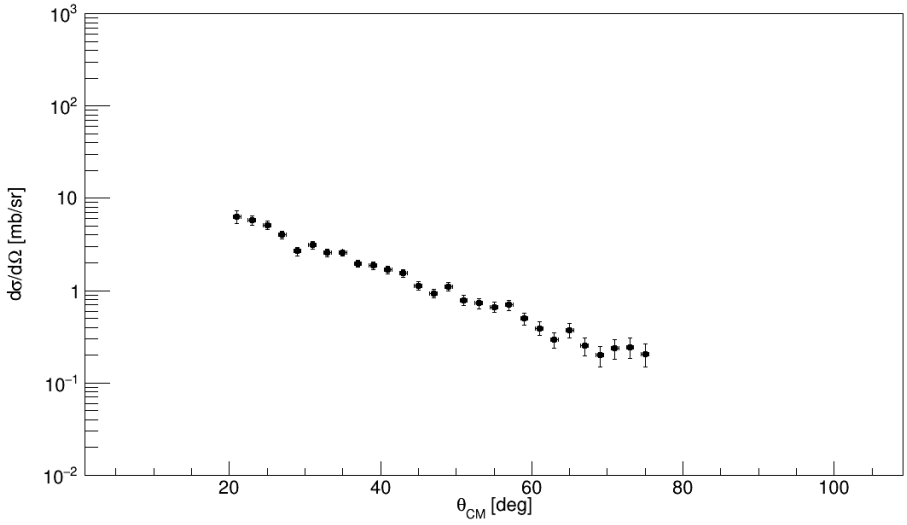

Figure 3.21: Differential cross-section data for the ^{6}He(d,t)^{5}He reaction. The error bars depict the statistical error.

calculated using the experimental data collected in the second geometry. The laboratory angle of the registered ^{4}He was transformed to the CM according to the equation (47) taken from [27]

$$\theta_{CM} = \arccos\left(\frac{-x\gamma^2\tan^2\theta_{lab} + \sqrt{1+\gamma^2\tan^2\theta_{lab}\,(1-x^2)}}{1+\gamma^2\tan^2\theta_{lab}}\right) \text{ with } x = \frac{\beta}{\beta_{CM}} \quad (3.10)$$

where β is the ratio of the center-of-mass velocity to the speed of light speed, β_{CM} is the ratio of the velocity of the ^{4}He in the center-of-mass to the seed of light, γ is the Lorentz factor of the center-of-mass system velocity in the laboratory system, and θ is the angle of the registered ^{4}He in the laboratory system. Tabulated data points are given in Appendix B.

3.5.3 Experimental error estimation

The statistical error $S_{stat}(\Delta\theta)$ related to the differential cross section measurement was estimated for each $\Delta\theta_{CM}$ bin using the following formula

$$S_{stat}(\Delta\theta) = \pm\frac{d\sigma}{d\Omega}(\Delta\theta)\sqrt{\frac{N_{exp}(\Delta\theta)}{N_{exp}(\Delta\theta)^2}} \tag{3.11}$$

where $N_{exp}(\Delta\theta)$ is the number of registered events for a given CM angle bin. The errors obtained for the differential cross sections measured in each bin in every reaction are presented in Appendix B.

The average statistical errors for elastic scattering are 12.0% and 16.8% for scattering off protons and deuterons, respectively. The average statistical error obtained for the neutron transfer reaction is 14.1 %.

The systematic error was calculated according to the formula

$$S_{sys} = \sqrt{\left(\frac{S_{\Delta\Omega}}{\Delta\Omega}\right)^2 + \left(\frac{S_{N_{tar}}}{N_{tar}}\right)^2 + \left(\frac{S_{N_{beam}}}{N_{beam}}\right)^2 + \left(\frac{S_{\eta}}{\eta}\right)^2} \tag{3.12}$$

where $\frac{S_{\Delta\Omega}}{\Delta\Omega}$ is the relative uncertainty of the solid angle $\Delta\Omega$, $\frac{S_{N_{tar}}}{N_{tar}}$ is the relative uncertainty of the target thickness N_{tar}, $\frac{S_{N_{beam}}}{N_{beam}}$ is the relative uncertainty of the beam flux N_{beam} and $\frac{S_{\eta}}{\eta}$ is the relative uncertainty of the detection efficiency η.

The relative uncertainty of the solid angle $\frac{S_{\Delta\Omega}}{\Delta\Omega}$ was estimated at 4.8% for the elastic scattering of ^{6}He from protons and at 2.5% for scattering from deuterons. For the transfer reaction, it was estimated at 10%. The detecton efficiency $\frac{S_{\eta}}{\eta}$ uncertainty was estimated at 5% for both scattering reaction and at 10% for the neutron transfer reactions. The target thickness uncertainty $\frac{S_{N_{tar}}}{N_{tar}}$ was averaged over the uncertainties obtained for each geometry, giving 7.2% for scattering from protons and 6.2% for scattering from deuterons. The deuteron target thickness uncertainty obtained for the second geometry was used for the transfer reaction - 5.1%. The beam flux uncertainty $\frac{S_{N_{beam}}}{N_{beam}}$ was estimated at 10% for each reaction.

The resulting systematic uncertainties are 14.1% for the p+^{6}He scattering, 13.0% for the d+^{6}He scattering and 18.1% for the transfer reaction.

Chapter 4

Theoretical analysis

The theoretical analysis of the obtained angular distributions for the elastic scattering and neutron transfer reaction will be described in this chapter. Elastic scattering of ^{6}He was analyzed within the framework of the optical model. This will be described accordingly in section 4.1 for the scattering of ^{6}He from protons and section 4.2 for the scattering of ^{6}He from deuterons. The neutron transfer reaction was analyzed using the distorted-wave Born approximation. All calculations were performed using the FRESCO [29] program version 3.4 , and the fitting procedures were performed with the SFRESCO [29] program version 3.4.

4.1 Elastic scattering, ^{6}He(p,p)^{6}He

The experimental differential cross section for the scattering of ^{6}He from protons was compared with cross sections calculated using selected published optical potentials.

The first potential was a global optical potential for the nucleon-nucleus interaction proposed by Varner et al. [2]. The second was obtained by Wolski et al. [1] for the same reaction at a similar energy (25 MeV/n). Wolski adjusted the volume real and surface imaginary terms of the global optical potential by Varner [2] to fit the experimental data. The third optical potential was obtained by Rusek et al. [3] from a microscopic analysis of p+^{6}He elastic scattering data [1] with CDCC

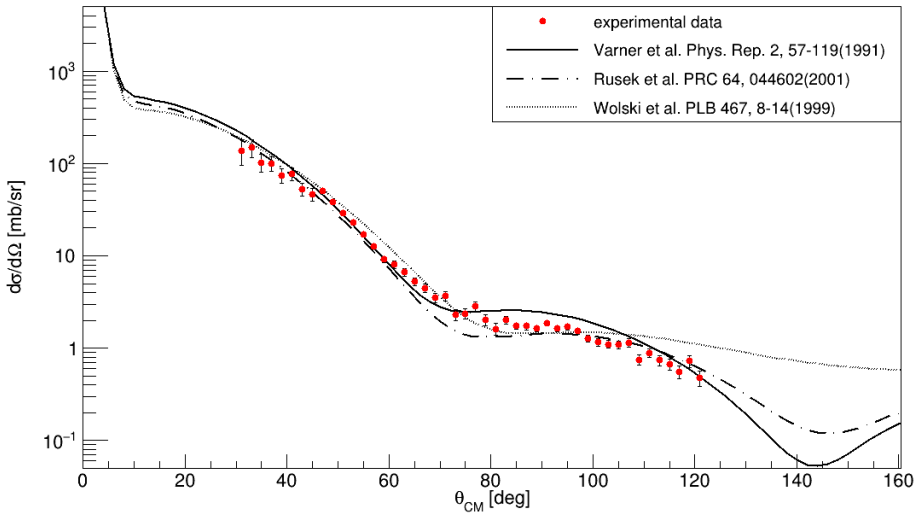

Figure 4.1: Experimental and calculated differential cross sections for the p+^{6}He elastic scattering. The cross sections were calculated within the OM and are based on OPs from Rusek [3], Wolski [1] and Varner [2].

calculations. This potential was read in by FRESCO in numerical form, both real and imaginary terms of the central potential and a spin-orbit term.

The calculated cross sections describe the experimental data after considering systematic errors, as seen in Figure 4.1. The OM potential of Wolski agrees well with the present data up to 100 degrees in the CM, where it starts to overestimate the cross section. The OMP obtained by Rusek underestimates the data in the range from 60 to 80 degrees in the CM, and the OMP by Varner overestimates the data in the range from 80 to 110 degrees in the CM.

Better to describe the experimental data, the parameters of the above-mentioned optical potentials were adjusted to minimize χ^2/N. The procedure was performed using the SFRESCO program separately for each potential. The spin-orbit terms were excluded from the search to reduce the number of free parameters. In the case of the Varner and the Wolski potentials, this resulted in a potential form:

$$U(r) = V_{vol}(r) + W_{vol}(r) + W_{surf}(r) \tag{4.1}$$

The potential depth, radius, and diffuseness parameters were fit for each term. In the case of the CDCC potential, both real and imaginary potentials were scaled by

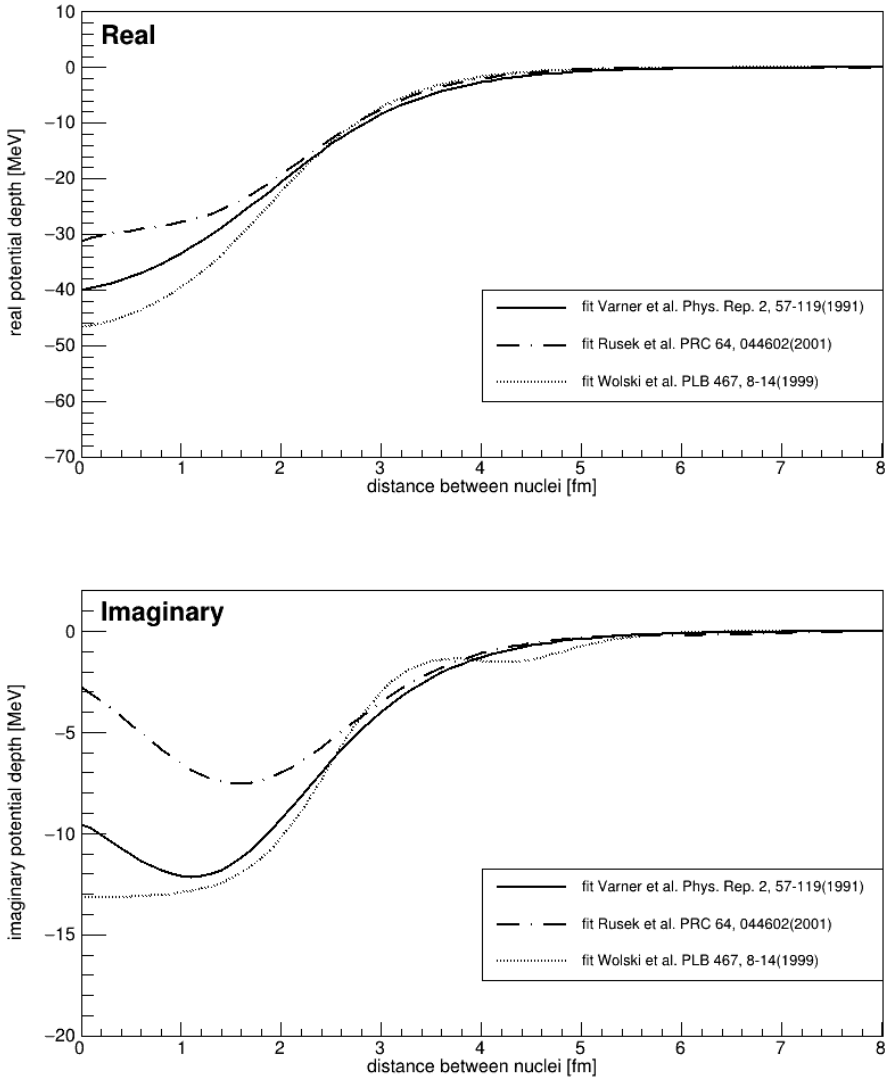

Figure 4.2: A comparison of the real and imaginary parts of the optical potentials for the p+^{6}He scattering used in the OM calculations plotted in Fig. 4.3

a normalization factor. The obtained potentials are presented in Figure 4.2. The real and imaginary depths of the CDCC potential were scaled by factors of 0.977 and 0.758, respectively. Figure 4.3 presents the cross sections calculated using the fitted potentials.

After the fitting procedure, all three potentials describe the experimental data over the whole angular range, with a small discrepancy at around 75° in the CM in the case of the fitted CDCC potential. It is worth noting that above 120° in the CM, the calculated cross sections diverge, and additional measurements in the region above the 120° in the CM are required to determine whether the fits based

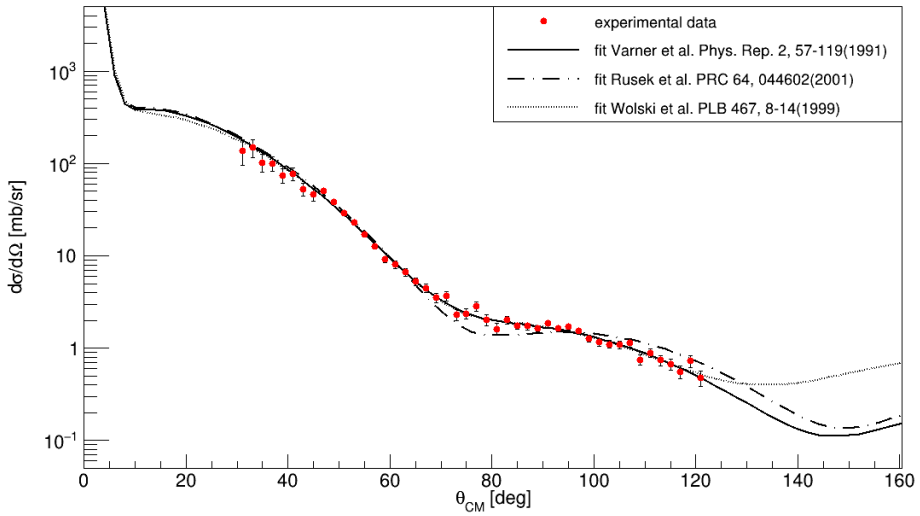

Figure 4.3: Experimental data and OM calculations of differential cross sections for the p+^{6}He elastic scattering. The OM calculations are based on the optical potentials by Rusek [3], Wolski [1], and Varner [2] fit to the experimental data.

potential	Term	V_0 [MeV]	r_0 [fm]	a_0 [fm]	$W_{0,s}$ [MeV]	$r_{w,s}$ [fm]	$a_{w,s}$ [fm]
Wolski	volume	45.4	1.80	0.61	2.58	2.00	0.69
	surface	-	-	-	3.47	3.2	0.77
	spin-orbit	5.9	1.235	0.63	-	-	-
Wolski fit	volume	49.14	1.883	0.627	13.20	2.478	0.394
	surface	-	-	-	1.376	4.313	0.397
Varner	volume	49.93	2.02	0.69	2.58	2.0	0.69
	surface	-	-	-	9.32	2.0	0.69
	spin-orbit	5.9	1.235	0.63	-	-	-
Varner fit	volume	43.28	1.920	0.757	5.727	0.202	0.712
	surface	-	-	-	10.99	1.258	0.782

Table 4.1: Original and fit optical potential parameters for the elastic scattering of ^{6}He off protons. In the fitting procedure, all of the optical potential parameters were varied. Spin-orbit terms were omitted in the fitting procedure.

on the Wolski OP or those on the Varner or Rusek potentials describe the data better. A summary of the original and fitted parameters for the Varner and Wolski potentials is presented in Table 4.1. The GOP of Varner fitted to the experimental data will be referred to as **"fGOP"** and the OMP obtained by Rusek from CDCC calculations fitted to the experimental data will be referred to as **"fCDCC"**.

A good agreement between the model and the experimental data was obtained for the fits based on the Varner and Wolski potentials, and only slightly worse but still good agreement was achieved based on the Rusek potential. A comparison of the weighted chi-squares of the fit potentials is presented in Table 4.2.

The obtained χ^2/N values for the original OM potentials are comparable, with the **fGOP** fitting the experimental data better than the **fCDCC** potential and the OM potential of Wolski [1]. Potentials obtained from fitting OM potentials based on these of Varner and Wolski with 9 parameters describe the experimental data significantly better than the **fCDCC** potential, where only two parameters were fit.

χ^2/N	**Original**	**Fit**
Rusek [3]	9.297	4.102
Wolski [1]	11.27	1.010
Varner [2]	6.925	1.075

Table 4.2: Comparison of χ^2/N obtained for different optical potentials and their fits to the experimental data for p+^{6}He elastic scattering.

4.2 Elastic scattering, ^{6}He(d,d)^{6}He

The measured differential cross section for the scattering of ^{6}He from deuterons was compared with cross sections obtained from OM calculations with global deuteron potentials and from single-folded p+^{6}He potentials derived in the previous section. For this method, the fitted CDCC potential of Rusek et al. [3] (**fCDCC**) and the fitted global optical potential of Varner et al. [2] (**fGOP**) were chosen.

4.2.1 Optical potential parametrization

There are multiple [30, 31, 32, 33, 4] global optical potentials available for the elastic scattering of deuterons. Most of these parametrizations were obtained for heavier nuclei: Perey and Perey [30] used data starting at Z≥12, Daehnick [31] starting at A≥27, Bojowald [32] starting at ^{27}Al and An [33] starting at ^{12}C. The parametrization proposed by Zhang [4] in 2016 included targets as light as A≥9 and lower deuteron energies. In his work, Zhang obtained [4] results significantly better than Daehnick and An. A comparison of cross sections for d+^{6}He scattering obtained from the Daehnick, An, and Zhang parametrizations is presented in Figure 4.4. The differential cross section obtained from Zhang's optical potential parametrization provides the most accurate description of the experimental data. It

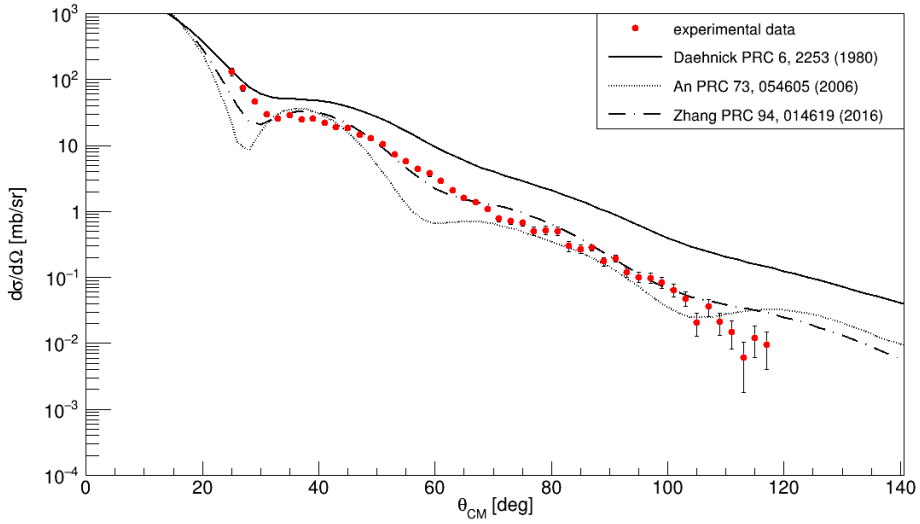

Figure 4.4: Experimental data and OM calculations of differential cross sections for the d+^{6}He elastic scattering. The cross section calculations are based on the optical model parameterizations by Daehnick [31], An [33] and Zhang [4].

is worth noting that the potential does not contain a spin-orbit term, and the surface term is negligibly small. This potential was chosen for a fit procedure. The lack of a spin-orbit term allows for easier parameter fitting. The global optical potential proposed by Zhang [4] consists of volume real and imaginary terms and a surface imaginary term. The OP parameters were varied to generate the optical potential that best matched the experimental data. This fitted potential will be referred to as **"fitted d+^{6}He GOP"**. A comparison of the original and fitted parameters of Zhang's optical potential is presented in Table 4.3 and the comparison with the experimental data is shown in Figure 4.4 and Figure 4.7, respectively.

term	**V_0 [MeV]**	**r_0 [fm]**	**a_0 [fm]**	**$W_{0,s}$ [MeV]**	**$r_{w,s}$ [fm]**	**$a_{w,s}$ [fm]**
volume	84.8	1.9	0.776	11.45	3.887	0.744
surface	-	-	-	0.002	3.887	0.744
volume, fitted	61.63	2.006	0.812	21.85	2.033	1.024
surface, fitted	-	-	-	0.708	2.989	0.362

Table 4.3: Global optical potential parameters for the d+^{6}He elastic scattering from the Zhang parametrization [4] together with parameters obtained from fitting the experimental data.

4.2.2 Calculation of the optical potential by means of the single-folding method

The optical potential for d+^{6}He elastic scattering can be obtained through folding U_{p+6He} and U_{n+6He} scattering potentials with the square of the wave function of the $2H_{g.s.}$. Under the assumption that the nuclear parts of the U_{p+6He} and U_{n+6He} are identical, the single-folding equation 1.23 becomes [34]

$$U_{d+6He}(r) = 2 \int |\varphi_{2H}(R)|^2 \; U_{p+6He}(|\mathbf{r} + \frac{1}{2}\mathbf{R}|) d\mathbf{R} \tag{4.2}$$

where $U_{d+6He}(r)$ is the d+^{6}He potential, $|\varphi(R)|^2$ is the square of the wave function of the $^2H_{g.s.}$, $\mathbf{R}$ is the distance between the neutron and the proton, and $U_{p+6He}(|\mathbf{r} + \frac{1}{2}\mathbf{R}|)$ is the single nucleon interaction potential, in our case a p+^{6}He potential (see Figure 1.2). The **fGOP** and **fCDCC** OMPs obtained in the previous section were used as p+^{6}He potential.

The deuteron has the lowest binding energy per nucleon of any naturally occurring isotope with a binding energy $E_d = 2.224 \; MeV$. It is reasonable to assume that the wave function of the ground state of ^{2}H has L = 0 orbital angular momentum. Therefore, its quadrupole moment should also be zero. However, the value of the deuteron quadrupole moment measured in 1947 by Arnold and Roberts [35] was $Q_D = 2.766 * 10^{-27} \; cm^2$, which means that there is a non-zero orbital momentum component. In order to incorporate it, the wave function of the deuteron ground state has to be a mixture of *s-wave* and *d-wave* components according to the formula

$$\varphi_{2H}(R) = S_s * \varphi_s(R) + S_d * \varphi_d(R) \tag{4.3}$$

where S_s and S_d are spectroscopic amplitudes and φ_s and φ_d are wave functions of the *s-* and *d-wave* components, respectively. The amplitudes are varied in order to reproduce the deuteron quadrupole moment. In the present work, the wave function of the deuteron ground state was calculated using three different binding potentials to assess the influence of the deuteron wave function on the resulting optical potentials.

In the first calculation of the single-folding potential, the deuteron was as-

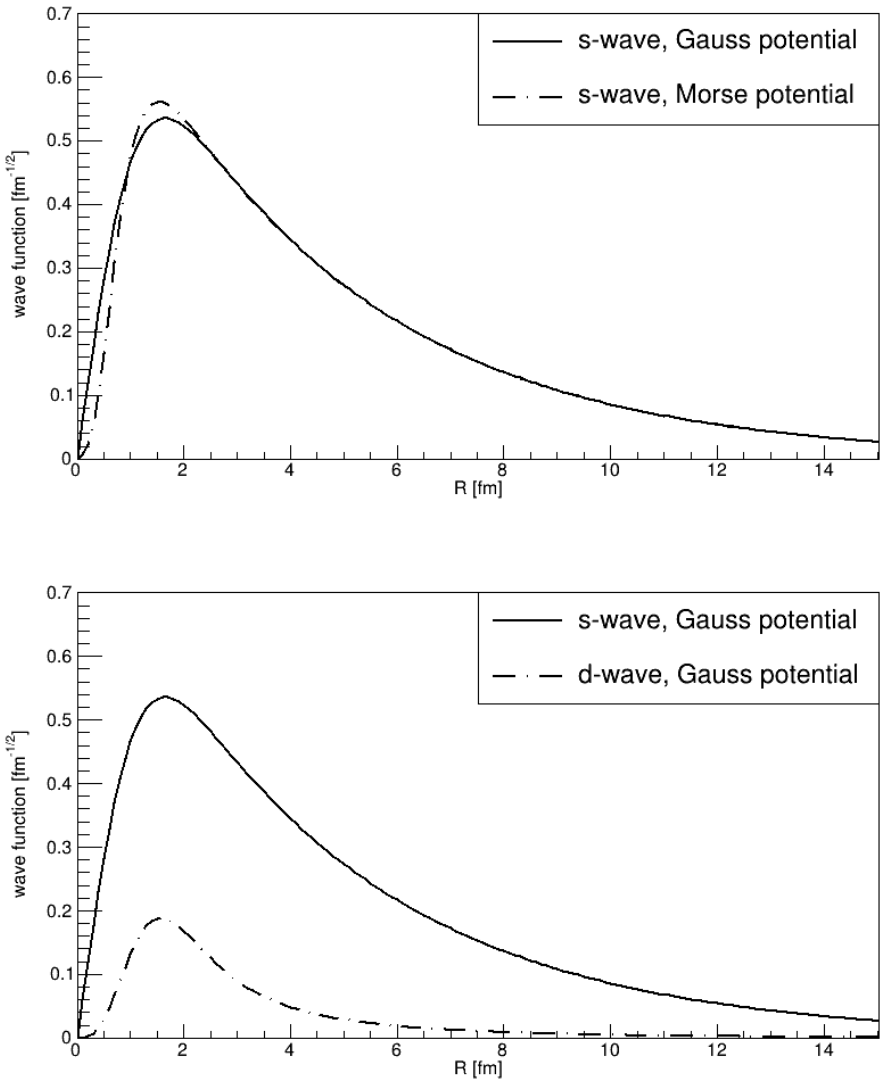

Figure 4.5: Components of the $^2\mathrm{H}_{\mathrm{g.s.}}$ wave function calculated with different binding potential forms and spectroscopic configurations. The upper panel shows pure *s-waves* calculated with the Gauss [36] and Morse [37] forms of the binding potential. The lower panel shows the *s-wave* and *d-wave* components calculated with the Gauss [36] form of the binding potential and the spectroscopic amplitudes from ref. [38].

sumed to have a pure *s-wave* configuration with the binding potential taken from Austern et al. [36] in the form

$$V(R) = -V_0 \; exp\left[-\left(\frac{R}{R_0}\right)^2\right] \tag{4.4}$$

with $R_0 = 1.484$ fm and V_0 varied to reproduce the binding energy of the deuteron $E_d = 2.224$ MeV. The obtained value of V_0 was 72.15 MeV.

In another approach, the deuteron was also considered to have a pure *s-wave* configuration, but the binding potential was in the Morse form [39], as used recently by Khachi et al. [37]

$$V(R) = -V_0 \left(exp\left[\frac{-2(R-r_m)}{a_m}\right] - 2\ exp\left[\frac{-(R-r_m)}{a_m}\right]\right) \tag{4.5}$$

with $V_0 = 114.15\ MeV$, $r_m = 0.841$ fm and $a_m = 0.350$ fm. Since FRESCO does not include the Morse form directly, the binding potential was calculated separately and read in to the program.

In the third procedure, both *s-wave* and *d-wave* components of the deuteron wave function were considered. The *s-wave* binding potential was taken from Austern, the same as in equation 4.4 and the *d-wave* potential was calculated in the same geometry with V_0 varied to reproduce the deuteron binding energy. The obtained value of V_0 was 515.26 MeV. The spectroscopic amplitude for the *s-wave* was $S_s = 0.9706$ and for the *d-wave* $S_d = 0.241$, as proposed by Amar et al. [38], which allowed for the reproduction of the quadrupole moment of the deuteron. As seen in the

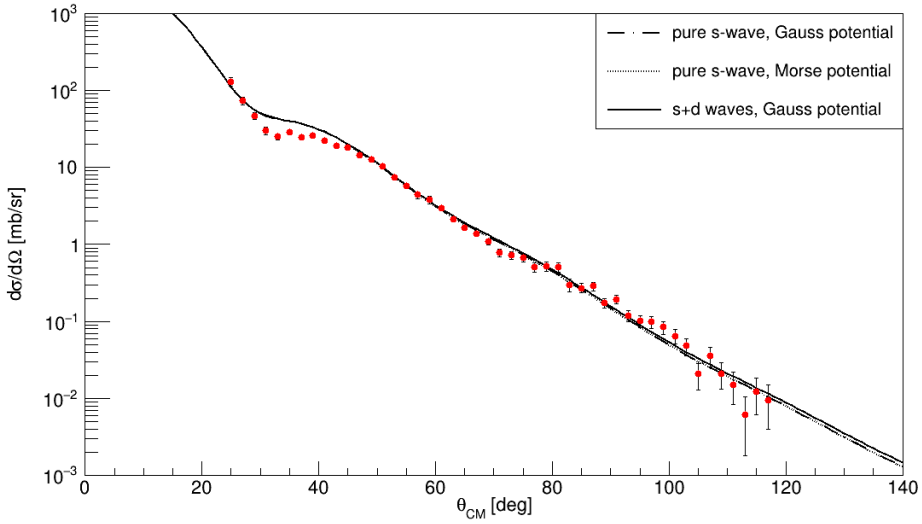

Figure 4.6: Experimental data and OM calculations of differential cross sections for the d+^{6}He elastic scattering. The cross section calculations are based on the optical potential obtained from folding a p+^{6}He potential with the $^2H_{g.s}$ wave function in *s-wave* and *s+d* wave configurations. The p+^{6}He potential was the fitted global OMP of Varner (**fGOP**).

upper panel of Fig. 4.5, the choice of binding potential of ^{2}H influences the *s-wave*

component in the region close to the origin, up to 2.5 fm.

Each of the above deuteron wave functions was folded with the p+^{6}He **fGOP**. The resulting d+^{6}He scattering potentials were used to calculate the elastic scattering differential cross section. As seen in Fig. 4.6, all of the cross sections overlap entirely up to 60° in the CM, with the *s+d* waves representation resulting in a slightly higher cross section for larger CM angles. Nevertheless, the difference is negligible, so the pure *s-wave* representation in the Gauss form of the binding potential will be used for the calculations of the d+^{6}He potential with the potential folding method using the a **fCDCC** p+^{6}He potential. The small difference between the cross sections presented in Figure 4.6 suggests that the effect of the quadrupole deformation of deuteron ground state on the d+^{6}He elastic scattering is very small.

The d+^{6}He scattering potential obtained from folding the **fCDCC** p+^{6}He potential with the pure *s-wave* representation of the $^2H_{g.s.}$ wave function will be referred to as the **"folded p+^{6}He fCDCC"**. The corresponding d+^{6}He potential obtained by folding the **fGOP** will be referred to as the **"folded p+^{6}He fGOP"**. The potentials described in this paragraph, along with the **"fitted d+^{6}He GOP"** were used to calculate the d+^{6}He differential cross section. Both folded potentials

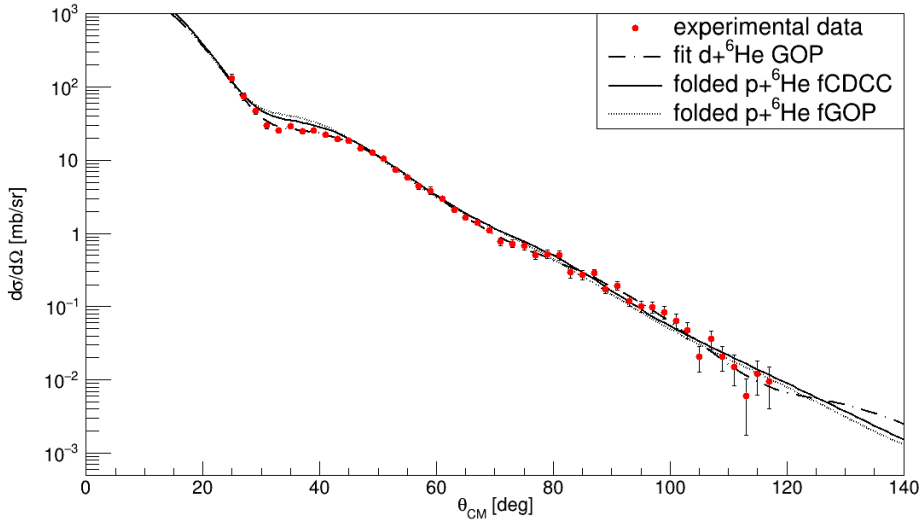

Figure 4.7: Experimental data and OM calculations of differential cross sections for the d+^{6}He elastic scattering. The calculations were performed with the following d+^{6}He OPs: **fitted d+^{6}He GOP**, **folded p+^{6}He fGOP** and **folded p+^{6}He fCDCC**.

result in slightly overestimated cross sections in the angular range from 30° to 40° in the CM, as seen in Fig. 4.7. The otherwise good agreement between cross section calculated from folded OMPs hints at the minor influence of the deuteron continuum states on the resulting cross section.

In the next step, the two d+^{6}He OMPs obtained with the folding method were fitted to the angular distribution of the d+^{6}He elastic scattering. The resulting cross sections were compared with the experimental data and the cross section obtained from the OM calculations with **fitted d+^{6}He GOP**. Differential cross sections for the d+^{6}He scattering obtained from multiparameter fitting of Zhang's global optical potential describe the experimental data to a great extent over the whole CM range. The cross section from **folded p+^{6}He fGOP** follows the experimental data points closer in the region from 100° to 120° in the CM, but at more forward angles, the **folded p+6He fCDCC** and **folded p+6He fGOP** cross sections overlap. A comparison of the obtained χ^2/N values is presented in Table 4.4.

Potential	χ^2/N
GOP Zhang	8.542
fitted d+^{6}He GOP	0.717
folded p+^{6}He fCDCC	3.127
fitted **folded p+^{6}He CDCC**	1.866
folded p+^{6}He fGOP	5.332
fitted **folded p+^{6}He GOP**	3.856

Table 4.4: Comparison of χ^2/N obtained for different OM potentials for the d+^{6}He scattering (see text) and their fits to the experimental data.

The difference between fitted and non-fitted folded potentials is small. Nevertheless, the fitted global potential describes the experimental data better. This seems logical since nine parameters were varied in the case of the global potential, while in the case of the folded potentials only the amplitudes of the real and imaginary parts were varied. At the same time it is worth noting that the folded potentials fit to the p+^{6}He experimental data performed significantly better in describing the d+^{6}He scattering than the global OP of Zhang [4].

4.3 The ^{6}He(d,t)^{5}He single neutron transfer reaction

The angular distribution of the differential cross section for the neutron transfer reaction was analyzed using the DWBA. Defining the scattering wave functions in the entrance and exit channels was necessary to perform the analysis. These functions were generated using the optical potentials corresponding to the elastic scattering in the given channel.

4.3.1 Entrance channel optical potentials

The following d+^{6}He optical potentials obtained in the previous section (see Table 4.4) will be used to describe the entrance channel:

- **fitted d+^{6}He GOP** obtained from fitting the optical potential parametrization of Zhang [4] to the d+^{6}He experimental data,
- **folded p+^{6}He fGOP** obtained from the global proton optical potential by Varner [2] using the folding method, fitted to the p+^{6}He experimental data
- **folded p+^{6}He fCDCC** obtained from the p+^{6}He optical potential (microscopic CDCC calculations performed by Rusek et al. [3]) using the folding method, fitted to the p+^{6}He experimental data

4.3.2 Exit channel optical potentials

Due to the lack of experimental data for the t+^{5}He elastic scattering, two different optical potentials were used to describe this system. The first potential was obtained from the parameterization proposed by Pang et al. [5]. The obtained parameters are presented in Table 4.5 and the potential is plotted in Figure 4.8 as the solid curves.

term	V_0 [MeV]	r_0 [fm]	a_0 [fm]	$W_{0,s}$ [MeV]	$r_{w,s}$ [fm]	$a_{w,s}$ [fm]
volume	109.3	1.743	0.82	6.15	2.11	0.84
surface	-	-	-	11.57	2.11	0.84

Table 4.5: Optical potential parameters for the t+^{5}He elastic scattering at 23 MeV/n using the Pang [5] parametrization.

The second potential for the t+^{5}He scattering was obtained from folding t+^{4}He and n+t scattering potentials with the wave function of the ^{4}He$_{g.s.}$ system. The t+^{4}He potential was obtained from the parameterization proposed by Becchetti and Greenlees [40]:

$$U(r) = V_v(r) + W_v(r) + V_{so}(r) \tag{4.6}$$

where $V_v(r)$ and $W_v(r)$ are volume real and imaginary terms of Woods-Saxon shape. Due to the software limitations regarding the folding of the spin-orbit term, it will not be used in further calculations. The obtained parameters of the t+^{4}He scattering potential are presented in Table 4.6.

term	$V_{0,so}$ [MeV]	$r_{0,so}$ [fm]	$a_{0,so}$ [fm]	W_0 [MeV]	r_w [fm]	a_w [fm]
volume	156.8	1.743	0.82	6.15	2.11	0.84
spin-orbit	2.5	1.2	0.72	-	-	-

Table 4.6: Optical potential parameters for the t+^{4}He elastic scattering at 23 MeV/n using the Becchetti and Greenlees [40] parametrization.

The n+^{3}H scattering potential was calculated using the Varner et al. [2] optical potential parametrization and the parameters are presented in Table 4.7.

term	V_0 [MeV]	r_0 [fm]	a_0 [fm]	$W_{w,s}$ [MeV]	$r_{w,s}$ [fm]	$a_{w,s}$ [fm]
volume	44.38	1.55	0.69	1.645	1.498	0.69
surface	-	-	-	2.596	1.498	0.69

Table 4.7: Optical potential parameters for the n+^{3}H elastic scattering at 23 MeV/u using the Varner et al. [2] parametrization.

For the calculation of the ^{4}He$_{g.s.}$ wave function, the binding potential proposed by Bang and Gignoux [41] was used. The potential consists of a real Woods-

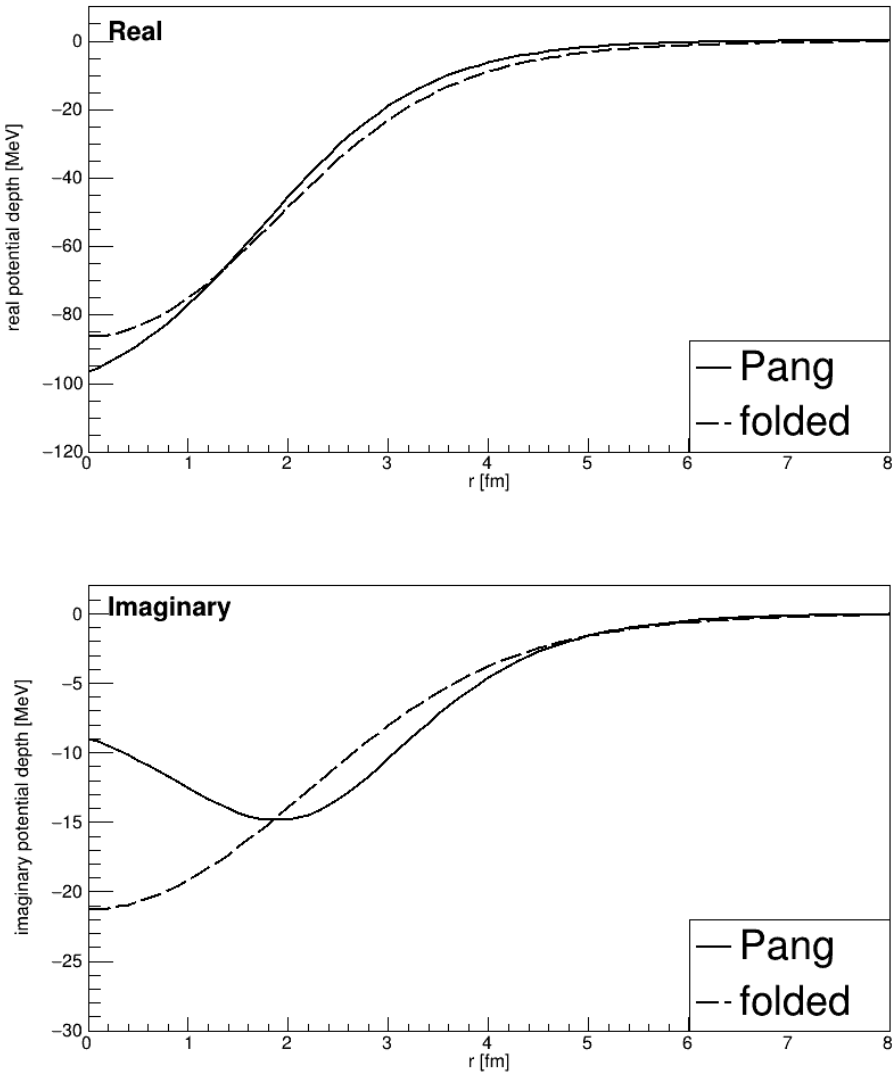

Figure 4.8: Real and imaginary parts of the t+^{5}He OM potentials are presented in the upper and lower panels, respectively. The potentials are the GOP of Pang [4] and the potential obtained through folding t+^{4}He and n+t scattering potentials with the wave function of the $^4\text{He}_{\text{g.s.}}$ system.

Saxon form plus a spin-orbit component of Thomas form

$$V_{4He+n}(r) = \frac{-V_{vol}}{1 + exp[(r - R_{WS})/a_{WS}]} + \frac{\mathbf{l} \cdot \mathbf{s}}{r} \frac{d}{dr} \frac{V_{so}}{1 + exp[(r - R_{so})/a_{so}]} \tag{4.7}$$

with $V_{vol} = 43.0\ MeV$, $R_{WS} = 2.0\ fm$, $a_{WS} = 0.70\ fm$, $V_{so} = 40.0\ MeV$, $R_{WS} = 2.0\ fm$ and $a_{WS} = 0.70\ fm$.

The resulting t+^{5}He OM potential is presented in Figure 4.8 as the dashed curves.

4.3.3 Wave functions of ^{6}He$_{g.s}$=^{5}He$_{g.s}$+n and ^{3}H=^{2}H+n

The neutron binding potential in ^{6}He$_{g.s.}$ was taken from Rusek et. al [7] in the form

$$V(r) = \frac{-V_{WS}}{1 + exp[(r - R_{WS})/a_{WS}]} \tag{4.8}$$

with $R_{WS} = 2.137\ fm$ and $a_{WS} = 0.65\ fm$. The potential depth V_{WS} was adjusted to $V_{WS} = 56.88\ MeV$ in order to reproduce the binding energy of the ^{5}He$_{g.s}$+n system.

The neutron binding potential in ^{3}H was calculated according to a parametriza-

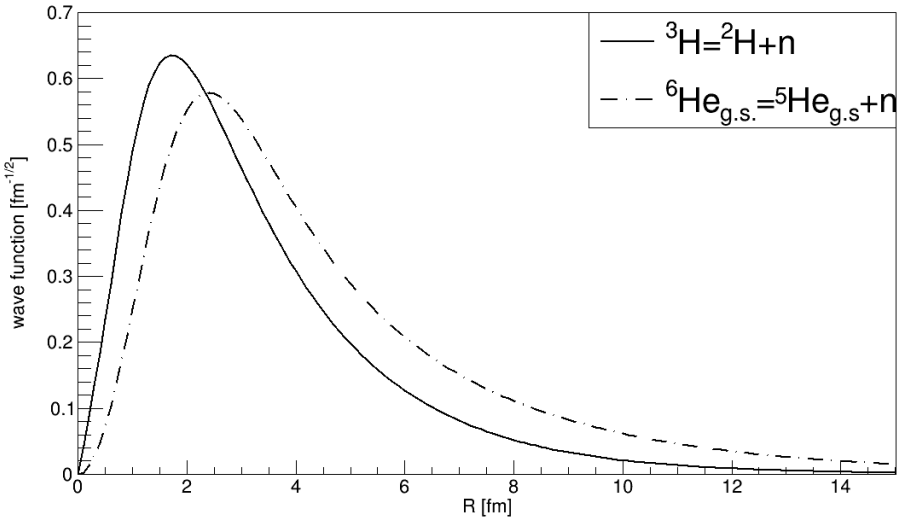

Figure 4.9: Neutron wave functions in ^{6}He$_{g.s.}$=^{5}He$_{g.s}$+n and ^{3}H=^{2}H+n systems calculated with binding potentials taken from Rusek [7] and proposed by Brida [42].

tion proposed by Brida et al. [42] of the form:

$$V_{d+n}(r) = \frac{-V_{WS}}{1 + exp[(r - R_{WS})/a_{WS}]} - V_{gauss} exp[-(r/\rho)^2] \tag{4.9}$$

with $V_{WS} = -172.88\ MeV$, $R_{WS} = 0.56\ fm$, $a_{WS} = 0.69\ fm$, $V_{gauss} = -198.8\ MeV$ and $\rho = 0.64\ fm$. The spectroscopic amplitude of the ^{3}H in the ^{2}H+n configuration was set to S$_{d+n}$=1.14, as proposed by Brida [42].

4.3.4 Transition potential

In each of the DWBA calculations, the transition potential was defined in the prior representation with the full remnant term according to the formula

$$U_{prior}(\mathbf{R}_{Aa}, \mathbf{R}_{Bx}) = V_{Bx}(\mathbf{R}_{Bx}) + U_{Ba}(\mathbf{R}_{Ba}) - U_{Aa}(\mathbf{R}_{Aa}) \tag{4.10}$$

where in our case V_{Bx} is the binding potential of the ^{5}He$_{\text{g.s}}$+n system, U_{Ba} is the scattering potential of d+^{5}He, and U_{Aa} is the scattering potential of d+^{6}He (see Figure 1.3). The transition potential in the post representation is defined by the following formula

$$U_{post}(\mathbf{R}_{Bb}, \mathbf{R}_{ax}) = V_{ax}(\mathbf{R}_{ax}) + U_{Ba}(\mathbf{R}_{Ba}) - U_{Bb}(\mathbf{R}_{Bb}) \tag{4.11}$$

where V_{ax} is the binding potential of the ^{2}H+n system, U_{Ba} is the scattering potential of d+^{5}He, and U_{Bb} is the scattering potential of t+^{5}He (see Figure 1.4). Due to the lack of a scattering potential for d+^{5}He, which is needed to calculate the transition potential with the full remnant term, the d+^{6}He scattering potential was used instead. The importance of the remnant part is visible in Fig. 4.10, where the

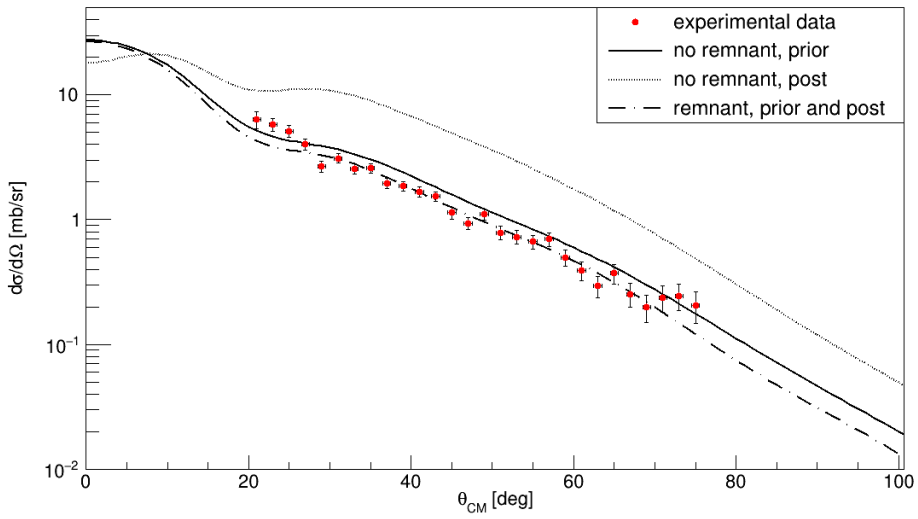

Figure 4.10: A comparison of the DWBA differential cross sections for the ^{6}He(d,t)^{5}He$_{\text{g.s}}$ reaction with and without the remnant term in the prior and post representations. The post and prior cross sections with the remnant term overlap almost completely and are drawn with one line. The same spectroscopic amplitude $S_{^5\text{He+n}}$=1.178 was used for all calculations.

neutron transfer cross section is calculated with identical entrance and exit channel potentials in prior and post representations, with and without the remnant term. For both post and prior calculations, the **fitted d+^{6}He GOP** and the optical potential parametrization by Pang for t+^{5}He were used for the description of the entrance and exit channels accordingly. A dot-dashed line was used to plot both prior and post representations with the full remnant term because the difference between them was practically unnoticeable.

4.3.5 Results of the DWBA calculation

Differential cross sections for the neutron transfer were calculated with the DWBA method according to Equation 1.27 with the entrance potentials defined in the beginning of this section (section 4.2) and the exit potentials defined in subsection 4.3.2.

The spectroscopic amplitude $S_{^{5}\mathrm{He}+\mathrm{n}}$ was adjusted for each d+^{6}He scattering potential in order to minimize χ^2/N.

Initially, the cross sections obtained with the t+^{5}He scattering potential by Pang and different d+^{6}He scattering potentials were used to obtain spectroscopic amplitudes adjusted to fit the experimental data. For the **folded p+^{6}He fCDCC** potential $S_{^{5}\mathrm{He}+\mathrm{n}}$=1.125 was obtained, for the **fitted d+^{6}He GOP** $S_{^{5}\mathrm{He}+\mathrm{n}}$=1.178 and for the **folded p+^{6}He fGOP**, $S_{^{5}\mathrm{He}+\mathrm{n}}$=1.130. The angular distributions have similar shapes, as seen in Fig. 4.11. All three potentials give a good description of the experimental data, with the folded d+^{6}He potentials performing slightly better over the range from 20° to 30° in CM.

Next, the same procedure was repeated for the folded t+^{5}He potential. For the **folded p+^{6}He fCDCC** potential $S_{^{5}\mathrm{He}+\mathrm{n}}$=1.172 was obtained, for the **fitted d+^{6}He GOP** $S_{^{5}\mathrm{He}+\mathrm{n}}$=1.231, and for the **folded p+^{6}He fGOP**, $S_{^{5}\mathrm{He}+\mathrm{n}}$=1.168. The differential cross section for the neutron transfer obtained with the **folded p+^{6}He fGOP** is slightly different from the cross sections obtained using the Zhang parametrization and the **folded p+^{6}He fCDCC** potential, especially around 20° in the CM and above 60° in the CM. Nevertheless, all three entrance channel potentials give angular distributions of similar shapes and satisfactorily describe the data, as

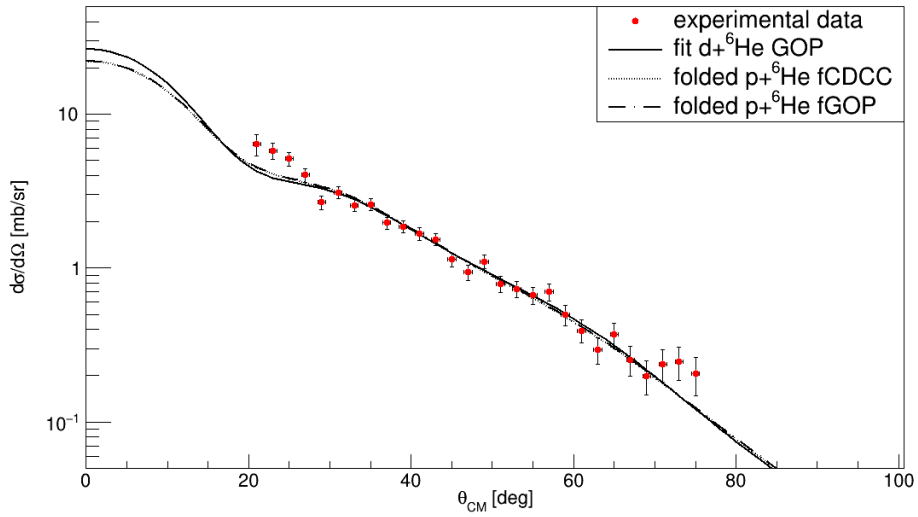

Figure 4.11: Experimental data and DWBA calculations for the ^{6}He(d,t)^{5}He$_{g.s.}$ reaction at 26 MeV/u. The exit channel potential was taken from the Pang et al. [5] optical potential parametrization, while the optical potentials obtained in the previous section were used in the entrance channel.

seen in Fig. 4.12.

The spectroscopic amplitude for the ^{6}He$_{g.s.}$=^{5}He$_{g.s}$+n configuration was averaged over the entrance and exit channel potentials defined at the beginning of this section and amounts to S$_a$=1.167 $^{+0.148}_{-0.140}$, with the error coming from the systematic experimental error (14.1%), the statistical error of the experimental data (18.1%) and the systematic error associated with the entrance, exit and core-core interaction potentials $\binom{+5.5\%}{-5.9\%}$. After taking into account the uncertainty, the obtained value agrees with the theoretical one from shell model calculations [43, 44] for the ^{5}He$_{g.s.}$,

Entrance potential	Exit potential	S$_{5He+n}$	χ^2/N
fitted d+^{6}He GOP	Pang [5]	1.178	1.642
folded p+^{6}He fGOP	Pang [5]	1.130	1.822
folded p+^{6}He fCDCC	Pang [5]	1.125	1.541
fitted d+^{6}He GOP	folded	1.231	1.675
folded p+^{6}He fGOP	folded	1.168	1.856
folded p+^{6}He fCDCC	folded	1.172	1.538

Table 4.8: Spectroscopic amplitudes for the ^{6}He$_{g.s.}$=^{5}He$_{g.s}$+n configuration for different entrance and exit potentials (details in text). The amplitudes were obtained by fitting the cross sections calculated with the DWBA method to the experimental data.

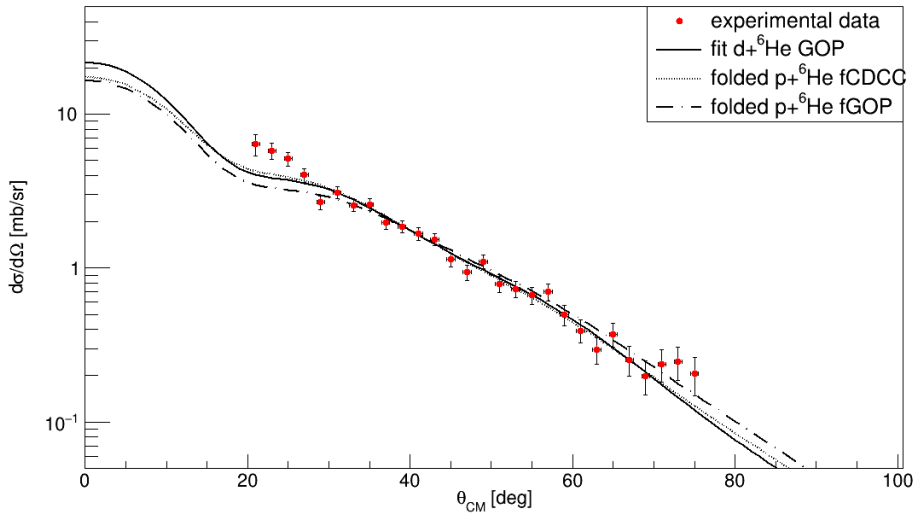

Figure 4.12: Experimental data and DWBA calculations for the ^{6}He(d,t)^{5}He$_{\text{g.s.}}$ reaction at 26 MeV/n. The exit channel potential was calculated using the double-folding method, while thr optical potentials obtained in the previous section were used in the entrance channel.

where S_{5He+n}=1.265.

The spectroscopic factor calculated based on the spectroscopic amplitude obtained from the experimental data is $SF_{exp}=1.36\ ^{+0.35}_{-0.33}$, and the SF obtained from shell model calculations [44] is $SF_{theo}=1.6$. The SF values agree after taking into account the uncertainty.

In general, the spectroscopic factors obtained experimentally from transfer reactions do not agree with the theoretical predictions, and their values amount to $\sim 0.55^{+0.10}_{-0.10}$ of the theoretical value [47, 48]. This so-called quenching of the spectroscopic factors is a known phenomenon observed also in proton knockout by electrons and proton and neutron removal reactions. While in one nucleon removal reactions a quenching factor dependence on the proton/neutron binding energy asymmetry [49, 6] is found, such a relation is not observed in one nucleon transfer reactions [48]. The quenching factor of the theoretical and experimental SFs is defined as $R_{SF}=SF_{exp}/SF_{theo}$, and in our case, it equals $R_{SF}=0.85\ ^{+0.22}_{-0.20}$. After considering the uncertainties, the obtained value aligns with widely reported results for single-nucleon transfer reactions [47, 48]. This result is presented in Figure 4.13 alongside values for oxygen obtained by Flavigny et al. [46], and for argon obtained by Heb-

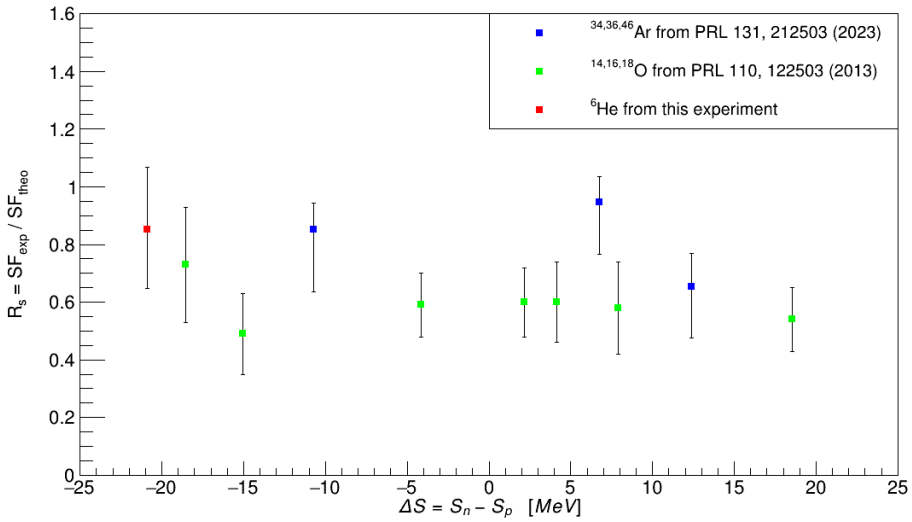

Figure 4.13: Quenching factors $R_s = SF_{exp}/SF_{theo}$ as a function of the difference between the neutron and proton separation energies ΔS. The data points for the ^{34,36,46}Ar were taken from Table III. of Hebborn et al. [45] and the data points for ^{14,16,18}O were taken from Table I of Flavigny et al. [46].

born et al. [45].

One should remember, however, that the calculations were performed for $^{6}He_{g.s.}=^{5}He_{g.s}+n$ only, whereas in the experimental data there is a mixture of ground and excited states of ^{5}He that could not be resolved. Consequently, the experimental differential cross sections for the transfer to the ground state of ^{5}He are overestimated, meaning that the disagreement between the theoretical and experimental spectroscopic amplitudes and spectroscopic factors might be more significant. At the same time, the quenching factor R_{SF} would be lower and, therefore, closer to the generally reported value [47, 48].

Conclusions

This work concerns on experimental study of the reactions of ^{6}He with protons and deuterons in inverse kinematics at 26 MeV/u. The experiment was performed at the ACCULINNA-2 fragment separator of the Flerov Laboratory of Nuclear Reactions at the Joint Institute for Nuclear Research in Dubna, Russia, in 2018. A ^{15}N beam was accelerated to an energy of 49.7 MeV/u by the U400M cyclotron and impinged on a primary beryllium target. The secondary beam was cleaned by the ACCULINNA-2 fragment separator, and the ^{6}He secondary beam was delivered to the reaction chamber where it struck a CD_2 polyethylene target. Angular distributions of p+^{6}He and d+^{6}He elastic scattering, as well as the ^{6}He(d,t)^{5}He transfer reaction were measured. It is worth noting that the differential cross sections for the elastic scattering of ^{6}He from deuterons and the (d,t) transfer reaction were measured for the first time.

The beam energy was determined with a time-of-flight detector consisting of two subdetectors placed in focal planes F3 and F5, 12.35 m apart, while the beam tracking on target was performed with two multi-wire proportional chambers. The total beam flux was estimated based on the count rate of the ToF subdetector located at the focal plane F5, just before the reaction target. Thanks to the beam tracking, scattering angles were calculated, considering the observed beam vector.

Elastic scattering measurements were made in three different geometries, allowing for particle registration over the wide angular range from 35° to 80° in the laboratory system of coordinates. The target thickness calculation was performed with the use of the experimental data obtained in an additional experiment performed with a ^{6}He beam and a ^{1,2}H gas-filled target.

Regarding the transfer reaction, the ^{3}H ions were registered with the left telescope positioned at a distance of 25.0 cm from the target at an angle of 15° to the beam axis and the ^{4}He ions formed as a result of the decay of ^{5}He into an alpha particle and a neutron were registered using the right telescope positioned at a distance of 25.0 cm from the target and set at an angle of 15° to the beam axis.

The first step in the data analysis process was to identify the correct positions of the MWPC detectors which slightly deviated from their nominal values. Subsequently, time calibration of the ToF detector and energy calibration of the silicon and scintillation detectors were performed. Minor corrections to the positions of the left and right telescopes and the target were introduced during the detector calibration process.

After the detectors were calibrated, the collected data were cleaned, and the elastic scattering was identified based on the registration of ^{1,2}H and ^{6}He in coincidence. Protons and deuterons were identified using the ^{6}He-^{1,2}H scattering angle dependence, while ^{6}He was identified based on the $\Delta E - E$ spectra in the right telescope. The angular distributions of the scattered protons and deuterons obtained in the laboratory system of coordinates were transformed to the center-of-mass system. The differential cross section for the p+^{6}He elastic scattering is in good agreement with existing experimental data [1] obtained at a similar energy.

The transfer reaction was identified by registering tritons in the left telescope and ^{4}He in the right telescope, which was confirmed using the $\Delta E - E$ spectrum. However, the process proved problematic for low-energy tritons, for which the $\Delta E - E$ spectrum could not be plotted because they were stopped in the silicon detector. Instead, the missing mass spectrum of ^{4}He and the particle registered in the left telescope was used, allowing for convenient identification of the transfer reaction.

In order to assess the detection efficiency of the experimental setup, a standalone Monte Carlo simulation was written for both elastic scattering and transfer reactions. The experiment was recreated using the beam data collected during the experiment, which enabled error estimation.

Once the data analysis was concluded, the obtained angular distribution for

the p+^{6}He elastic scattering differential cross section was analyzed within the optical model. Initially, the experimental cross section was compared with the cross sections calculated based on a set of optical potentials. The first potential was the global optical potential of Varner [2], the second was the optical potential obtained by Wolski [1] based on experimental data, and the third was an optical potential obtained by Rusek [3] from microscopic CDCC calculations based on Wolski's experimental data. Among the compared angular distributions, that obtained with Varner's global optical potential best describes the current data. Wolski's and Rusek's potentials also describe the data reasonably well, but Wolski's potential overestimates the measured cross section in the range above 110 degrees in the CM, while Rusek's potential underestimates the experimental data in the range between 60° and 80° in the CM. In the next step, the optical potential parameters were adjusted to fit the experimental data.

Subsequently, the measured angular distribution for the d+^{6}He elastic scattering differential cross section was compared with the angular distribution of the d+^{6}Li elastic scattering at a similar energy. The significant difference between these distributions shows the strong dependence on the structure of the target nucleus. Collected data for the d+^{6}He scattering were compared with differential cross sections calculated using global optical potentials by Daehnick [31], An [33] and Zhang [4] from which Zhang's fit the experimental data best.

Additionally, d+^{6}He optical potentials were calculated with the single-folding method by folding the obtained p+^{6}He potentials with the deuteron wave function. For this purpose, the $^{2}H_{g.s}$ wave function was calculated in an *s-wave* configuration with binding potentials of Gaussian [36] and Morse [37] forms, as well as in an *s+d-wave* configuration with a binding potential of Gaussiab form [36]. It was observed that resulting wave function of the $^{2}H_{g.s}$ and the quadrupole deformation of the deuteron ground state have little influence on the d+^{6}He elastic scattering.

Differential cross sections calculated from the OMP obtained with the folding method from p+^{6}He potentials fitted to the experimental data describe the d+^{6}He scattering well, which hints at a small influence of the deuteron continuum states on the resulting cross section. The parameters of Zhang's global potential and the

folded potential were adjusted in order to fit the experimental data.

The transfer reaction cross section was analyzed using the DWBA method. In the entrance channel, several d+^{6}He potentials obtained through fitting the experimental data were used. In the exit channel, two different potentials were tried: a global optical potential by Pang [5] and an optical potential obtained from folding the ^{4}He+t global optical potential of Becchetti and Greenlees [40] and the n+t global optical potential of Varner et al. [2] with the ^{5}He$_{g.s}$ wave function. The transition potential was considered in both post and prior representations, with and without the remnant term. It was found that the remnant term significantly influences the resulting cross section. In the calculations the d+^{6}He potential from the entrance channel was used as the core-core interaction potential.

The spectroscopic amplitudes of the ^{6}He$_{g.s.}$=^{5}He$_{g.s.}$+n configuration were obtained with the SA for the ^{3}H=^{2}H+n configuration of tritium set to S_{2H+n}=1.14, as proposed by Brida [42]. The SA averaged over the results of the DWBA calculations performed with various OMPs in the entrance and exit channels is $S_{5He+n} = 1.167\ ^{+0.148}_{-0.140}$ with the uncertainties being associated with the experimental systematic and statistical errors and the analysis error corresponding to the choice of the OM potentials. After considering the uncertainties, the obtained spectroscopic amplitude agrees with the theoretical value [44].

The spectroscopic factor of the ^{6}He$_{g.s.}$=^{5}He$_{g.s}$+n configuration obtained from the experimental data (SF_{exp}=1.36 $^{+0.35}_{-0.33}$) agrees with the factor obtained from theoretical predictions (SF_{theo}=1.6) after taking into account the uncertainties. It is worth noting that in this work the experimental cross section for the transfer reaction is a mixture of both the ground and excited states of ^{5}He. Therefore, the obtained SF can be considered as an upper limit of the ^{6}He$_{g.s.}$=^{5}He$_{g.s}$+n configuration. This also means that the resulting quenching factor of the experimental SF is lower and thus closer to the generally reported value.

List of abbreviations

2D two dimensional

ADC analog-to-digital converter

CDCC continuum-discretized coupled channels

CFD constant fraction discriminator

CM center-of-mass system

DAQ data acquisition system

DSSD double sided silicon detector

DWBA distorted-wave Born approximation

ECR electron cyclotron resonance

fCDCC fit continuum-discretized coupled channels

fGOP fit global optical potential

FWHM full width at half maximum

GOM global optical model

GOP global optical potential

MBS multi branch system

MC Monte Carlo

MWPC multi-wire proportional chamber

OM optical model

OMP optical model potential

OP optical potential

PCB printed circuit board

PID particle identification

PMT photomultiplier

QDC charge integrating analog-to-digital converter

SF spectroscopic factor

TDC time-to-digital converter

ToF time-of-flight

References

[1] R. Wolski et al. "Cluster structure of 6He studied by means of 6He + p reaction at 25 MeV/n energy". en. In: *Physics Letters B* 467.1 (Nov. 1999), pp. 8–14.

[2] R.L. Varner et al. "A global nucleon optical model potential". en. In: *Physics Reports* 201.2 (1991), pp. 57–119.

[3] K. Rusek, K. W. Kemper, and R. Wolski. "6 He interaction with protons". en. In: *Physical Review C* 64.4 (Sept. 2001), p. 044602.

[4] Y. Zhang, D. Y. Pang, and J. L. Lou. "Optical model potential for deuteron elastic scattering with 1p-shell nuclei". In: *Physical Review C* 94.1 (July 2016). Publisher: American Physical Society, p. 014619.

[5] D. Y. Pang et al. "Global optical model potential for $A = 3$ projectiles". In: *Phys. Rev. C* 79 (2 Feb. 2009), p. 024615.

[6] T. Aumann et al. "Quenching of single-particle strength from direct reactions with stable and rare-isotope beams". en. In: *Progress in Particle and Nuclear Physics* 118 (2021), p. 103847.

[7] K. Rusek, L. Giot, and P. Roussel-Chomaz. "Influence of the transfer reactions on p + 6He elastic scattering". en. In: *The European Physical Journal A* 32.2 (May 2007), pp. 159–163.

[8] R. S. Mackintosh and K. Rusek. "Dynamic polarization potential for 6 He + p due to breakup". en. In: *Physical Review C* 67.3 (Mar. 2003), p. 034607.

[9] P. Descouvemont. "Four-body extension of the continuum-discretized coupled-channels method". en. In: *Physical Review C* 97.6 (June 2018), p. 064607.

[10] P. Descouvemont. "Low-energy Li 11 + p and Li 11 + d scattering in a multicluster model". en. In: *Physical Review C* 101.6 (June 2020), p. 064611.

[11] S. Fernbach, R. Serber, and T. B. Taylor. "The Scattering of High Energy Neutrons by Nuclei". In: *Phys. Rev.* 75 (9 May 1949), pp. 1352–1355.

[12] G. R. Satchler. *Introduction to Nuclear Reactions*. en. London: Palgrave Macmillan UK, 1990. ISBN: 9781349205318.

[13] *The Euroschool on Exotic Beams, Vol. IV*. en. Vol. 879. Lecture Notes in Physics. Berlin, Heidelberg: Springer Berlin Heidelberg, 2014. ISBN: 9783642451409.

[14] G. Kaminski et al. "Status of the new fragment separator ACCULINNA-2 and first experiments". In: *Nuclear Instruments and Methods in Physics Research, Section B: Beam Interactions with Materials and Atoms* 463 (2020), pp. 504–507.

[15] A.A. Bezbakh et al. "First radioactive beams at ACCULINNA-2 facility and first proposed experiment". In: vol. 177. 2018.

[16] G. F. Knoll. *Radiation Detection and Measurement*. John Wiley and Sons, Inc., 2010.

[17] Nikolaus Kurz and Jörn Adamczewski-Musch. *Multi Branch System*. URL: https://www.gsi.de/en/work/research/experiment_electronics/data_processing/data_acquisition/mbs (visited on 04/23/2023).

[18] Wikipedia. *VMEbus*. URL: https://en.wikipedia.org/wiki/VMEbus (visited on 11/29/2023).

[19] Wikipedia. *Computer Automated Measurement and Control*. URL: https://en.wikipedia.org/wiki/Computer_Automated_Measurement_and_Control (visited on 11/29/2023).

[20] MultiMedia LLC. *MS Windows NT Kernel Description*. URL: https://www.gsi.de/en/work/research/experiment_electronics/data_processing/data_analysis/the_go4_home_page (visited on 04/17/2023).

[21] Rene Brun and Fons Rademakers. *ROOT - An Object Oriented Data Analysis Framework*. URL: https://root.cern/ (visited on 04/17/2023).

[22] IAEA. *Live Chart of Nuclides*. URL: https://nds.iaea.org/relnsd/vcharthtml/VChartHTML.html (visited on 04/18/2023).

[23] M. Pârlog et al. "Response of CsI(Tl) scintillators over a large range in energy and atomic number of ions. Part I: recombination and δ-electrons". In: *Nuclear Instruments and Methods in Physics Research Section A: Accelerators, Spectrometers, Detectors and Associated Equipment* 482.3 (2002), pp. 674–692. ISSN: 0168-9002.

[24] S. Agostinelli et al. "Geant4—a simulation toolkit". en. In: *Nuclear Instruments and Methods in Physics Research Section A: Accelerators, Spectrometers, Detectors and Associated Equipment* 506.3 (2003), pp. 250–303.

[25] J. Allison et al. "Geant4 developments and applications". In: *IEEE Transactions on Nuclear Science* 53.1 (2006), pp. 270–278.

[26] J. Allison et al. "Recent developments in Geant4". en. In: *Nuclear Instruments and Methods in Physics Research Section A: Accelerators, Spectrometers, Detectors and Associated Equipment* 835 (2016), pp. 186–225.

[27] Patrick Reichart. *Relativistic Kinematics - formula collection*. URL: https://people.nscl.msu.edu/~zegers/ebss2017/RelKin-english.pdf (visited on 01/08/2024).

[28] A.T. Rudchik et al. "One- and two-step processes in the 6Li(d,6Li), (d,7Li) and (d,7Be) reactions at Ed = 50 MeV". In: *Nuclear Physics A* 602.2 (1996), pp. 211–224. ISSN: 0375-9474.

[29] Thompson Ian. *FRESCO, Coupled Reaction Channels Calculations @ONLINE*. URL: https://www.fresco.org.uk/.

[30] C. M. Perey and F. G. Perey. "Deuteron Optical-Model Analysis in the Range of 11 to 27 MeV". en. In: *Physical Review* 132.2 (Oct. 1963), pp. 755–773.

[31] W. W. Daehnick, J. D. Childs, and Z. Vrcelj. "Global optical model potential for elastic deuteron scattering from 12 to 90 MeV". In: *Physical Review C* 21.6 (June 1980), p. 2253.

[32] J. Bojowald et al. "Elastic deuteron scattering and optical model parameters at energies up to 100 MeV". In: *Phys. Rev. C* 38 (3 Sept. 1988), pp. 1153–1163.

[33] Haixia An and Chonghai Cai. “Global deuteron optical model potential for the energy range up to 183 MeV”. en. In: *Physical Review C* 73.5 (May 2006), p. 054605.

[34] P. W. Keaton and D. D. Armstrong. “Deuteron Optical Potential with a Tensor Term and Breakup”. en. In: *Physical Review C* 8.5 (Nov. 1973), pp. 1692–1701.

[35] J. M. B. Kellogg et al. “An Electrical Quadrupole Moment of the Deuteron The Radiofrequency Spectra of HD and D_2 Molecules in a Magnetic Field”. In: *Phys. Rev.* 57 (8 Apr. 1940), pp. 677–695.

[36] N. Austern et al. “Continuum-discretized coupled-channels calculations for three-body models of deuteron-nucleus reactions”. en. In: *Physics Reports* 154.3 (1987), pp. 125–204.

[37] Anil Khachi et al. “Deuteron structure and form factors: Using an inverse potential approach”. In: *Phys. Rev. C* 107 (6 June 2023), p. 064002.

[38] A. Amar, K. Rusek, and Sh. Hamada. “Effects of deuteron breakup and nucleon-transfer reactions on d+11B elastic scattering”. en. In: *The European Physical Journal A* 59.8 (Aug. 2023), p. 182.

[39] Philip M. Morse. “Diatomic Molecules According to the Wave Mechanics. II. Vibrational Levels”. In: *Phys. Rev.* 34 (1 July 1929), pp. 57–64.

[40] F D Becchetti Jr and G W Greenlees. “GENERAL SET OF *sup*3He AND TRITON OPTICAL-MODEL POTENTIALS FOR A $>$ 40, E $<$ 40 MeV.” In: *pp 682-3 of Polarization Phenomena in Nuclear Reactions. / Barschall, H. H. (ed.). Madison, Wis. Univ. of Wisconsin Press (1971).* (Jan. 1971).

[41] J. Bang and C. Gignoux. “A realistic three-body model of 6Li with local interactions”. en. In: *Nuclear Physics A* 313.1–2 (1979), pp. 119–140.

[42] I. Brida, Steven C. Pieper, and R. B. Wiringa. “Quantum Monte Carlo calculations of spectroscopic overlaps in A *qe*7 nuclei”. en. In: *Physical Review C* 84.2 (Aug. 2011), p. 024319.

[43] Yu. F. Smirnov and Yu. M. Tchuvil’sky. “Cluster spectroscopic factors for the p -shell nuclei”. en. In: *Physical Review C* 15.1 (Jan. 1977), pp. 84–93.

[44] Nemets O.F. et al. *Nucleon associations in atomic nuclei and many nucleon transfer reactions*. Kiev: Naukova Dumka, 1988.

[45] C. Hebborn, F. M. Nunes, and A.E. Lovell. "New Perspectives on Spectroscopic Factor Quenching from Reactions". en. In: *Physical Review Letters* 131.21 (Nov. 2023), p. 212503.

[46] F. Flavigny et al. "Limited Asymmetry Dependence of Correlations from Single Nucleon Transfer". en. In: *Physical Review Letters* 110.12 (Mar. 2013), p. 122503.

[47] N. K. Timofeyuk. "Spectroscopic factors and asymptotic normalization coefficients for 0 p -shell nuclei: Recent updates". en. In: *Physical Review C* 88.4 (Oct. 2013), p. 044315.

[48] B. P. Kay, J. P. Schiffer, and S. J. Freeman. "Quenching of Cross Sections in Nucleon Transfer Reactions". en. In: *Physical Review Letters* 111.4 (July 2013), p. 042502.

[49] A. Gade et al. "Reduction of spectroscopic strength: Weakly-bound and strongly-bound single-particle states studied using one-nucleon knockout reactions". en. In: *Physical Review C* 77.4 (Apr. 2008), p. 044306.

Appendix A

Target thickness calculation

Appendix B

Tabulated experimental cross sections

θ_{CM} $[deg]$	$d\sigma/d\Omega$ $[\frac{mb}{sr}]$	error $[\frac{mb}{sr}]$	$\theta_{CM}[deg]$	$d\sigma/d\Omega$ $[\frac{mb}{sr}]$	error $[\frac{mb}{sr}]$
31	137.8	41.6	77	2.827	0.324
33	149.0	32.5	79	2.032	0.269
35	102.7	22.4	81	1.618	0.239
37	100.1	18.3	83	2.011	0.184
39	74.52	13.17	85	1.751	0.152
41	77.19	11.91	87	1.728	0.146
43	53.13	8.62	89	1.653	0.142
45	46.27	7.14	91	1.852	0.150
47	50.70	2.99	93	1.632	0.139
49	38.50	2.25	95	1.709	0.140
51	29.27	1.82	97	1.547	0.129
53	22.97	1.52	99	1.270	0.116
55	16.92	1.22	101	1.169	0.112
57	12.72	1.02	103	1.103	0.109
59	9.162	0.807	105	1.089	0.109
61	8.022	0.720	107	1.145	0.113
63	6.674	0.628	109	0.748	0.091
65	5.270	0.535	111	0.887	0.100
67	4.467	0.476	113	0.740	0.095
69	3.521	0.407	115	0.665	0.093
71	3.651	0.403	117	0.556	0.090
73	2.299	0.310	119	0.726	0.109
75	2.374	0.307	121	0.475	0.093

Table B.1: Differential cross-sections of the ^{6}He(p,p)^{6}He scattering along with the statistical error obtained in this experiment.

θ_{CM} $[deg]$	$d\sigma/d\Omega$ $[\frac{mb}{sr}]$	error $[\frac{mb}{sr}]$	$\theta_{CM}[deg]$	$d\sigma/d\Omega$ $[\frac{mb}{sr}]$	error $[\frac{mb}{sr}]$
25	131.0	18.5	73	0.787	0.093
27	74.17	9.15	75	0.732	0.089
29	46.99	5.65	77	0.551	0.077
31	30.18	3.63	79	0.564	0.078
33	25.61	2.73	81	0.550	0.077
35	28.72	2.49	83	0.324	0.059
37	24.89	2.01	85	0.314	0.059
39	25.69	1.81	87	0.365	0.065
41	22.08	1.52	89	0.256	0.056
43	19.27	1.31	91	0.186	0.024
45	18.31	1.19	93	0.114	0.019
47	14.43	1.00	95	0.096	0.017
49	12.77	0.90	97	0.094	0.017
51	10.46	0.80	99	0.081	0.015
53	7.337	0.658	101	0.062	0.013
55	5.821	0.584	103	0.046	0.011
57	4.443	0.513	105	0.020	0.007
59	3.826	0.485	107	0.034	0.010
61	2.956	0.201	109	0.020	0.008
63	2.116	0.166	111	0.014	0.006
65	1.629	0.144	113	0.006	0.004
67	1.394	0.131	115	0.012	0.006
69	1.091	0.115	117	0.009	0.005
71	0.776	0.096			

Table B.2: Differential cross-sections of the ^{6}He(d,d)^{6}He scattering along with the statistical error obtained in this experiment.

θ_{CM} $[deg]$	$d\sigma/d\Omega$ $[\frac{mb}{sr}]$	error $[\frac{mb}{sr}]$
21	6.365	0.994
23	5.776	0.706
25	5.133	0.529
27	4.021	0.400
29	2.673	0.283
31	3.106	0.279
33	2.561	0.235
35	2.595	0.220
37	1.965	0.182
39	1.858	0.168
41	1.674	0.153
43	1.538	0.143
45	1.135	0.120
47	0.9373	0.1061
49	1.102	0.114
51	0.7871	0.0948
53	0.7292	0.0904
55	0.6655	0.0859
57	0.6984	0.0880
59	0.4979	0.0742
61	0.3923	0.0663
63	0.2934	0.0575
65	0.3723	0.0658
67	0.2536	0.0553
69	0.1988	0.0497
71	0.2380	0.0561
73	0.2456	0.0596
75	0.2053	0.0569

Table B.3: Differential cross-sections of the ^{6}He(d,t)^{5}He neutron transfer reaction along with the statistical error obtained in this experiment.